OIST OKINAWA INSTITUTE OF SCIENCE AND TECHNOLOGY

Soap Film Mediated 3D Self-Assembly: Suspended and Displacement Driven Geometries Using Centimeter-Scale Tiles

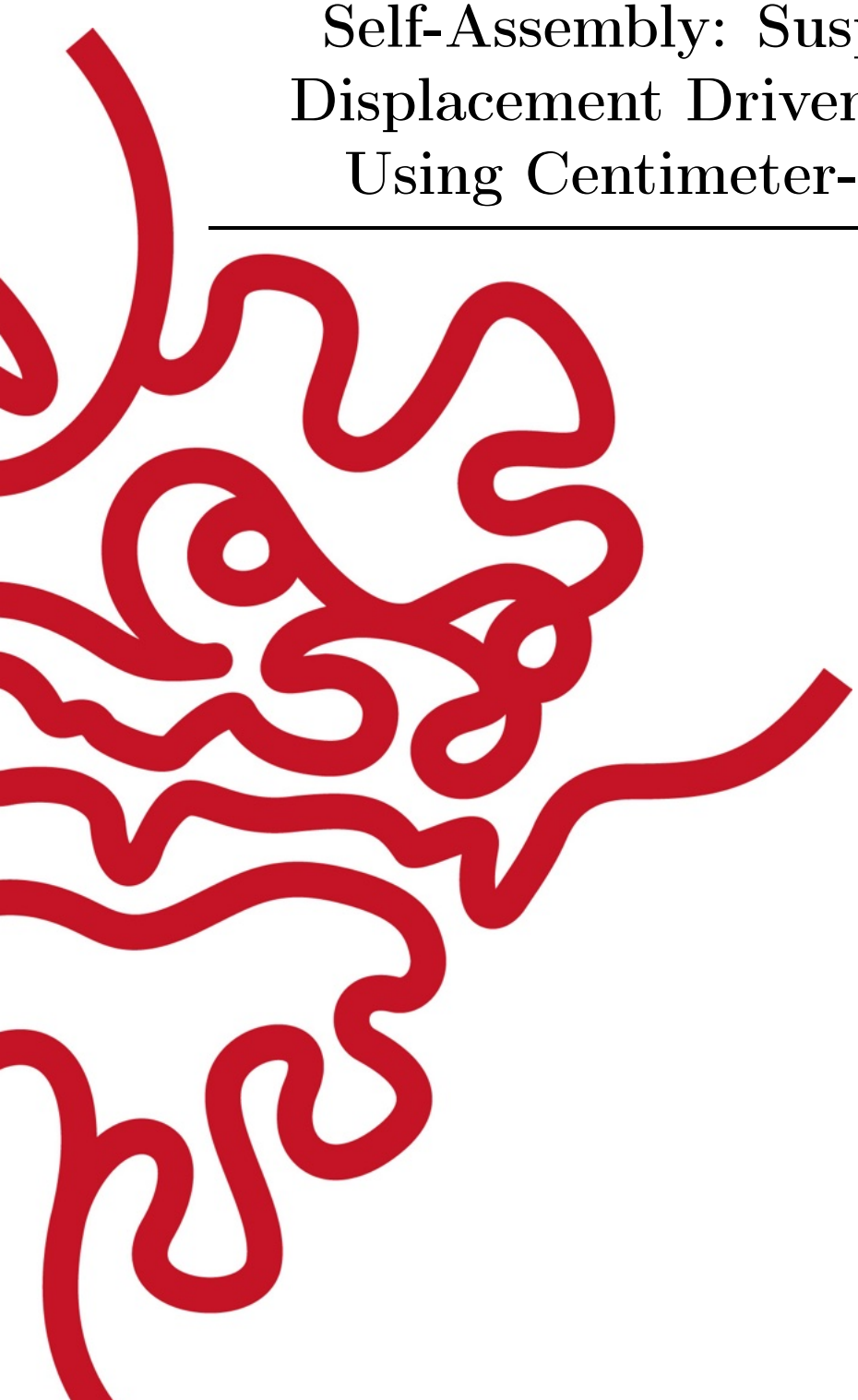
Metadata	Language: English Publisher: Date of Publication: 2022-09-16 Keywords (Ja): Keywords (En): Author: Mihai, Alexandru E-mail: Affiliation:
URL	https://doi.org/10.15102/1394.00002518

Okinawa Institute of Science and Technology
Graduate University

Thesis submitted for the degree

Doctor of Philosophy

Soap Film Mediated 3D Self-Assembly: Suspended and Displacement Driven Geometries Using Centimeter-Scale Tiles



by

Alexandru Mihai

Supervisor: **Eliot Fried**

August, 2022

Declaration of Original and Sole Authorship

I, Alexandru Mihai, declare that this thesis entitled *Soap Film Mediated 3D Self-Assembly: Suspended and Displacement Driven Geometries Using Centimeter-Scale Tiles* and the data presented in it are original and my own work.

I confirm that:

- This work was done solely while a candidate for the research degree at the Okinawa Institute of Science and Technology Graduate University, Japan.
- No part of this work has previously been submitted for a degree at this or any other university.
- References to the work of others have been clearly attributed. Quotations from the work of others have been clearly indicated, and attributed to them.
- In cases where others have contributed to part of this work, such contribution has been clearly acknowledged and distinguished from my own work.

Date: August, 2022
Signature:



Abstract

Soap Film Mediated 3D Self-Assembly: Suspended and Displacement Driven Geometries Using Centimeter-Scale Tiles

The shapes of soap films and their properties have been studied for centuries, and scientific literature mentioning the self-assembly of structures across length scales is becoming increasingly prevalent. While research regarding self-assembly is often focused on the nanoscopic regime, multiple recent reviews aptly state that self-assembly is not limited to molecules. To better understand self-assembly systems in generality, pushing the boundaries of scale and methodology is paramount. This thesis demonstrates the self-assembly of multiple geometries on centimeter length scales by use of a novel medium, namely soap films. Gravity-mediated and displacement-driven assemblies demonstrate platonic solid geometries as well as prismatic and pyramidal structures of varying heights within a catenoid-like soap film membrane. The edge-to-edge alignment of any two tiles is similar to the self-assembly processes described in research regarding the rotation of microstructures. An axes-symmetric model of soap film deflection within the context of gravity-mediated structures is derived and compared to experiments with excellent accordance found. The model is derived by energy methods, using a calculus of variations approach. For the structures constructed using the displacement-driven method, two effective radii predicting the pinch-off of the soap film were discovered and used to compare experimental results to the predictions. Self-folding within the context of displacement-driven assemblies is also presented to reiterate the versatility and robustness of the assembly method. Numerical simulations using Surface Evolver are presented throughout to provide an additional method of analysis of the equilibrium states of the assemblies. The characterization of fundamental geometries assembled by the methods presented in this thesis enables future research and applications in packaging, robotics, and three-dimensional electronics.

Acknowledgments

I would first like to thank my supervisor Professor Eliot Fried for his continued support, encouragement, and interest in the research conducted throughout my doctoral studies. The opportunity to explore varied and fascinating problems is invaluable; it was a privilege to be a part of the Mechanics and Materials Unit at OIST.

Discussions with Dr. Stoffel Janssens, Dr. Johannes Schönke, and Dr. Vikash Chaurasia helped me to discover and clarify questions that may not yet have answers as well as how to approach such questions from experimental, theoretical, and numerical perspectives. I would also like to thank Dr. David Vazquez Cortes and Mr. Michael Grunwald for always answering my repeated questions regarding lab work, 3D printing, and imaging techniques.

I would like to thank my thesis committee, Professor Gustavo Gioia and Professor Simone Pigolotti, for their questions, suggestions and keeping me on track throughout my time at OIST. The help of the Graduate school staff throughout my studies and research also has to be noted, in no particular order: Kozue Higashionna-san, Midori Morinaga-san, Chiaki Chibana-san, Harry Wilson, and Jeremie Gillet.

I would also like to thank some of the friends I have made here in Okinawa: Agneesh, Ainash, Barney, Chris, Nadine, Tadashi, and Chris. Special thanks are necessary for Izabela, for her support, compassion, understanding, friendship, and for always listening. Lastly, I would like to thank my family for their support and encouragement, even after I had moved to what seemed to be a dot in the ocean.

Contents

Declaration of Original and Sole Authorship iii

Abstract v

Acknowledgments vii

Contents ix

List of Figures xi

Introduction 1
- 0.1 Preface . . . 1
- 0.2 Motivation and Discovery . . . 2
- 0.3 Organization of the Thesis . . . 3

1 Background 5
- 1.1 Self-assembly . . . 5
  - 1.1.1 Sub-millimetric scale assemblies . . . 5
  - 1.1.2 Capillary self-assembly . . . 6
- 1.2 Self-Folding . . . 8
  - 1.2.1 Small scale folding . . . 8
  - 1.2.2 Mesoscale and large scale self-folding . . . 10
- 1.3 Soap Films . . . 11
  - 1.3.1 Film thickness and longevity . . . 11
  - 1.3.2 Topological transitions . . . 14

2 Gravity-mediated self-assembly 17
- 2.1 Classical catenoid solution . . . 18
  - 2.1.1 Exsistence criterion of catenoidal solutions . . . 20
  - 2.1.2 Surface Evolver simulations . . . 22
- 2.2 Variational formulation of a suspended ring . . . 24
  - 2.2.1 Boundary value problem . . . 27
  - 2.2.2 Closed form solution . . . 28
- 2.3 Soap film experiments . . . 31
  - 2.3.1 Experimental setup and procedure . . . 31

2.3.2 Experimental results for suspended rings . . . 33
2.3.3 Platonic solid assemblies . . . 37
2.4 Surface Evolver simulations of non-axisymmetric geometries . . . 40

3 Displacement-driven self-assembly **43**
3.1 Experimental setup . . . 44
3.2 Open prismatic structures . . . 46
3.2.1 Transient tile angle prior to prismatic assembly . . . 47
3.2.2 Effective radius of prismatic nets . . . 57
3.2.3 Reversibility of assembly . . . 58
3.3 Pyramidal structures . . . 60
3.3.1 Effective radius of pyramidal nets . . . 61
3.3.2 Reversibility of assembly . . . 62
3.4 Additional geometries . . . 63
3.5 Self-folding . . . 66

Conclusions **69**

Bibliography **73**

A Supplementary calculations **81**
A.1 Gravitational Effects . . . 81
A.2 Catenary solution of the axisymmetric minimal surface equation . . . 83
A.3 Force balance formulation of gravity-mediated assemblies . . . 85

B Open prismatic structures **87**

C Pyramidal structures **89**

List of Figures

1.1 Self-assembly on nanometer length scales . . . 6
1.2 Surface tension driven self-assembly on a liquid-gas interface . . . 7
1.3 Switchable self-assembly of capillary structures . . . 8
1.4 Surface tension driven self-folding of polyhedra . . . 9
1.5 Elastocapillary folding of a cube . . . 9
1.6 Self-folding on centimeter length scales . . . 10
1.7 Self-folding cube from μm to mm side lengths . . . 11
1.8 Acoustic forcing of a soap film . . . 12
1.9 Large scale soap bubbles . . . 13
1.10 Cubic particles absorbed at soap film interfaces . . . 13
1.11 Catenoid-like soap film examples . . . 14
1.12 Topological transitions of soap films . . . 15

2.1 Schematic of a minimal surface of revolution . . . 19
2.2 Contour plot of (2.1.11) for different values of R^* . . . 21
2.3 Existence of asymmetric catenoidal solutions phase space . . . 22
2.4 Surface Evolver refinement and iteration . . . 23
2.5 Force due to surface tension acting on a catenoidal boundary . . . 24
2.6 Axisymmetric suspended ring schematic . . . 25
2.7 Dimensionless phase space of (2.2.27) Solution . . . 29
2.8 Sections of contour plot in Figure 2.7 given constant values of B. . . . 30
2.9 Limiting behavior of (2.2.27) as B approaches one . . . 31
2.10 Sections of contour plot in Figure 2.7 given constant values of R^* . . . 31
2.11 Arrangement of cameras for imaging of gravity mediated assemblies . . . 32
2.12 Computer aided design drawings of soap film holder . . . 33
2.13 Instability of suspended rings . . . 35
2.14 Experimental results of suspended rings . . . 36
2.15 Deposition of square tiles onto a soap film . . . 37
2.16 Rotation of gravity-mediated cubic assembly . . . 38
2.17 Gravity-mediated platonic solid assemblies . . . 39
2.18 Simulation results of a cubic assembly . . . 40
2.19 Simulation results of tetrahedral, octahedral, and icosahedral assemblies 42

3.1 Displacement driven assembly experimental setup . . . 45
3.2 CAD drawings of polygonal bases used in displacement-driven assemblies 45
3.3 Open prismatic assemblies . . . 46

3.4 Transient tile angle schematic . . . 47
3.5 Dimensionless phase space of (3.2.14) solution for two base geometries . 50
3.6 Solutions of (3.2.14) for $B_t = 0$ and $B_t = 0.3$ . . . 51
3.7 Solutions of (3.2.14) for $B_t = 0$ and $B_t = 0.87$ . . . 52
3.8 Surface Evolver simulations of cubic assemblies . . . 53
3.9 Surface Evolver results of torque acting on a tile in a prismatic geometry 54
3.10 Simulation results for $B = 0.3$ and 0.87 . . . 55
3.11 Simulation results for $B_t = 0.54$ . . . 56
3.12 Displacement-driven prismatic structures with 2 cm heights . . . 57
3.13 Displacement-driven open prisms data . . . 58
3.14 Reattachment of hexagonal prism structure to soap film . . . 59
3.15 Displacement-driven pyramidal assemblies . . . 60
3.16 Displacement-driven pyramidal assemblies experimental data . . . 61
3.17 Reattachment of hexagonal pyramid structure to soap film, top view . . 62
3.18 Reattachment of hexagonal pyramid structure to soap film, side view . 63
3.19 Displacement-driven closed cube . . . 64
3.20 Displacement-driven pyramid atop a cube . . . 64
3.21 Displacement-driven octahedral assembly . . . 65
3.22 Displacement-driven closed octahedral assembly . . . 65
3.23 2D nets of self-folding structures . . . 66
3.24 Self-folding opposed to the direction of gravitational acceleration . . . 67
3.25 Self-folding perpendicular to the direction of gravitational acceleration . 68

4.1 Existence space of 3D self-assembly using a soap film . . . 70

A.1 Schematic of gravitational effects on circular soap film . . . 81
A.2 Results of gravitational effects on deflection of circular soap film . . . 82

B.1 Displacement-driven open prisms . . . 88

C.1 Displacement-driven triangular pyramids . . . 90
C.2 Displacement-driven square pyramids . . . 90
C.3 Displacement-driven pentagonal pyramids . . . 91
C.4 Displacement-driven hexagonal pyramids . . . 91

Introduction

0.1 Preface

Structures that make up the physical world are complex and elusive. The observations of these structures span the entirety of recorded history. The observers range from painters and sculptors to modern-day researchers. Observations are followed by discoveries that are thereby followed by understanding. As observers, we slowly unravel the processes dictating the physical system we inhabit and gain the knowledge associated therein. Patterns and geometric assemblies are found at any length scale, from molecules to galaxies, Whitesides and Boncheva [1] postulate. Regarding self-assembly, the scientific community has seen a sharp increase in the frequency of publications over the last 30 years as compiled by Mastrangeli and Perego [2] as well as Cui and Zhao [3]. The ability to interrogate the nanoscopic and microscopic regimes has led to many discoveries. At the same time, the control of components at such length scales continues to create novel self-assembled structures; the reviews of Arigaa et al. [4] and Iyer and Paul [5] outline many of these advancements. As the characteristic length scale of assemblies increases, the dominant force acting on the respective components changes. From nanometric to micrometric, the effects of van der Waals, electrostatic, and molecular forces dominate compared to the force due to gravity. A transition is often referenced regarding capillary systems where the force due to gravity is only comparable at sufficiently small length scales, namely the millimeter length scale, as the capillary length of most liquids is on the order of 2 mm, noted in the book of Jean Berthier [6]. Consequently, the dimensionless parameter Eötvós or Bond number, defined as a ratio of the capillary length and another characteristic length, is typically small in systems where capillary is the driving force. An important distinction to note is that capillary length is calculated with respect to a liquid-gas interface, so while a soap solution may have a capillary length of approximately 1.7 millimeters, a soap film membrane or soap bubble will exhibit a capillary length on the order of 3 meters, depending on its thickness as Cohen et al. [7] note in their work on giant soap bubbles. This thesis demonstrates the potential for assemblies on centimeter length scales where the competition of gravity, surface tension, and geometric constraints yields captivating structures. Specifically, this thesis presents the assembly of centimeter-scale tiles into suspended platonic geometries via a gravity-mediated process and prismatic and pyramidal displacement-driven assemblies by use of a pinch-off of a catenoid-like soap film. The applications of such structures include novel packaging methods, robotics, and electronics. The unique combination of a soap film substrate and non-patterned flat centimeter-scale tiles is shown to be a diverse system enabling the construction of

a variety of assemblies.

0.2 Motivation and Discovery

Many avenues of research have led to advancements in self-assembly capabilities. Progress concerning self-assembly produces new materials, new methods of fabrication and impacts a variety of fields. The development of such methods relies on technological resources and an understanding of the underlying physics. Some discoveries are coincidences, while others are the product of continued research progress. The methods and results presented in this thesis provide an additional avenue of research regarding self-assembly, and the work discussed is connected to a multitude of active research fields. The self-assembly paths presented in this thesis involve competition between geometric, capillary, and mechanical interactions, as pre-patterning is not necessary. Moreover, the use of a catenoid-like soap film as a substrate has no precedent. This unique approach creates a system in which geometrical effects stemming from the curvature of the film and physical effects stemming from capillary interactions combine to facilitate assembly. Another distinguishing feature of the method is that it can be harnessed in combination with gravity or imposed displacement. Most self-folding processes require the addition of heat, electromagnetic radiation, and other environmental changes [8–12]. Current methods for the assembly of polyhedral structures lack the means to construct centimeter-scale assemblies from independent components.

The traces of discovery regarding the self-assembly system presented started while investigating the behavior of an acetone droplet in a Leidenfrost state deposited onto an air-water interface as proposed by Janssens et al. [13]. The interaction of the acetone droplet with the supporting interface exhibited many fascinating phenomena. The influence of Marangoni propulsion, capillary-gravity waves, and interfacial effects make the system increasingly complex [14–18]. As such, a series of simplifications were considered to reduce the complexity and allow further investigation. Firstly, removing Marangoni effects and maintaining a constant surface tension, a system reminiscent of coupling a moving liquid-gas interface with static obstacles. Secondly, consider the interface to be static along with the obstacle, as the fundamental solution of the larger system should encompass this simple case. The problem is now one of capillarity, with significant research done over hundreds of years, with new questions arising to this day. Consider the capillary rise of a liquid-gas interface around a thin plate, a glass microscope cover-slip with thickness ranging from $0.13 - 0.17$mm, arranged perpendicular to the quiescent interface. The system is now only dependent on the geometry of the obstacle/cover-slip, surface tension, and hydrostatic pressure. To isolate the effect due to surface tension, a soap film generated across a ring was used experimentally. As the cover-slip pierces the soap film membrane with the surface of the soap film perpendicular to the wide face of the cover-slip, the familiar capillary rise does not occur due to the symmetry of the soap film. As the angle between the cover-slip and the bounding ring of the soap film changes, the interaction of the soap film and the cover-slip shows a moving contact line of similar shape to the previous experiments with a liquid-gas interface at varying surface tensions. As the relative angle between the cover-slip and the ring bounding the soap film approaches zero, the soap film seems

to align with the edges of the cover-slip. With the boundary of the soap film coinciding with the edges of the square cover-slip, a catenoid-like soap film can be seen as the cover-slip is displaced from the supporting frame. Once the cover-slip was released, I noticed that instead of passing through the soap film or causing it to rupture, as Stogin et al. [19] detailed, the tile was suspended within the soap film. The addition of components confirmed the robustness of the system. A model was derived for an axisymmetric system to describe the experimentally realized assemblies. As a tile could be supported within an initially quiescent soap film, the next step was the deposition of centimeter-scale tiles onto a catenoidal soap film. The symmetry of the system permits the construction of prismatic, pyramidal, and octahedral geometries resting on a base at centimeter-length scales. Using the pinch-off behavior of a catenoidal soap film, structures separate from the initial film were constructed. The impact of the suspended tiles within the catenoidal soap film is encompassed in the effective radii of the base corresponding to the various structures.

0.3 Organization of the Thesis

The following chapter details pertinent background information regarding self-assembly systems and soap films. A calculus of variations approach is presented in Chapter 2 to describe the simplified system of a ring suspended within a soap film. The proposed solution in Chapter 2 is compared to experimental results, and the potential of gravity-mediated assemblies in the likeness of platonic solid geometries is discussed. Numerical simulations using Surface Evolver are used to compare the equilibrium of the gravity-mediated assemblies to the proposed axisymmetric model. Extending the gravity-mediated assemblies to free-standing displacement-driven assemblies via pinch off-phenomena is demonstrated in Chapter 3. A model for the angle of a rectangular tile suspended within a soap film while one edge is attached to a base is proposed and compared to experimental results. Surface Evolver simulations of a prismatic assembly in progress, similar to the proposed model, are presented and compared to the experimental results. The construction of prismatic, pyramidal, and octahedral structures by the displacement-driven method is accompanied by corresponding effective radii such that the pinch-off phenomena correspond to the theory presented in Chapter 2. Combinations of prismatic and pyramidal structures are also presented, along with experiments demonstrating the potential of self-folding in the context of displacement-drive assemblies within a soap film. Lastly, a concluding chapter brings together the self-assembly methods described in Chapters 2 and 3 into a phase space of existence. The concluding remarks also detail potential future work and applications.

Chapter 1

Background

Self-assembly and self-folding are broad categories of methodologies observed in nature as well as implemented in modern material science. This chapter will outline the distinctions between self-assembly and self-folding while introducing the relevant state-of-the-art research. The final section of this chapter will detail soap film membranes as idealized capillary systems with surprising robustness. A discussion pertaining to topological transitions in the context of soap films will lay the foundation for the pinch-off phenomenon referenced in subsequent chapters.

1.1 Self-assembly

Self-assembly is commonly described in the literature as the process by which individual components form an organized structure. For example, the book of John A. Pelesko [20] defines the process of self-assembly as follows:

> **Self-assembly** *refers to the spontaneous formation of organized structures through a stochastic process that involves pre-existing components is reversible and can be controlled by the proper design of the components, the environment, and the driving force.*

Although the vast majority of the work on this topic is concerned with the fabrication of nanometer and micrometer-scale structures, Whitesides & Boncheva [1] point to the potential value of self-assembly at larger scales, centimeter included. Furthermore, the interest pertaining to self-assembly at centimeter and larger length scales is extensively found in recent publications as well as books on the topic [20–22].

1.1.1 Sub-millimetric scale assemblies

Figure 1.1 details only one of the multiple self-assembly systems involving nanometer-scale components; on the nanometer and micrometer length scales, self-assembly has been investigated for many years. The image in Figure 1.1 is reproduced from the work of Gu et al. [23] and depicts the assembly of 200 nm long rods into bundles and chains. Molecular self-assembly is also a prolific field of study on such length scales.

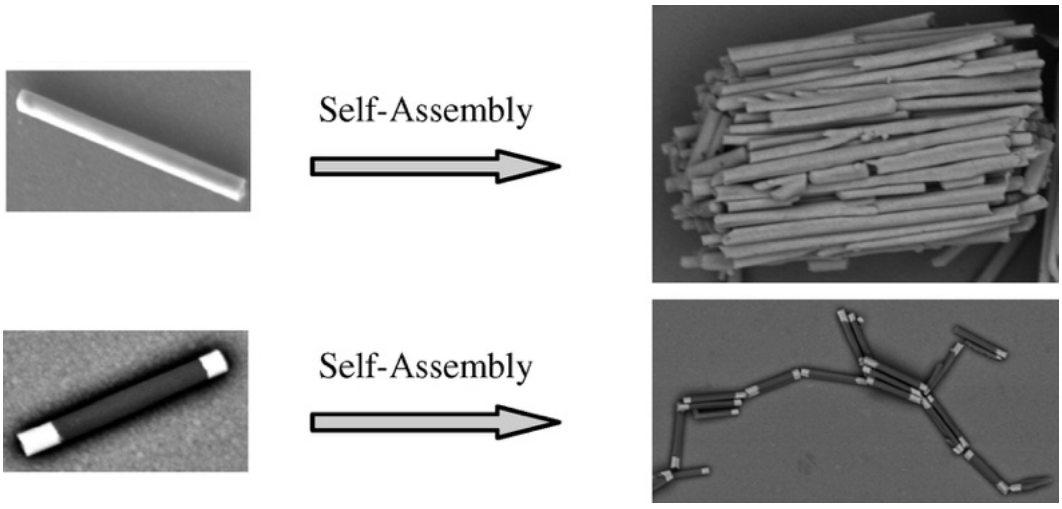


Figure 1.1: The image is reproduced from the work of Gu et al. [23]. The self-assembly of independent 200 nm long rods into bundles and rows. Similar results have been shown in the work of Botto et al. [24] and Lewandowski et al. [25] regarding the assembly of micrometer-scaled cylindrical particles into chains.

Terfort et al. [26] demonstrated the possibility of millimeter-scale assemblies as early as 1997 by use of components agitated in a closed environment until multiple assemblies were observed. Typically these assemblies are limited to two-dimensional structures; the work of Tien et al. [27] is an example. Or, as Park et al. [28] describe in their 2004 work, conglomerates of many three-dimensional components. By functionalizing the edges of the components, the final assembly can be tuned to exhibit various emerging structures.

1.1.2 Capillary self-assembly

Capillarity, or surface tension, driven self-assembly has been studied for decades, the "Cheerios effect" being an example from as early as 1979 pioneered by the work of Chan et al. [34]. The more recent works of Hosokawa et al. [33] and Vandewalle et al. [32] rely on the fabrication of floating objects that have 3D geometric properties or functionalized edges and produce two-dimensional assemblies of discrete components on centimeter length scales. Figure 1.2 depicts the primary operative interactions of surface tension driven self-assembly on a liquid-gas interface, and Figure 1.3 a particular set of experiments from the work of Vanderwalle et al. [32] implementing the capillary attraction detailed in (c) of Figure 1.2. The experiments of Hosokawa et al. [33] are the precursors to those of Vanderwalle et al., as predominantly, the shape of the floating tiles was modified to enable the sharpest edges to meet at a point. The work of Bowden et al. [30] demonstrates the use of the component interactions depicted in panel (a) of Figure 1.2.

The assembly of colloidal particles on small length scales continues to be a prolific field of study as demonstrated in the works of Botto et al. [35], Ni et al. [36], and Lui and Li [37], all dealing with nanoparticle assemblies. The operative interactions of assembly presented in this thesis are reminiscent of those described by Liu et al. [38],

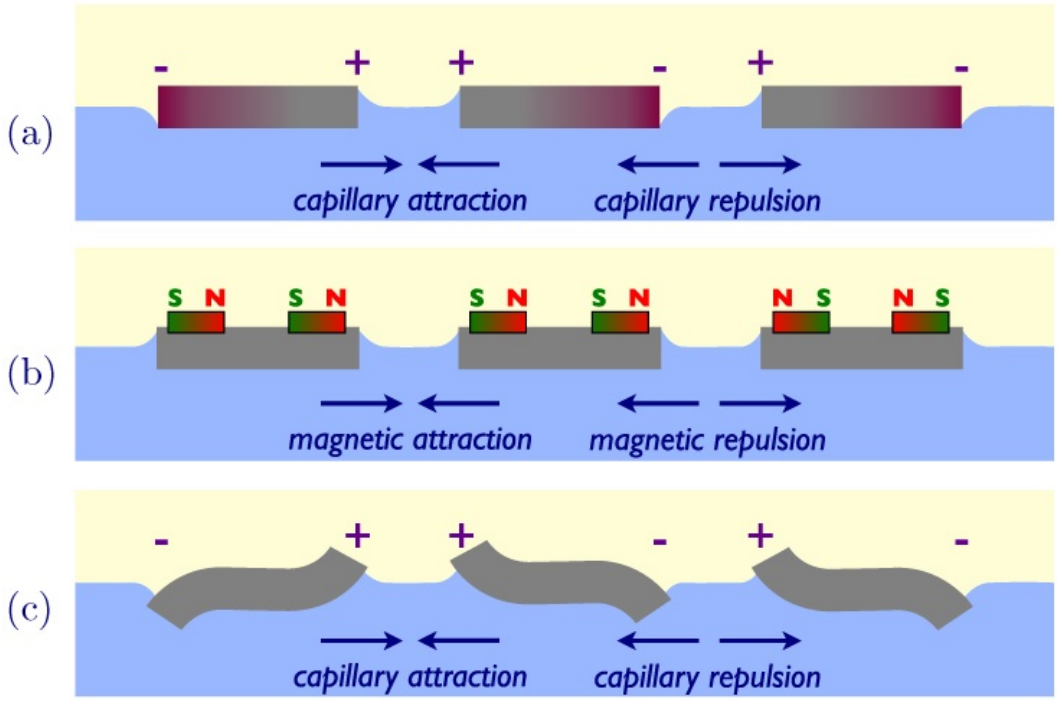


Figure 1.2: The image is reproduced from the work Poty et al. [29]. Each row (*a*), (*b*), and (*c*) details the use of functionalized components in the self-assembly on capillary surfaces. Namely, hydrophobicity/hydrophilicity, magnetic interactions, and non-planer shape distortions, respectively. The effect of the "Capillary Bond" as described by Bowden et al. [30] is a good example of the interactions detailed in (*a*). Grzybowski et al. [31] demonstrate the assembly of structures using operating principles as seen in (*b*). An example of the interactions seen in (*c*) are found in the work of Vanderwalle et al. [32] by the design of non-planer floating components varying two-dimensional structures or patterns can be assembled. In addition to these modifications, the in-plane shape of the components also constrains the resulting assembled structures, as seen in the work of Hosokawa et al. [33].

where assemblies arise as a result of the curvature of a fluid interface. Almost all surface tension-driven assemblies are restricted to two-dimensional patterns, and very few others can accommodate structures on the scale of centimeters. Capillary effects are commonly compared with gravitational effects only at sufficiently small length scales, say below a few millimeters, as seen in the work of Poty and Vandewalle [39].

Figure 1.2 showcases the predominant design choices that drive two-dimensional self-assembly on an interfacial medium. Figure 1.3 alternatively demonstrates that within the constraints of assembly on an interface, the possibility for emergent structures that make use of capillary forces is diverse and surprising. But self-folding can also be driven by surface tension, as is described in the following section.

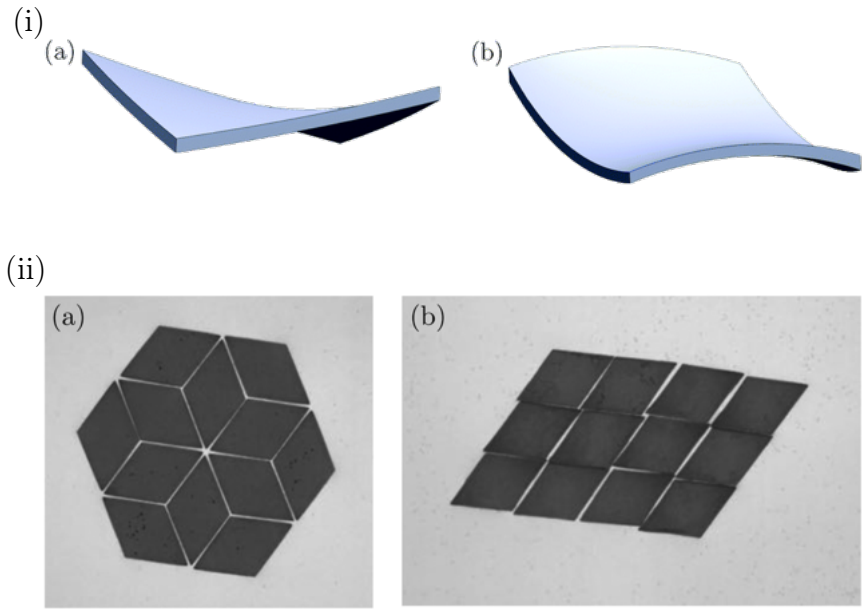


Figure 1.3: As detailed in the work of Vanderwalle et al. [32] by the design of non-planer floating components, varying two-dimensional structures or patterns can be achieved. Each rhombus seen in (*ii*) has an edge length of 1cm and corresponds to the respective shapes seen above in (*i*). A notable aspect of this work is that at a defined temperature, the 3D shape of each component changes, and thereby the realized assembly is reconfigured.

1.2 Self-Folding

Compared to self-assembly as defined in the previous section, self-folding does not comprise independent components but instead, as the name suggests, the automated folding of two-dimensional patterns into three-dimensional structures. Reminiscent of origami instructions, self-folding typically refers to a hinged structure, where each hinge corresponds to a crease instruction within an origami manual. Self-folding methods without prescribed hinges have been studied by Py et al. [40] as well as Geraldi et al. [41] within their work on "Capillary Origami." As this thesis makes use of rigid tiles for the proposed self-assembly method, self-folding within this thesis will refer to the construction of three-dimensional structures from pre-patterned two-dimensional nets of the structures to be realized.

1.2.1 Small scale folding

The distinction between self-folding and self-assembly is adequately demonstrated by comparing Figure 1.1 and Figure 1.4. The self-folding method depicted in Figure 1.4 makes use of the capillary force acting on a hinge by liquid solder under a change in the environmental temperature; the image is reproduced from the work of Kaplan et al. [9]. Figure 1.5 alternatively depicts repeated folding of a cubic structure by precisely controlling the volume of a water droplet interacting with the four hinged squares. Legrain et al. [42] further investigated other prismatic structures in their 2014 work. While self-folding produces three-dimensional assemblies from two-dimensional templates, the ini-

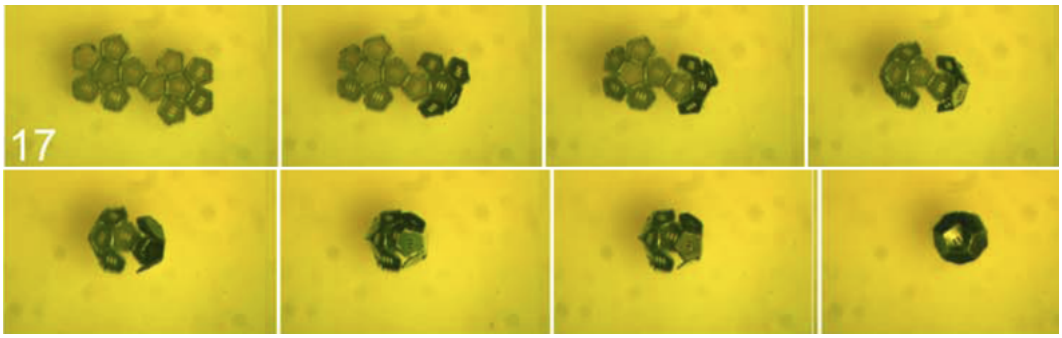


Figure 1.4: The image is reproduced from the work Kaplan et al. [9]. The self-folding process shown is driven by the liquid solder deposited at the edges of the dodecahedral net and the changing temperature of the medium; each edge length is 300 μm. While the process of self-folding depicted is a significant advancement, the selection of the appropriate two-dimensional net poses an interesting question; out of the 43,380 distinct net representations of a dodecahedron which is the most suitable for the self-folding process demonstrated. Kaplan et al. describe the dominant intermediaries to reduce this problem and isolated 21 nets to study the yield of polyhedra construction; the method numbered 17 is given as an example. Leong et al. [8] detail these design considerations regarding a cubic structure and the ideal solder volume for appropriate folding angles.

tial production of such templates limits the types of assemblies achieved. The precise control of environmental factors should also be considered as many such processes occur at narrow temperature windows or chemical concentrations. Self-assembly, on the other hand, especially on nanometer length scales, predominantly produces aggregates of functionalized components under similar conditions as those required in self-folding processes.

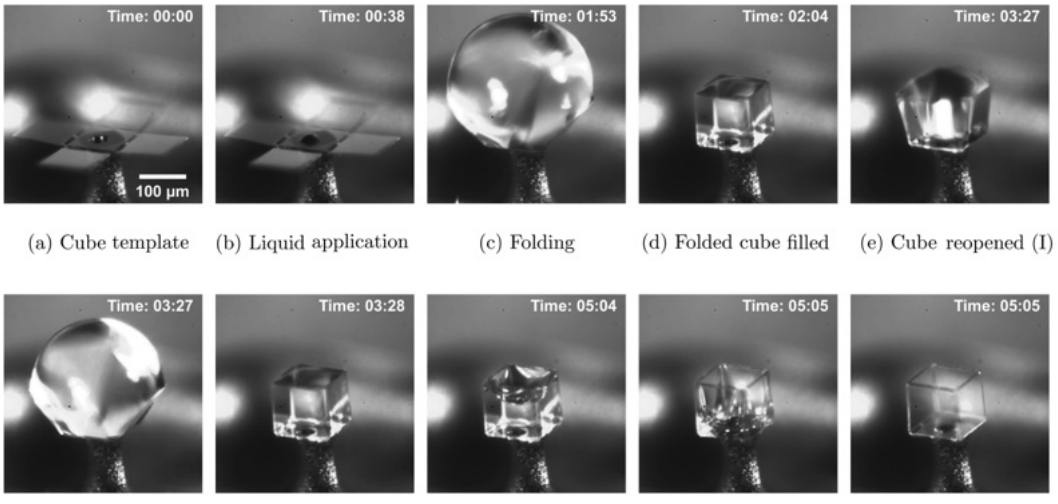


Figure 1.5: The image is reproduced from the work of Legrain et al. [42]. It depicts the repeatable folding of a cubic structure by use of through-wafer filling. The controllable elastocapillary folding described makes use of the edge pinning properties of water and the precise control of the water volume.

1.2.2 Mesoscale and large scale self-folding

The work of Callens et al. [43] and Boncheva et al. [44] pertain to mesoscopic self-folding of linked components as seen in Figure 1.6. Boncheva et al. [44] detail self-folding paths involving competition between mechanical and magnetic interactions, while Callens et al. [43] alternatively developed self-folding methods for fabricating three-dimensional structures from planar linkages spanned by latex sheets. Some of the achieved structures are seen in Figure 1.6, and they range in size from a few millimeters to a few centimeters.

Figure 1.7 is reproduced from the work of Leong et al. [8], investigating the self-folding of polyhedra at multiple length scales. Using a similar methodology to that found in the work of Kaplan et al. [9] a much broader size range of structures was realized. The images in Figure 1.7 show that surface tension-driven assembly methods could be extended to even larger sizes, and there is a distinct interest in the construction of even larger structures. Song et al. [12] demonstrate an inverted system yielding centimeter-scale and even meter-wide assemblies of two-dimensional pen drawings submerged in water to generate 3D structures by surface tension driven detachment followed by solidification at a fluid interface.

(i) (ii)

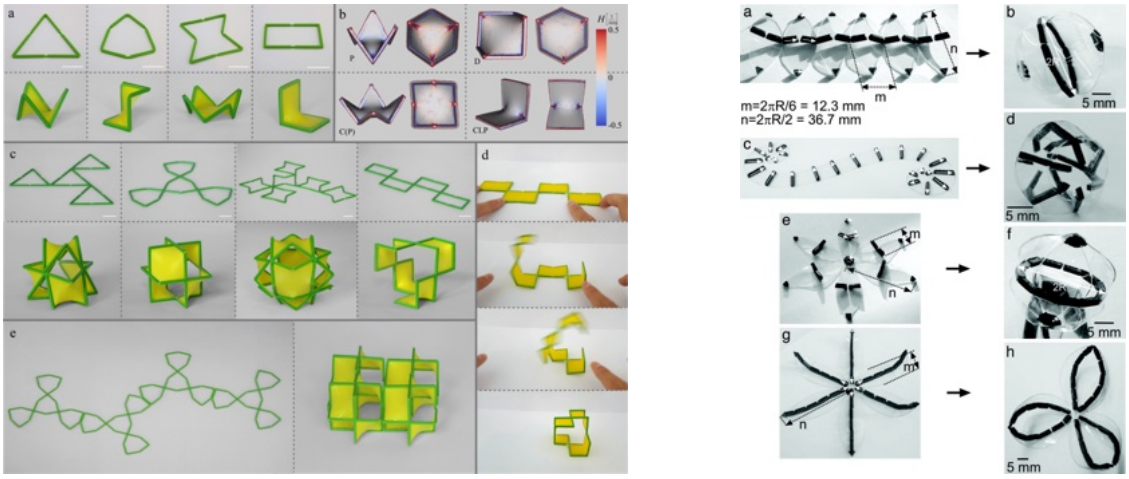


Figure 1.6: Self-Folding geometries on centimeter-length scales. (*i*) showing the work of Callens et al. [43], which demonstrates the use of pre-strained elastomer sheets as a driving force of self-folding on specifically designed frames. (*ii*) showing the work of Boncheva et al. [44] making use of the competition between mechanical and magnetic interactions.

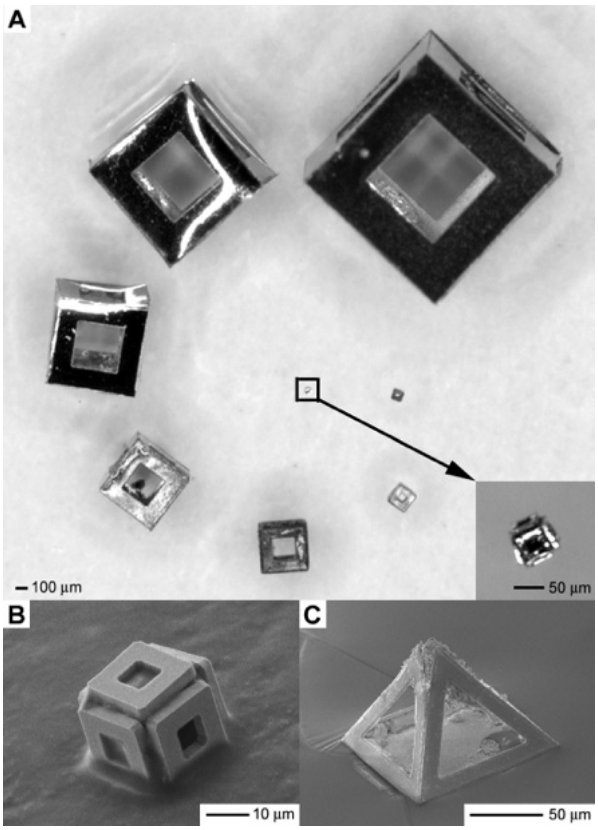


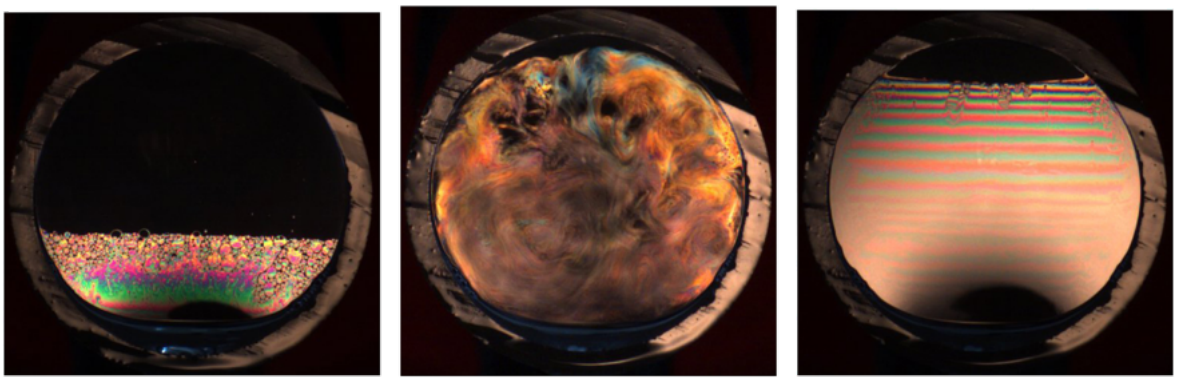
Figure 1.7: Multiple self-folding cubes ranging from 10 μm to 1 mm side lengths, reproduced from the work of Leong et al. [8]. These experiments demonstrate that a liquid solder based surface tension-driven self-folding process can fold structures up to 2 mm in size. This shows that with the appropriate system and methodology, capillary forces can facilitate assemblies on larger length scales.

1.3 Soap Films

Soap films have fascinated scientists and students alike for over a hundred years. Boys [45] demonstrated many beautiful and interesting properties of soap films in his 1890 book, as did Courant [46] 50 years later, and the applications of soap films continue to appear in a multitude of fields to this day.

1.3.1 Film thickness and longevity

Figure 1.8 demonstrates three main topics concerning soap films: draining, mixing, and thinning. Immediately following the generation of a soap film, be it in bubble form or bounded by a frame, the surface is observed to be somewhat chaotic, somewhere between turbulence and convective currents. Soap films are often used to study two-dimensional fluid dynamics; Vorobieff et al. [48] characterized two-dimensional turbulence using soap films, while Chomaz and Cathalau [49] investigated soap films as classical fluids. Regarding soap films bounded by a rigid frame oriented such that the force due to gravity is acting parallel to the film, as seen in Figure 1.8, the water within the membrane flows along the direction of gravitational acceleration. This is quite natural as water is often observed to flow downhill, but it is precisely this flow



(a) (b) (c)

Figure 1.8: Mixing a vertically oriented soap film via acoustic agitation to prevent draining influenced rupture reproduced from the work of Gaulon et al. [47]. Images are approximately 1s apart and the interior diameter of the bounding cylinder is 26 mm. (a): a film following the draining of the contained liquid towards the bottom, the film is still spanning the tube, but the black film is too thin to be imaged. (b): a film in the process of mixing by use of music being played at the other end of the tube bounding the soap film. (c): a film in the thinning process, note the black film forming at the top. Following mixing, bands of colors known as Newton's shades are visible as the thickness of the film varies from top to bottom.

that leads to the image seen in Figure 1.8(a). As the water drains, the thickness at the bottom of the film is much larger than that at the top. The black part of the soap film in Figure 1.8(a) is referred to as black film, or Newton Black film, and it appears that way because its thickness is less than 100 nm. In Figure 1.8(c), we observe clear bands of different colors due to the internal refraction of visible light. Each color band corresponds to a distinct film thickness; the bands are known as Newton's shades as he first described the phenomena in *Opticks* [50]. And so, as the first panel of Figure 1.8 corresponds to the draining of the soap film, and the third to thinning, Figure 1.8(b) consequently refers to the mixing of a soap film. In the work of Gaulon et al. [47] the mixing is initiated by acoustic forcing, i.e., playing music into the tube bounding the soap film. By mixing a soap film, the water within it is redistributed, and the possibility of rupture due to the film thinning is greatly diminished. The study of film thinning and longevity includes the work of Champpougny et al. [51] investigating the effects of humidity, as well as the work of Berg et al. [52] focusing on drainage in microscale soap films.

Stogin et al. [19] have also shown that liquid membranes can be highly stable; such soap film membranes act as inverse sieves where small particles can be suspended while larger particles pass through without breaking the membrane. And the ongoing study of foams has relied on advancements in understanding the interactions of soap films and their corresponding boundaries [55–57]. Given that soap films exhibit such robustness, it is only natural that soap films could be made much larger than a few centimeters. Figure 1.9 depicts an image of a giant soap bubble from the work of Cohen et al. [7]. Generated atop a soap solution bath, the bubble is almost one meter tall with a radius 10 cm larger than the height. On such length scales, the contribution of the force due to gravity is no longer negligible. Note that the height of the bubble is smaller than its horizontal radius. This work shows that soap films and liquid membranes are not

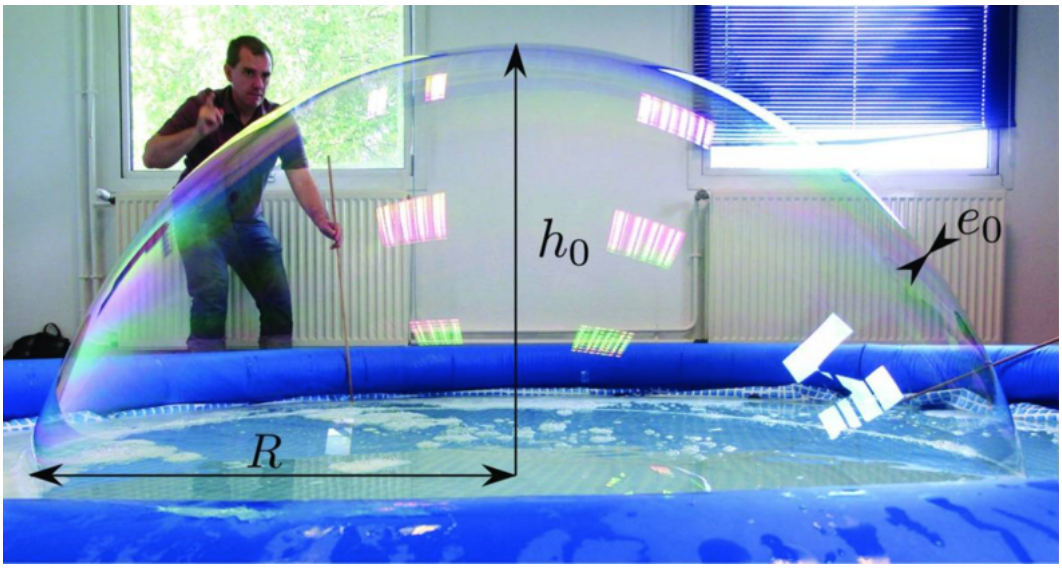


Figure 1.9: The image is reproduced from the work Cohen et al. [7] showing the potential of large-scale soap bubbles and the corresponding shapes taken. Here, $R = 1.09$m, and $h_0 = 0.97$m the thickness of the film is measured following the bursting technique described by McEntee and Mysels [53] and $e_0 \approx 0.81\mu$m. Brubaker [54] has further developed the theoretical analysis of large-scale bubbles in the subsequent work.

restricted to sub-centimeter length scales where the Bond number is sufficiently small.

Figure 1.10 is reproduced from the research of Davies and Raufaste [58] from 2021. This work studied the orientation of a cube with varying mass suspended within a soap film. It shows the feasibility of suspensions counteracting the force due to gravity within a soap film, as well as the potential for self-alignment. The interaction of a sphere falling through a soap film has also been studied using experimental and numerical experimentation by Chen et al. [59] as well as Cox and Davies [60].

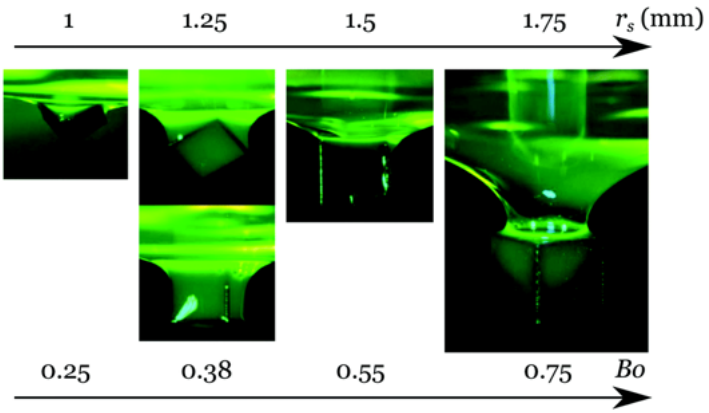


Figure 1.10: The image is reproduced from the work Davies and Raufaste [58]. While recording the suspension of a cube within a soap film Davies and Raufaste observed the changing orientations of cubes with a Bond number less than one. The experimental results correspond to the previous computational work of Davies [61] on super-quadratic objects suspended within or passing through a soap film.

1.3.2 Topological transitions

This thesis focuses on a particular class of soap film geometries, catenoid or catenoid-like soap films, like those seen in Figure 1.11. The catenoid was the first minimal surface discovered apart from the plane, described in the 1740s by Leonhard Euler [66]. The properties and kinematics of catenoids are of paramount importance in a variety of applications, as seen in research on transport through vesicle walls by Frolov et al. [67], and studies of vesicle necking by Chabanon and Rangamani [68]. The analysis of static catenoid-like soap films is an ongoing research direction. In 2021, Alimov et al. [69] extended previous results regarding mirror-symmetric frames, Figure 1.11(ii), to include noncircular and asymmetric frames. This thesis corresponds well to the theoretical predictions and expands the potential geometries to be investigated. Describing the dynamic behavior of catenoid pinch-off is seen in the work of Robinson and Steen [70] as well as the recent work of Goldstein et al. [71]. In addition to the pinch-off of a catenoidal soap film into two disjoint films, more geometrically complex transitions have also been observed. Goldstein et al. [72] have investigated a soap film representation of a Möbius strip. Through a smooth deformation of the bounding curve, the soap film undergoes a topological transition where the initially one-sided film transforms into a two-sided film as depicted in Figure 1.12. Under a continuous deformation of the bounding curve, a change in the geometry is observed, and Moffatt et al. [73] quantified this phenomenon. Extending these results, the work of Hutzler et al. [74] investigated topological transitions of soap films bound by prism geometries. While the topological transition found in this thesis is of the simplest sort, a pinch-off, it nonetheless corresponds to a nontrivial change in the surface of the soap film.

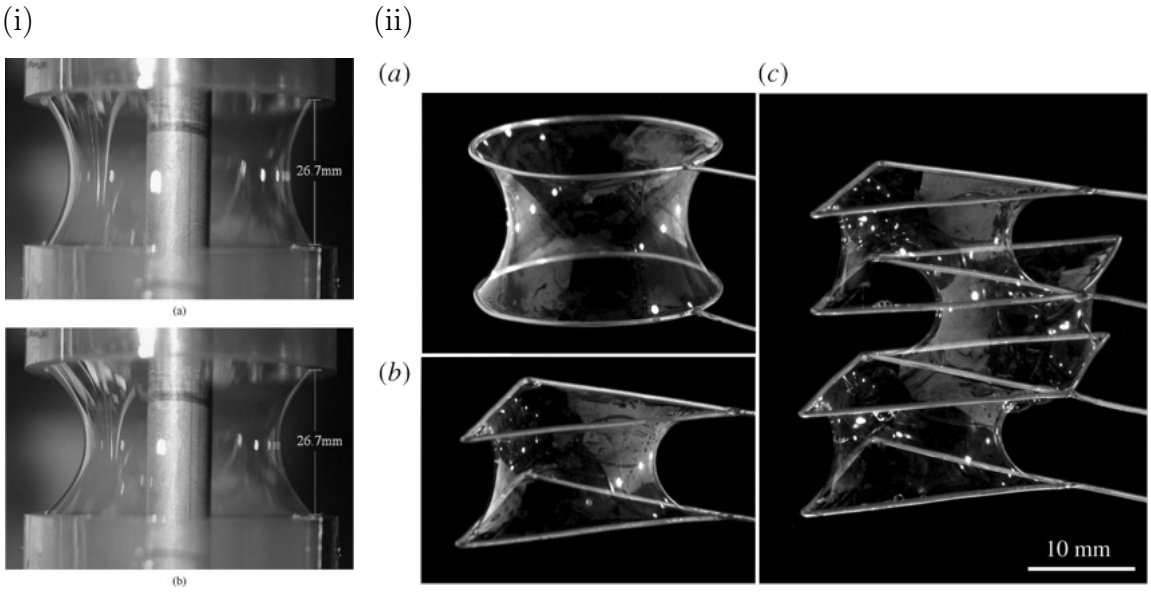


Figure 1.11: (i) shows the effect of a magnetic field on a soap film generated between two rings, membrane profiles at voltages 0 and 3kV in (a) and (b) respectively. Similar studies have investigated the effect of an electric field on transport phenomena within a soap film [62, 63]. (ii) contains examples of soap film bridges between mirror symmetric frames and the corresponding periodic surfaces generated. Images denoted by (i) and (ii) are reproduced from the work Moulton & Pelesko [64] and Alimov et al. [65], respectively.

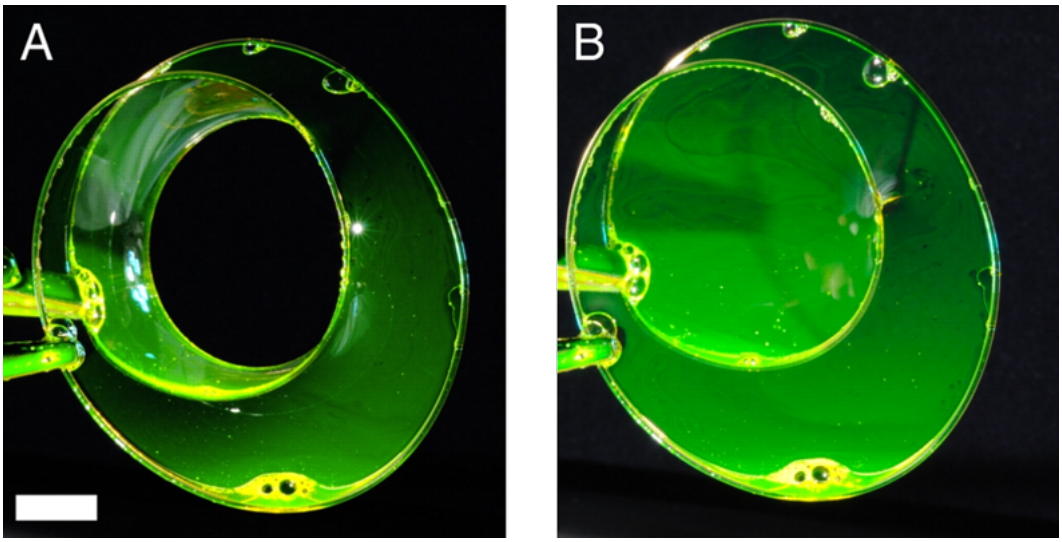


Figure 1.12: Images A and B are reproduced from the work of Goldstein et al. [72] showing a soap film representation of a Möbius strip, the scale bar seen in A is 2cm. Through a smooth deformation of the bounding curve, the soap film seen in A undergoes a topological transition where the initially one-sided film transforms into a two-sided film seen in B. Extending these results, the work of Hutzler et al. [74] investigated topological transitions of soap films bound by prism geometries.

Chapter 2

Gravity-mediated self-assembly

In this chapter, consider self-assembly processes that begin by freely distributing two-dimensional tiles with various polygonal shapes and dimensions ranging from mm to cm on a soap film that spans a circular ring of radius 5 cm. The assembly mechanism is the result of gravitational and surface tension forces acting on the tiles at room temperature and pressure. In contrast to the self-assembly of mesoscale (mm-cm) structures on liquid-air interfaces that have been demonstrated in the works of Poty et al. [29], Bowden et al. [30], Hosokawa et al. [33], among others, the method presented in this chapter does not require that the system be agitated or that the surfaces or edges of the components be functionalized. The interactions between a soap film and two-dimensional tiles dispersed and suspended within it yield robust three-dimensional Platonic solid-like structures. The shape changes that a soap film undergoes as these structures form are fascinating.

A limiting factor of the assembly method presented in this chapter is that the soap film carries the weight of the tiles without rupturing. Namely, the cohesive force due to the surface tension of the soap film must be equal to the net gravitational force acting on all tiles distributed on the soap film and subsequently self-assemble into a suspended structure. The shape of a soap film suspended by a circular ring and carrying a self-assembled structure is challenging to determine. The problem of finding the shape of a soap film that spans a rigid wireframe, also known as the problem of Plateau [75], has a rich history within the mathematical study of minimal surfaces. The first proof of the existence of a minimal surface bounded by a given closed space curve that does not intersect itself is due to Douglas [76] and resulted in a Fields medal in 1936. This chapter will not delve into the intricacies of such generalized minimal surfaces; instead, it will consider a simple ring. The shape of the soap film spanning a ring is a flat circular disk bounded by the ring. All structures presented in this chapter are assembled by deposition of tiles onto a planar circular soap film spanning a bounding ring. A catenoid closely approximates the shape of the soap film following assembly. Therefore, an axisymmetric model of a ring suspended within a soap film is considered. The derived model and analysis determine an effective carrying capacity of a soap film. Experimental results validate the theoretical predictions of soap film deflection by a suspended ring. Numerical simulations using Surface Evolver [77] are introduced to show that assembled Platonic solid-like geometries correspond to effective radii within the axisymmetric model.

Section 1 provides a detailed review of the classical catenoid solution to the minimal surface problem. The analytical criterion for the existence of a catenoid solution is compared to predictions based on Surface Evolver simulations as a first confirmation of the validity of the numerical representation of the soap film. Additionally, the force due to surface tension acting on a ring of radius less than that of the supporting ring is determined analytically. It is used to further validate the Surface Evolver simulations.

In Section 2, the classical catenoid solution presented in Section 1 is extended to derive a closed-form expression for the carrying capacity of a soap film. Using the calculus of variations, the ordinary differential equation governing the existence of an axisymmetric minimal surface is reproduced along with an additional nonlinear Neumann condition on the suspended ring. The existence and properties of this generalized solution are explored.

Section 3 presents the procedure used for soap film experiments conducted in this research, highlighting its robustness while carefully delineating all significant sources of error. Experimental results of 3D printed toroidal rings suspended within a soap film are compared to results from the model presented in Section 2. Lastly, illustrative examples of the three-dimensional Platonic solid-like structures obtained using the gravity-mediated method are presented.

In Section 4, Surface Evolver simulations demonstrate that even non-axisymmetric self-assembled structures closely resemble the theoretical predictions of suspended toroidal rings. Experimental data agree nicely with the simulation results, and the existence of an effective radius of such structures is demonstrated.

2.1 Classical catenoid solution

A mathematical description of the catenoid, which is the only minimal surface of revolution besides the plane, was first provided by Euler in 1744 [66]. The study of minimal surfaces arose naturally in conjunction with the development of the calculus of variations and was pioneered by Lagrange [78] beginning in 1762. A surface $\mathcal{S} \in \mathbb{R}^3$ is minimal if and only if the mean curvature H satisfies $H = 0$ at each point of $\mathcal{S}$. This condition is equivalent to the requirement that, relative to some Cartesian coordinate system, each point (x, y, z) of $\mathcal{S}$ can be represented locally in the form $(x, y, f(x, y))$, where f satisfies the second-order elliptic partial-differential equation

$$0 = \left(1 + \left(\frac{\partial f}{\partial y}\right)^2\right) \frac{\partial^2 f}{\partial x^2} - 2\frac{\partial f}{\partial x}\frac{\partial f}{\partial y}\frac{\partial^2 f}{\partial x \partial y} + \left(1 + \left(\frac{\partial f}{\partial x}\right)^2\right) \frac{\partial^2 f}{\partial y^2}. \tag{2.1.1}$$

To restrict the necessary conditions for a minimal surface to a surface of revolution, consider two circular rings, with radii R_i and $R_o \geq R_i$, contained in parallel planes separated by a finite distance and oriented coaxially, as depicted in Figure 2.1. Finding a minimal surface spanning the rings can be simplified into a one-dimensional problem. Given a curve between two points contained in the (x, z)-plane of a standard (x, y, z) Cartesian coordinate system, with associated right-handed orthonormal basis $(\boldsymbol{\imath}, \boldsymbol{\jmath}, \boldsymbol{k})$, the corresponding surface of revolution is given by a 2π rotation of the curve about the z-axis. Let (r, z, θ) denote the cylindrical-polar coordinates of an arbitrary point with

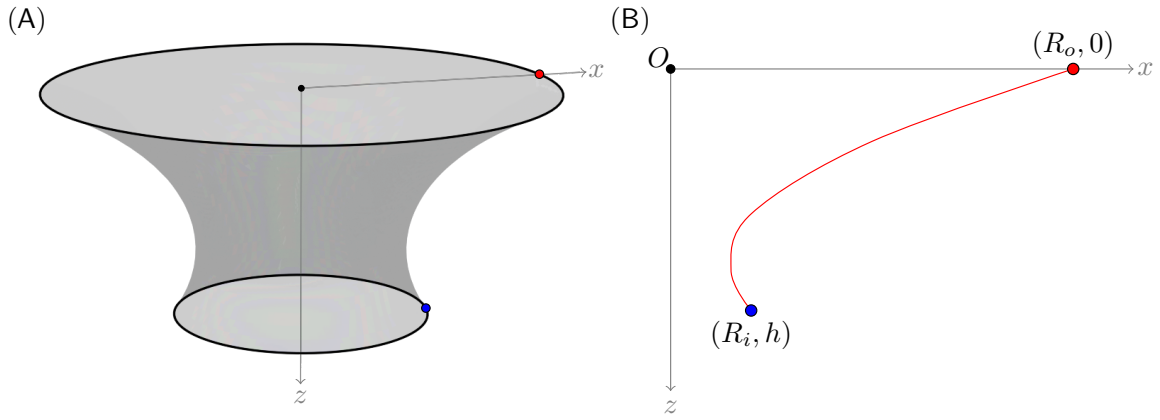


Figure 2.1: A 3D view of the geometry is shown on the left with x and z axes drawn. In the plane defined by the axes, the geometry can be represented as a curve, seen on the right. Without loss of generality, the points defining the boundary are denoted as (R_i, h) and $(R_o, 0)$.

Cartesian coordinates (x, y, z) such that

$$r = \sqrt{x^2 + y^2} \geq 0 \quad \text{and} \quad \theta = \arctan \frac{x}{y}, \tag{2.1.2}$$

where the principal branch of the inverse tangent is used to define the angle $0 \leq \theta \leq 2\pi$. Define R as a function of z to denote the red curve seen in Figure 2.1, this function evaluated at $R(0)$ and $R(h)$ corresponds to the endpoints of the curve at R_o and R_i, respectively. Figure 2.1 shows a three-dimensional representation of a membrane-spanning two rings and a corresponding two-dimensional section. Considering a surface constrained to be axisymmetric, as depicted in Figure 2.1, the local condition (2.1.1) can be written as

$$0 = 1 + (R')^2 - RR'' \qquad \text{for } 0 < z < h. \tag{2.1.3}$$

The ordinary differential equation (2.1.3) is the axisymmetric minimal surface equation and can also be found by minimizing the area functional of a surface of revolution. This equation is to be solved subject to Dirichlet boundary conditions that apply to the two rings, namely

$$\begin{cases} R_i = R(h), & (2.1.4) \\ R_o = R(0). & (2.1.5) \end{cases}$$

(2.1.3) can be reduced to a first-order ordinary differential equation by applying a substitution. Following two integrations, a representation for $R(z)$ involving two constants of integration is found. The particular calculations can be found in Appendix

A.2. Therefore the boundary value problem (2.1.3)–(2.1.5) is equivalent to:

$$\begin{cases} R(z) = \dfrac{\cosh(\sqrt{C_1}(z - C_2))}{\sqrt{C_1}}, & (2.1.6) \\ R_i = \dfrac{\cosh(\sqrt{C_1}(h - C_2))}{\sqrt{C_1}}, & (2.1.7) \\ R_o = \dfrac{\cosh(C_2\sqrt{C_1})}{\sqrt{C_1}}. & (2.1.8) \end{cases}$$

Focusing on (2.1.7) and (2.1.8), note that C_2 can be isolated. The system can be nondimensionalized by dividing $R(z)$ and z by R_o, where $r^* = R/R_o$ and $z^* = z/R_o$. Evaluating these substitutions gives

$$\begin{cases} r^*(z^*) = \dfrac{\cosh(R_o\sqrt{C_1}z^* - \cosh^{-1} R_o\sqrt{C_1})}{R_o\sqrt{C_1}}, & (2.1.9) \\ R^* = \dfrac{\cosh(R_o\sqrt{C_1}h^* - \cosh^{-1} R_o\sqrt{C_1})}{R_o\sqrt{C_1}}, & (2.1.10) \end{cases}$$

where R^* is a dimensionless radius defined by the ratio of the smaller ring and the larger ring, and h^* is the separation distance along the z-axis divided by the radius of the larger ring. The nondimensionalization of a catenoidal soap film typically assumes the radius of the larger ring to be a multiple of the radius of the smaller ring, as described in the work of Salkin et al. [79]. Throughout this thesis, R^* is used to ensure that the range of the non-dimensional parameter is finite. As C_1 is a constant, it is convenient to introduce $c = R_o\sqrt{C_1}$, after which (2.1.10) can be written as

$$R^* = \frac{\cosh(ch^* - \cosh^{-1} c)}{c}. \tag{2.1.11}$$

Given values of R^* and h^*, c can be determined numerically from (2.1.11) whereby the solution of the catenoid as a minimal surface of revolution can be fully expressed. Note that for certain combinations of R^* and h^*, there does not exist a value of c such that (2.1.11) is satisfied. This issue is taken up in the next section.

2.1.1 Exsistence criterion of catenoidal solutions

The existence of solutions of (2.1.11) given R^* and h^* is expanded upon in Figure 2.2, the graph of which shows various contours of (2.1.11) given constant R^*. The range of R^* is from $R^* = 0$ to $R^* = 1$ due to the chosen non-dimensionalization. For the derivation of the existence criterion, the maximal value of h^* must be found. As such, consider the consequence of requiring that the derivative of (2.1.11) with respect to c vanishes.

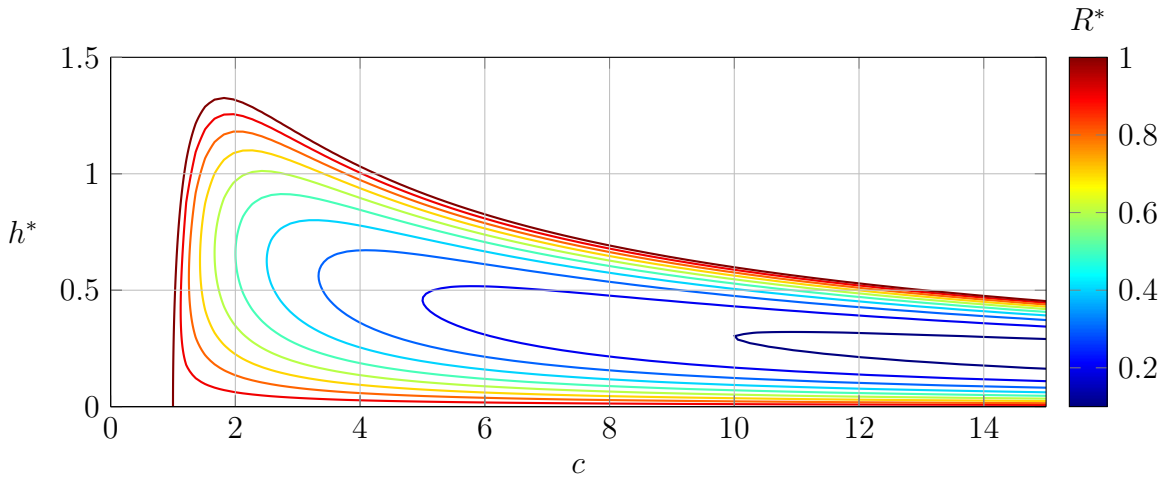


Figure 2.2: Each line represents a value of R^* such that (2.1.11) is satisfied. Using this, we can see the corresponding maximal value of h^* for the given R^*. This maximal h^* is the upper limit of catenoidal solutions of (2.1.11), for h^* greater than this value, only the Goldschmidt solution exists.

$$\begin{aligned} 0 &= \frac{\mathrm{d}}{\mathrm{d}c}\left(\frac{\cosh(ch^* - \cosh^{-1} c)}{c} - R^*\right), \\ &= \frac{\left(h^* - \frac{1}{\sqrt{c^2-1}}\right)\sinh(ch^* - \cosh^{-1} c)}{c} - \frac{\cosh(ch^* - \cosh^{-1} c)}{c^2}, \\ &= c\left(h^* - \frac{1}{\sqrt{c^2-1}}\right)\tanh(ch^* - \cosh^{-1} c) - 1. \end{aligned} \tag{2.1.12}$$

Given a choice of R^* satisfying $0 \leq R^* \leq 1$, (2.1.11) and (2.1.12) form a system of two equations for the two unknowns h^* and c, given as follows

$$\begin{cases} R^* = \dfrac{\cosh(ch^* - \cosh^{-1} c)}{c}, & (2.1.13) \\ 1 = c\left(h^* - \dfrac{1}{\sqrt{c^2-1}}\right)\tanh(ch^* - \cosh^{-1} c). & (2.1.14) \end{cases}$$

The solution of this system yields the limit of existence of a catenoidal solution to the axisymmetric minimal surface equation. For $R^* = 0$, the system (2.1.13)–(2.1.14) cannot be solved, as the range of the hyperbolic cosine does not contain zero. For $R^* = 1$, the solution $h^* \approx 1.32549$ is consistent with that found in the works of Goldschmidt [80], Goldstein et al. [71], Cryer and Steen [81], and Moulton et al. [64], among others. For $0 < R^* < 1$, the corresponding maximal values of h^*, visually represented in Figure 2.3, are consistent with the recent results found in the work of Salkin et al. [79].

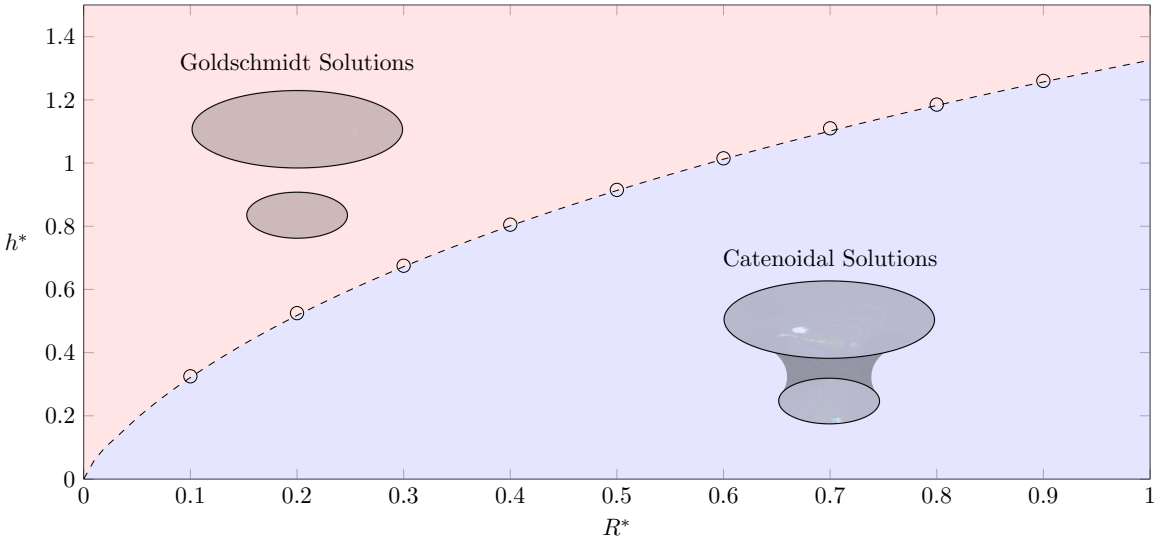


Figure 2.3: The dashed curve is the solution of the system given by (2.1.13) and (2.1.14). The system was numerically solved with Mathematica using the FindRoot method for $R^* \in [0, 1]$ with a resolution of 0.01. Empty circles correspond to Surface Evolver simulations for R^* in intervals of 0.1. The critical h^* value in the simulations is found by incrementing the separation distance between two bounding rings by 0.005 until a pinch-off is observed. The first value of h^* at which pinch-off is observed is plotted here. The red region represents combinations of R^* and h^* yielding Goldschmidt solutions, and in blue are pairs for which a catenoid solution exists. The inset images are simulation results for $R^* = 0.5$ and $h^* = 0.9$, 0.95 corresponding to catenoidal and Goldschmidt solutions.

2.1.2 Surface Evolver simulations

This thesis makes extensive use of Surface Evolver, a program developed by Brakke [77] in 1992 for numerical simulations of soap films and other applications in which surface energy is of paramount importance. Surface Evolver is a finite element-based energy minimization framework in which a surface is represented as a simplicial complex. Where a simplicial complex is defined as a surface that permits a triangulation made up of vertices, edges, and faces. The catenoid is a classical example used to demonstrate how the results vary and improve with simplex refinement and iteration. Figure 2.4 shows one possible simulation progression of a catenoid with $R^* = 0.5$ and $h^* = 0.9$; there, r denotes the number of refinements (namely, the number of times a given face has been subdivided), and g is the number of iterations taken toward converging to an energy minimum. Surface Evolver simulations are intrinsically non-dimensional; the (dimensionless) surface tension is set to unity by default. As such, the bounding ring in all subsequently discussed simulations has (dimensionless) radius unity.

Surface Evolver allows for topological changes, and so the condition of existence regarding catenoidal geometries as given by (2.1.13) and (2.1.14) can be verified numerically. Figure 2.3 shows the results of the simulations. The excellent accordance of the simulation results to predictions derived from the theoretical model indicates that the numerical scheme implemented with Surface Evolver is well suited to solve minimal surface problems of this general type.

In addition to the pinch-off criterion, which delimits the existence of catenoidal solutions, Surface Evolver can be used to calculate the normalized force due to surface

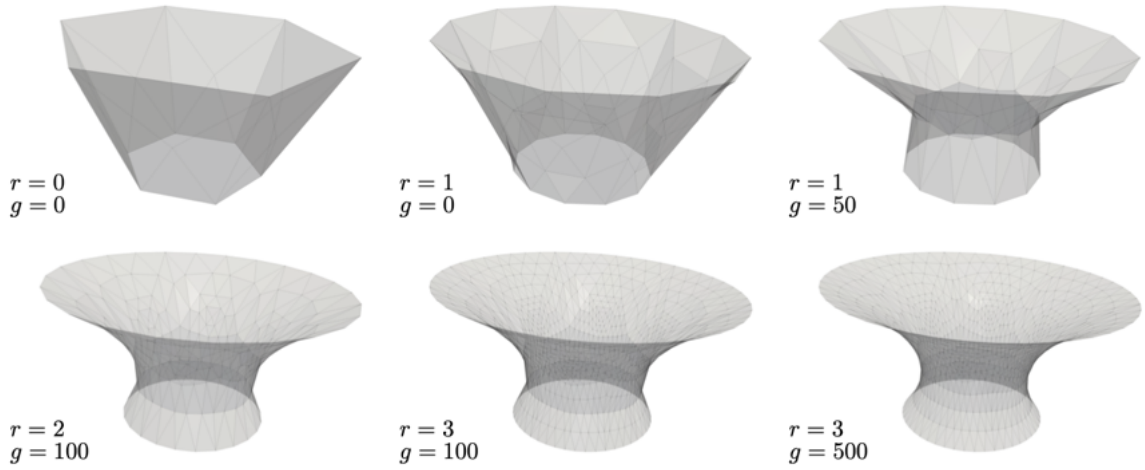


Figure 2.4: Examples of refinement (r) and iteration (g) operations within a Surface Evolver simulation of a catenoid where $R^* = 0.5$ and $h^* = 0.9$. The geometry shown here is the same as seen in the 3D representation of Figure 2.1.

tension acting on a boundary. The force due to surface tension is proportional to the length of the boundary. The remainder of this chapter focuses on the competition between the force due to gravity and the force due to surface tension. Determining the force due to surface tension is therefore of essential importance to the proceeding analysis. Consider the force acting on the lower ring as depicted in Figure 2.1. The force due to surface tension depends on the circumference of the ring and the angle at which the soap film meets the ring. Let ϕ denote the angle between the z-axis and the soap film where $z^* = h^*$. Thereby, the force due to surface tension acting in the z-direction is given by $F_\sigma = 4\pi R^* \sigma \cos\phi$. By the definition of ϕ, its tangent is given by $\tan\phi = \mathrm{d}r^*/\mathrm{d}z^*$ at $r^* = R^*$. The derivative of (2.1.9) with respect to z^* evaluated at $z^* = h^*$ yields

$$\frac{\mathrm{d}r^*}{\mathrm{d}z^*} = \tan\phi = \sinh(R_o\sqrt{C_1}h^* - \cosh^{-1} R_o\sqrt{C_1}). \tag{2.1.15}$$

As C_1 is, as of yet, undetermined, a corresponding equation relating C_1, R^*, and ϕ is found by use of an intermediate step of solving (2.1.3). Namely, (A.2.11) of Appendix A.2 evaluated for $r^* = R^*$ gives

$$\frac{\mathrm{d}r^*}{\mathrm{d}z^*} = \tan\phi = \sqrt{C_1 {R_i}^2 - 1}. \tag{2.1.16}$$

Isolating for C_1 is straightforward from (2.1.16), resulting in

$$R_o\sqrt{C_1} = \frac{R_0}{R_i\cos\phi} = \frac{1}{R^*\cos\phi}. \tag{2.1.17}$$

Using (2.1.17), (2.1.15) can be written as

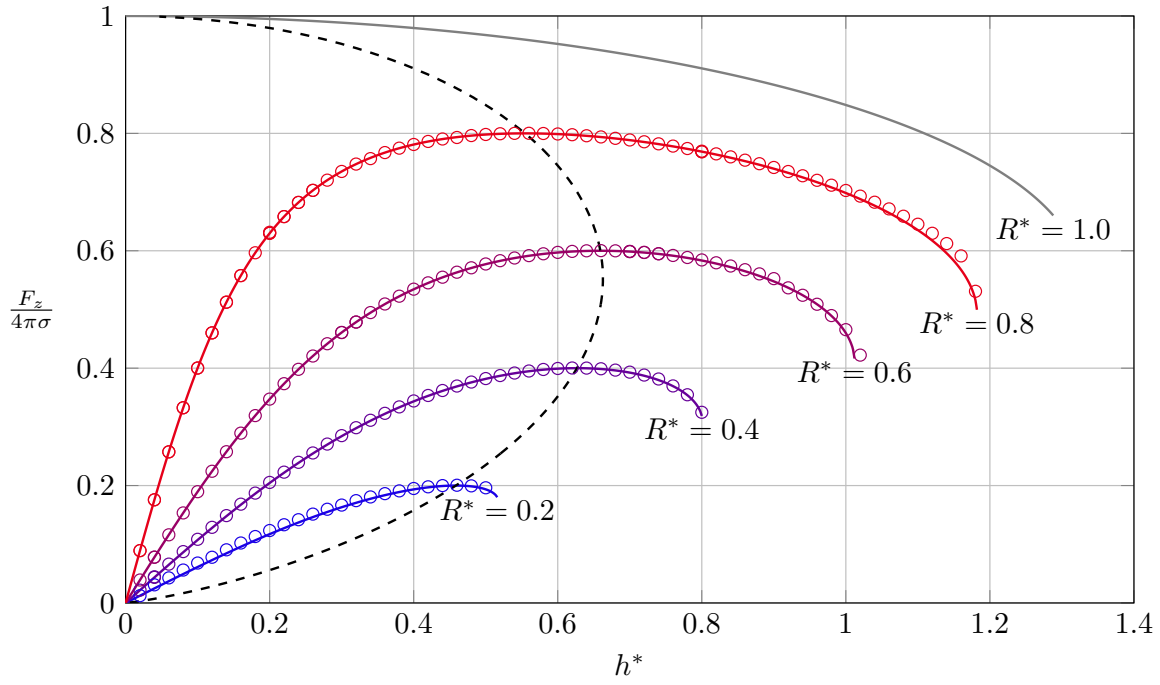


Figure 2.5: Theory and simulation results of the normalized force due to surface tension acting on the lower bounding ring of a catenoidal soap film with surface tension σ. Solid lines are found by solving (2.1.18) given R^* and h^* in the appropriate domains, while empty circles denote the simulation results obtained via Surface Evolver simulations. The corresponding radii are labeled, and the dashed line is the locus of points corresponding to the maxima obtained for each value of R^*, calculated by setting $\phi = 0$ in (2.1.18).

$$\sinh^{-1}(\tan\phi) = \frac{h^*}{R^*\cos\phi} + \cosh^{-1}\left(\frac{1}{R^*\cos\phi}\right). \tag{2.1.18}$$

Given values of R^* and h^*, (2.1.18) can be solved numerically. The curves in Figure 2.5 are found by fixing R^* and computing ϕ for each h^* using Mathematica. The points seen in Figure 2.5 are extracted from Surface Evolver using the `v_force()` method at each vertex where the soap film meets the ring of radius R^*. The force due to surface tension acting along the z-axis is normalized by the force, per unit length, $4\pi\sigma$, exerted by the soap film on the supporting ring of dimensionless radius unity.

2.2 Variational formulation of a suspended ring

The present section aims to establish a useful estimate for the load-carrying capacity of a soap film with given surface tension. This goal is achieved by studying a novel variant of the classical catenoidal soap film that is formulated next. Consider a soap film with surface tension σ that spans a rigid circular ring of radius R_o that is suspended from a circular ring fixed so that its axis of symmetry is parallel to the direction of the force due to gravity. Suppose that another rigid circular ring of mass m and radius $R_i < R_o$ is suspended in the film, and it shares the same axis of symmetry as the ring that supports the soap film, as shown in Figure 2.6.

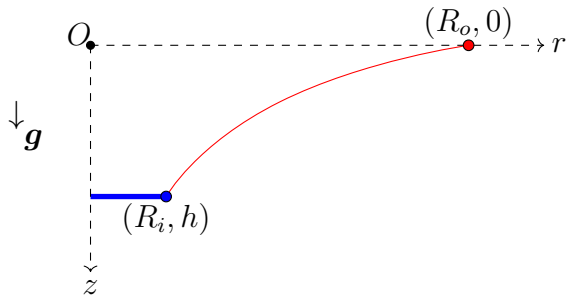


Figure 2.6: Schematic of the axisymmetric geometry in the (r, z) plane, $r = 0$ is the axis of rotation. The soap-film membrane is shown in red, while the suspended ring is blue. As h is allowed to vary, the suspended ring in blue is assumed to remain in the same orientation for multiple values of h.

The shape of the soap film in Figure 2.6 can be represented as a function R of the vertical coordinate that is defined such that, for a given separation h, $R(h) = R_i$. The coordinates are identically defined as in the previous section, but h in this context is unknown. The relaxation of the constraints on the system results in many fascinating outcomes.

In principle, the total energy of the system can be written as a sum of the surface energy of the soap film, the gravitational potential energy of the ring, and the gravitational potential energy of the soap film. However, the total mass of a typical soap film with thickness ranging from 50 nm to 500 nm suspended from a circular ring of radius 5 cm ranges from 0.3 mg to 3 mg[1]. This is between two and three orders of magnitude smaller than the mass of the suspended rings to be considered. On these grounds, the mass of the soap film is neglected in the subsequent calculations, and the total potential energy of the system is taken to be of the form

$$\begin{aligned}\mathcal{E}(R,h) &= \int_0^l 2\sigma(2\pi R)ds - mgh \\ &= \int_0^h \left[4\pi\sigma R\sqrt{1+(R')^2}\right] dz - mgh. \end{aligned} \tag{2.2.1}$$

The function R and the distance h between the supporting and suspending rings are unknown quantities. For the soap film to be in equilibrium, these quantities must satisfy the Euler–Lagrange equations of the functional. To derive those equations, variations $R+\epsilon\eta$ and $h+\epsilon k$ are considered for some parameter $\epsilon \ll 1$. Consistent with the Dirichlet boundary condition

$$R(0) = R_o, \tag{2.2.2}$$

and the variation η of R must satisfy

$$\eta(0) = 0. \tag{2.2.3}$$

[1]For a detailed investigation of the effects due to gravity on a soap film spanning a ring, please refer to Appendix A.1

A further restriction between the value $\eta(h)$ of the variation at the suspended ring and the variation k of the distance separating it from the supporting ring arises on recognizing that R must satisfy the Dirichlet condition

$$R(h) = R_i. \tag{2.2.4}$$

To derive that condition, consider the following expansion of R about $z = h$:

$$\begin{aligned} R(h) &= R(h + \epsilon k) + \epsilon\eta(h + \epsilon k) \\ &= (R(h) + \epsilon k R'(h) + \epsilon^2 k R''(h) + \cdots) + (\epsilon\eta(h) + \epsilon^2 k\eta'(h) + \cdots) \\ &= R(h) + \epsilon(kR'(h) + \eta(h)) + \mathcal{O}(\epsilon^2), \end{aligned} \tag{2.2.5}$$

where the correction term $\mathcal{O}(\epsilon^2)$ incorporates all contributions involving quadratic and higher powers of ϵ. By (2.2.5), $kR'(h) + \eta(h) = \mathcal{O}(\epsilon)$, from which it follows that the variations η and k must satisfy

$$\eta(h) = -kR'(h). \tag{2.2.6}$$

Apart from (2.2.3) and (2.2.6), the variations η and k can be selected arbitrarily.

Let $\mathcal{F}$ be defined by

$$\begin{aligned} \mathcal{F}(\epsilon) &= \mathcal{E}(R + \epsilon\eta, h + \epsilon k) \\ &= \int_0^{h+\epsilon k} \left[4\pi\sigma(R + \epsilon\eta)\sqrt{1 + (R' + \epsilon\eta')^2}\right] dz - mg(h + \epsilon k) \qquad (2.2.7) \\ &= \int_0^{h} \left[4\pi\sigma(R + \epsilon\eta)\sqrt{1 + (R' + \epsilon\eta')^2}\right] dz \\ &\quad + \int_h^{h+\epsilon k} \left[4\pi\sigma(R + \epsilon\eta)\sqrt{1 + (R' + \epsilon\eta')^2}\right] dz - mg(h + \epsilon k). \qquad (2.2.8) \end{aligned}$$

Granted that R and h correspond to a minimum of the potential energy functional defined in (2.2.1), the Gateaux derivative of $\mathcal{F}$ must vanish at $\epsilon = 0$:

$$\left.\frac{\mathrm{d}\mathcal{F}(\epsilon)}{\mathrm{d}\epsilon}\right|_{\epsilon=0} = 0. \tag{2.2.9}$$

Computing the derivative of (2.2.8) with respect to ϵ gives

$$\begin{aligned} \frac{\mathrm{d}\mathcal{F}(\epsilon)}{\mathrm{d}\epsilon} &= \int_0^h \left[4\pi\sigma\eta\sqrt{1 + (R' + \epsilon\eta')^2} + 4\pi\sigma(r + \epsilon\eta)\frac{\eta'(R' + \epsilon\eta')}{\sqrt{1 + (R' + \epsilon\eta')^2}}\right] dz \\ &\quad + k\left[4\pi\sigma(R(h) + \epsilon\eta(h))\sqrt{1 + (R'(h) + \epsilon\eta'(h))^2}\right] \\ &\quad + \int_h^{h+\epsilon k} \left[4\pi\sigma\eta\sqrt{1 + (R' + \epsilon\eta')^2} + 4\pi\sigma(R + \epsilon\eta)\frac{\eta'(R' + \epsilon\eta')}{\sqrt{1 + (R' + \epsilon\eta')^2}}\right] dz - mgk, \end{aligned} \tag{2.2.10}$$

from which it follows that

$$\left.\frac{\mathrm{d}\mathcal{F}(\epsilon)}{\mathrm{d}\epsilon}\right|_{\epsilon=0} = \int_0^h 4\pi\sigma \left[\eta\sqrt{1+(R')^2} + \frac{RR'\eta'}{\sqrt{1+(R')^2}}\right] dz + k\left[4\pi\sigma R(h)\sqrt{1+(R'(h))^2} - mg\right] \tag{2.2.11}$$

Applying integration by parts to the second term of the integral on the right-hand side of (2.2.11) and using the Dirichlet condition (2.2.4) and the constraint (2.2.6) on the variations η and k yields

$$\begin{aligned}\left.\frac{\mathrm{d}\mathcal{F}(\epsilon)}{\mathrm{d}\epsilon}\right|_{\epsilon=0} = \int_0^h 4\pi\sigma\eta \left[\sqrt{1+(R')^2} - \frac{\mathrm{d}}{\mathrm{d}z}\left(\frac{RR'}{\sqrt{1+(R')^2}}\right)\right] dz \\ + k\left[4\pi\sigma R_i\sqrt{1+(R'(h))^2} - mg - \frac{4\pi\sigma R_i(R'(h))^2}{\sqrt{1+(R'(h))^2}}\right].\end{aligned} \tag{2.2.12}$$

Using (2.2.12) in the stationarity condition (2.2.9) and invoking the Dirichlet condition (2.2.4) delivers the first-variation condition for the energy functional (2.2.1) in the form

$$\begin{aligned}0 = \int_0^h 4\pi\sigma\eta \left[\sqrt{1+(R')^2} - \frac{\mathrm{d}}{\mathrm{d}z}\left(\frac{RR'}{\sqrt{1+(R')^2}}\right)\right] dz \\ + k\left[4\pi\sigma R_i\sqrt{1+(R'(h))^2} - mg - \frac{4\pi\sigma R_i(R'(h))^2}{\sqrt{1+(R'(h))^2}}\right].\end{aligned} \tag{2.2.13}$$

2.2.1 Boundary value problem

First, if η is compactly supported about an arbitrary point interior to the interval $(0, h)$ and $k = 0$, (2.2.13) yields the ordinary differential equation

$$0 = \sqrt{1+(R')^2} - \frac{\mathrm{d}}{\mathrm{d}z}\left(\frac{RR'}{\sqrt{1+(R')^2}}\right). \tag{2.2.14}$$

In view of (2.2.14), the first-variation condition (2.2.13) reduces to the requirement that

$$0 = k\left[4\pi\sigma R_i\sqrt{1+(R'(h))^2} - mg - \frac{4\pi\sigma R_i(R'(h))^2}{\sqrt{1+(R'(h))^2}}\right] \tag{2.2.15}$$

hold for all admissible choices of k, from which it follows that

$$\begin{aligned}\frac{mg}{4\pi\sigma R_i} &= \sqrt{1+(R'(h))^2} - \frac{(R'(h))^2}{\sqrt{1+(R'(h))^2}} \\ &= \frac{1}{\sqrt{1+(R'(h))^2}}.\end{aligned} \tag{2.2.16}$$

Together, the equilibrium conditions (2.2.14)–(2.2.16) comprise a boundary value problem for R involving mixed boundary conditions. Namely, an inhomogeneous Dirichlet condition at the fixed bounding ring and a Neumann condition corresponding to the suspended ring.

$$\begin{cases} 0 = \sqrt{1+(R'(z))^2} - \dfrac{\mathrm{d}}{\mathrm{d}z}\left(\dfrac{R(z)R'(z)}{\sqrt{1+(R'(z))^2}}\right), & 0<z<h, \quad (2.2.17) \\ R(0) = R_o, & (2.2.18) \\ (R'(h))^2 = \left(\dfrac{4\pi\sigma R_i}{mg}\right)^2 - 1. & (2.2.19) \end{cases}$$

2.2.2 Closed form solution

The ordinary differential equation (2.2.17) is the axisymmetric minimal surface equation. As shown in the previous section and Appendix A.2, the solution to that equation is

$$R(z) = \frac{\cosh(\sqrt{C_1}(z+C_2))}{\sqrt{C_1}}. \quad (2.2.20)$$

The constants of integration C_1 and C_2 that enter (2.2.20) are to be determined by ensuring that (2.2.20) satisfies the boundary conditions (2.2.18) and (2.2.19). Applying (2.2.18) to (2.2.20) yields C_2 in terms of R_o and C_1:

$$C_2 = \frac{\cosh^{-1}(R_o\sqrt{C_1})}{\sqrt{C_1}}. \quad (2.2.21)$$

Next, applying (2.2.19) to the consequence

$$C_1 = \frac{1+(R'(z))^2}{R_i^2} \quad (2.2.22)$$

of (2.2.20) determines C_1 as

$$C_1 = \frac{1+R'(h)^2}{R_i^2} = \left(\frac{4\pi\sigma}{mg}\right)^2. \quad (2.2.23)$$

Thus, using (2.2.21) and (2.2.23) in (2.2.20) determines R in the form

$$R(z) = \frac{mg}{4\pi\sigma}\cosh\left(\frac{4\pi\sigma z}{mg} + \cosh^{-1}\left(\frac{4\pi\sigma R_o}{mg}\right)\right), \qquad 0 \le z \le h. \quad (2.2.24)$$

Finally, evaluating (2.2.24) at (R_i, h) and solving for h yields a closed-form expression for the distance h between the supporting and suspending rings:

$$h = \frac{mg}{4\pi\sigma}\left[\cosh^{-1}\left(\frac{4\pi\sigma R_i}{mg}\right) - \cosh^{-1}\left(\frac{4\pi\sigma R_o}{mg}\right)\right]. \quad (2.2.25)$$

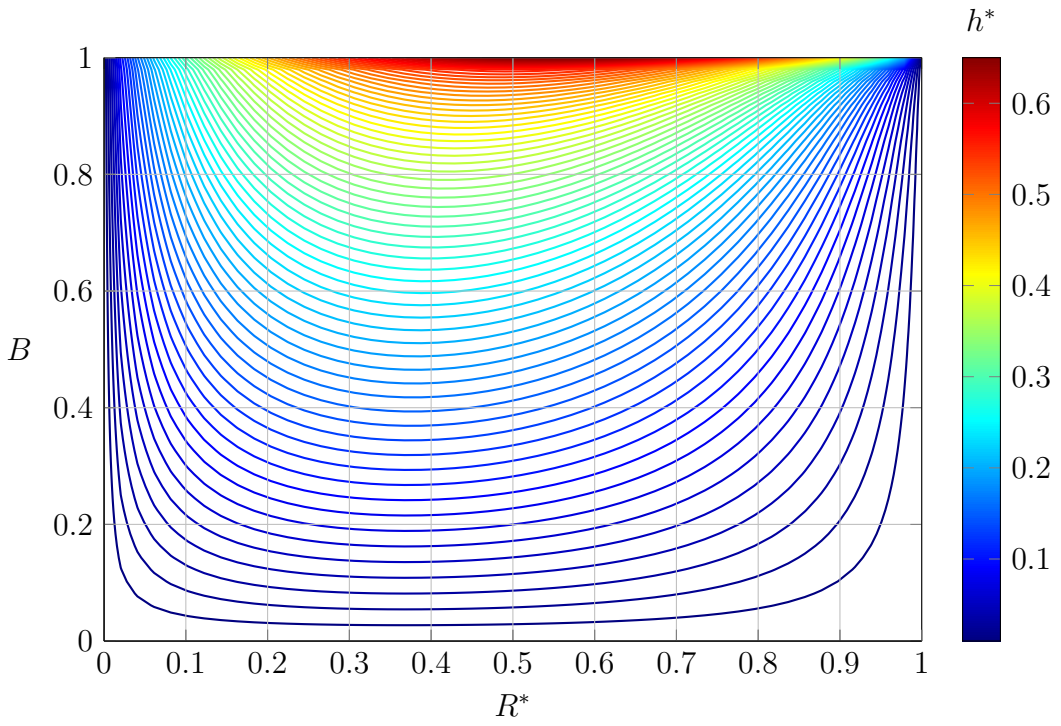


Figure 2.7: Phase space plot of (2.2.27) in the (R^*, B) plane, with the color representing h^*. Each line represents a combination of B and R^* values such that h^* is constant.

The dimensionless parameter

$$B = \frac{mg}{4\pi\sigma R_i}, \tag{2.2.26}$$

can be identified as the Bond number of the system. Defining $h^* = h/R_o$ and $R^* = R_i/R_o$ as in the treatment of the classical problem for a catenoid. Then, by (2.2.25) and (2.2.26),

$$h^* = BR^* \left(\cosh^{-1} \frac{1}{B} - \cosh^{-1} \frac{1}{BR^*} \right). \tag{2.2.27}$$

A contour plot of curves corresponding to constant values of h^* in the (R^*, B)-plane is presented in Figure 2.7. Notice from (2.2.27) that a condition on the existence of solutions is

$$B \leq 1; \tag{2.2.28}$$

this solvability condition is identical to the requirement that the value of $R'(h)$ found from (2.2.19) be a real number. This is a natural outcome as the condition that $mg \leq 4\pi\sigma R_i$ results from force balance at equilibrium along the edge of the suspended ring.[2] The Bond number found in the work of Davies and Raufaste [58] is defined as $Bo = \rho g r_s^2/2\sigma$. Since the suspended geometry in Figure 2.6 is circular, $m/2\pi R_i$ can be recognized as the mass density of the suspended ring. The bound of $Bo < 1$ seen in the work of Davies and Raufaste [58] is similarly found here. For a given fixed value of R^*, as B increases (for example, by increasing the mass density m of the suspended right), the distance h^* between the supporting and suspended rings increases. In Figure 2.8,

[2] For a detailed derivation of (2.2.27) using the principle of force balance, see to Appendix A.3.

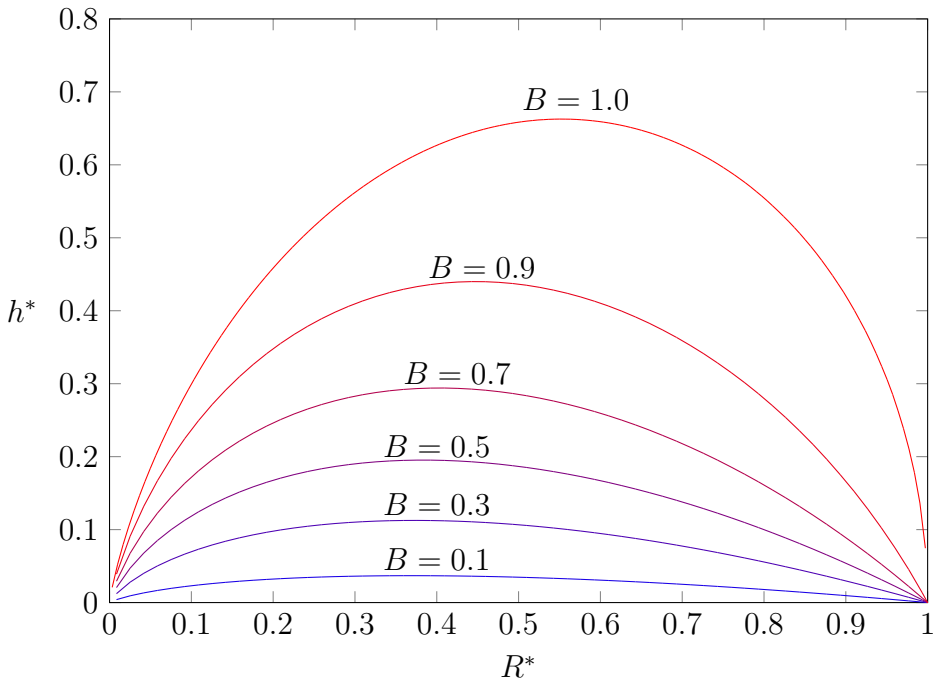


Figure 2.8: Sections of contour plot in Figure 2.7 given constant values of B.

for a fixed value of B note that there exists a value of R^* such that the value of h^* is maximal. This corresponds to varying the radius R_o of the supporting ring while fixing all other relevant parameters.

Further analysis of (2.2.27) affords a characterization of the local maxima of the curves seen in Figure 2.8. Consider the consequence of setting the derivative of (2.2.27) with respect to R^* equal to zero, given by

$$\begin{aligned} 0 &= \frac{\mathrm{d}}{\mathrm{d}R^*}\left[BR^*\left(\cosh^{-1}\left(\frac{1}{B}\right) - \cosh^{-1}\left(\frac{1}{BR^*}\right)\right) - h^*\right], \\ &= B\cosh^{-1}\left(\frac{1}{B}\right) - B\cosh^{-1}\left(\frac{1}{BR^*}\right) + \frac{B}{\sqrt{1-(R^*)^2}}. \end{aligned} \tag{2.2.29}$$

For $B = 1$, (2.2.29) can be evaluated numerically to show that the red curve shown in Figure 2.8 has a maximum at $R^* \approx 0.55$, and that the corresponding value of h^* is approximately 0.66. These values are depicted in Figure 2.9.

Figure 2.10 presents the alternative sections of (2.2.27), exhibiting how h^* varies with B for fixed values of R^*. Compared to the analogous curves in Figure 2.8, the curves of constant R^* in Figure 2.10 increase monotonically for $0 \leq B \leq 1$, with the consequence that the maximum of each curve is thus found at $B = 1$. Additionally, evaluating (2.2.27) at $B = 1$ yields the same equation governing R^* and h^* as evaluating (2.1.18) for $\phi = 0$. The limiting value $B = 1$ of the Bond number corresponds to the maximal carrying capacity of the system under consideration. It is equivalent to the maximal force due to surface tension acting on the suspended ring in a catenoidal soap film geometry.

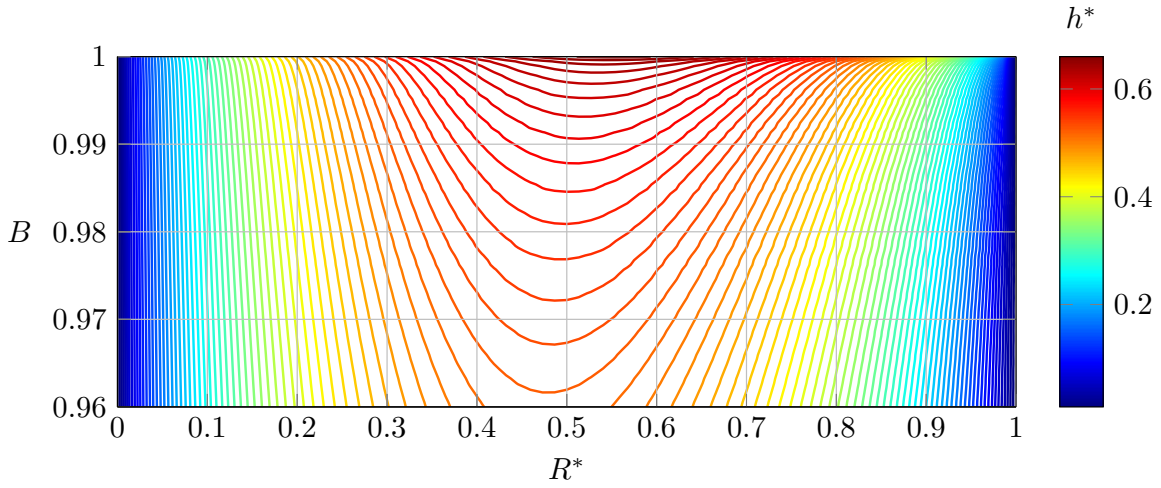


Figure 2.9: Limiting behavior of (2.2.27) as B approaches one. A closer look at the top of the contour plot see in Figure 2.7.

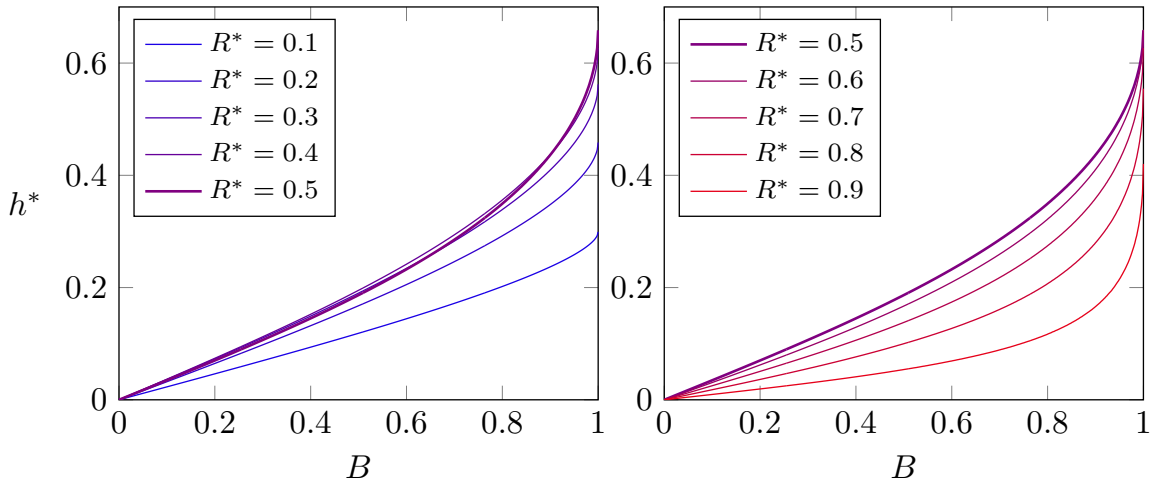


Figure 2.10: Sections of the contour plot in Figure 2.7 given constant values of R^*. Note that both subplots are on the identical domain, but due to the symmetry of (2.2.27) with respect to R^* the corresponding curves are seen to intersect.

2.3 Soap film experiments

2.3.1 Experimental setup and procedure

The experimental setup is depicted in Figure 2.11. It consists of the following components:

- An optical breadboard to align all supporting pillars.
- A 3D printed circular frame upon which the soap film is initially generated.
- A light source is located below the circular frame and inclined at a slight angle to allow imaging of the suspended rings in the soap film and the edge of the soap film.

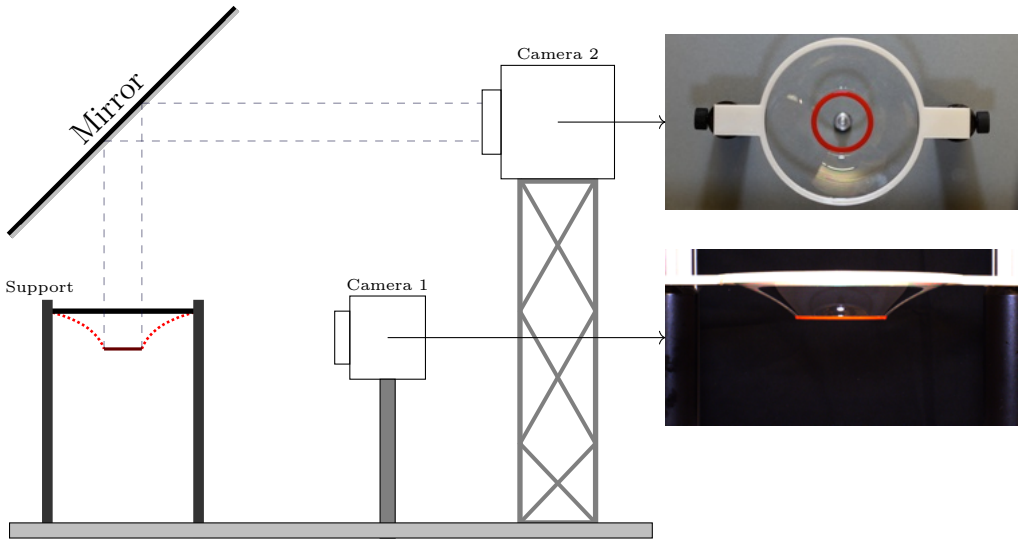


Figure 2.11: Experimental setup of soap film mediated self-assembly. Two pillars fix the support ring on either side attached to an optical breadboard plate. Two cameras are used for the side and top views, an iDS microscope camera with a 20 mm focal length lens and a Canon EOS 5Ds R DSLR with a 65 mm focal length lens, respectively. Corresponding images are seen on the right. A surface mirror angled at a 45-degree angle is used to enable top-down imaging. And a black curtain is placed behind the mirror and support pillars to facilitate the imaging using LED white light.

- A mounted camera aligned with the 3D printed circular frame.
- A surface mirror ensures clear images of the self-assembled structures from above.

The soap solution was made in identical fashion to that used by Biria & Fried [82], using 245 ml of distilled water, 45 ml of Glycerin, and 5 ml of Dawn® dishwashing liquid. Biria & Fried [82] measured the surface tension of the soap film to be 24 ± 0.1 mN/m and this value was used in all subsequent analyses. The experimental procedure begins by removing the supporting circular ring from the stand, submerging the ring in the soap solution, and removing the ring from the soap solution to generate the soap film. The supporting circular ring is then placed back on the stand, which has already been calibrated to ensure the soap film is perpendicular to the force due to gravity. The design of the supporting frame shown in Figure 2.12 was done using Autodesk Fusion. The previously mentioned calibration step can also be verified after deposition, namely after pre-wetting a ring or tile, as shown in Figure 2.11, where the alignment of the suspended tile can be seen from the top view.

The deposition of an object, such as a ring or tile, onto the soap film, must be done slowly and by ensuring that the object is nearly parallel to the supporting ring before releasing it. This ensures the soap film stabilizes as soon as possible, reducing transient phenomena and their effects. The faster the deposition of a ring or tile onto the membrane, the greater the kinetic energy of the system and, thereby, the greater the likelihood of film rupture or of the ring or tile passing through the film, as investigated by Stogin et al. [19].

The use of precision instrumentation for the deposition of rings or tiles is not necessary due to the robustness of the experimental procedure described herein. The

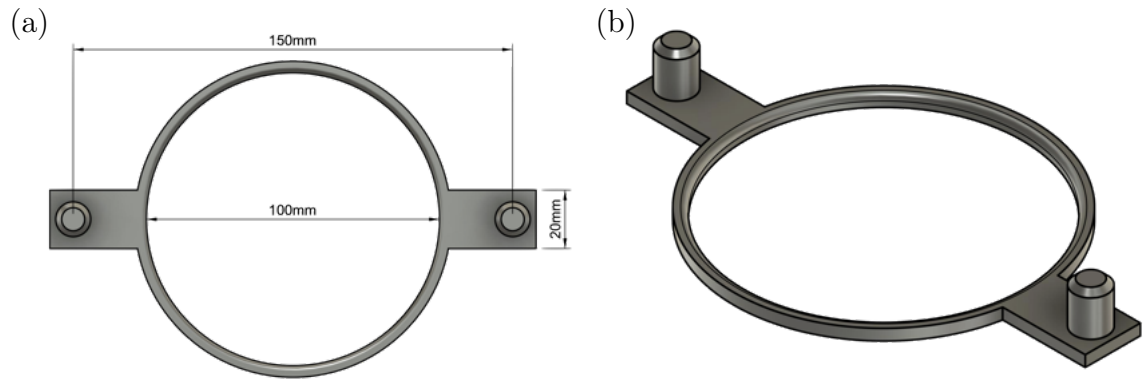


Figure 2.12: Using an Ultimaker S5 3D printer equipped with a 0.25 mm nozzle attachment and Tough PLA plastic as a material, the design shown was realized to directly connect with optical stand equipment in the lab. The interior radius of the ring is rounded to ensure that the pinning of the contact line is kept to a minimum.

equilibrium configuration of a soap film with a suspended ring or tile was observed to be independent of the horizontal position of that ring or tile when deposited on the soap film. Soap films were generally observed to equilibrate within one minute after the deposition of a tile up to 1 cm.

The ability to directly integrate the experimental setup into the existing optical equipment in the laboratory was integral to the consistency and simplicity of the experimental procedure. The design of the supporting circular frame seen in Figure 2.12 in particular underwent multiple design iterations. Taking into account the size of the soap solution container, ease of film generation, and ease of calibration resulted in the design seen in Figure 2.12.

2.3.2 Experimental results for suspended rings

As shown in Figure 2.8, the variation of h^* with respect to R^* for fixed values of the Bond number B is approximately quadratic. Additionally, for fixed values of R^* Figure 2.7 shows that h^* increases monotonically with B. To explore these behaviors experimentally, four choices of R^* were considered, namely $R^* = 0.2$, $R^* = 0.4$, $R^* = 0.6$, and $R^* = 0.8$, for varying values of B achieved by varying the total mass m of each ring. These choices of R^* correspond to $R_i = 1$ cm, $R_i = 2$ cm, $R_i = 3$ cm, and $R_i = 4$ cm since all experiments were conducted with a supporting ring a radius of 5 cm.

Each deposited ring was 3D printed from Polylactic Acid, commonly known as PLA, a type of recycled plastic commonly used in 3D printers. The material used has a mass density of 1.24 g/cm^3. For each choice of the dimensionless radius R^*, the mass of each deposited ring was varied by modifying the thickness and annular radius of the ring. The thickness of the rings is the height when laying on a flat surface, a result of the printing process used to construct them. The annular radius is the difference between the outer and inner radii of the ring. The resolution of the 3D printer allowed for consistent thicknesses of 0.5, 0.75, and 1 mm. Table 2.1 shows the mass of individual

rings given the corresponding physical characteristics.

	$R_i = 1$ cm		
	$\tau = 0.5$ mm	$\tau = 0.75$ mm	$\tau = 1.0$ mm
$A_r = 2$ mm	0.0654 g	0.0948 g	0.1357 g
$A_r = 4$ mm	0.1098 g	0.1672 g	0.2341 g
$A_r = 6$ mm	0.1430 g	0.2152 g	NA

	$R_i = 2$ cm		
	$\tau = 0.5$ mm	$\tau = 0.75$ mm	$\tau = 1.0$ mm
$A_r = 2$ mm	0.1920 g	0.2841 g	0.4057 g
$A_r = 4$ mm	0.2455 g	0.3725 g	0.5254 g
$A_r = 6$ mm	0.3103 g	0.4299 g	NA

	$R_i = 3$ cm		
	$\tau = 0.5$ mm	$\tau = 0.75$ mm	$\tau = 1.0$ mm
$A_r = 2$ mm	0.1916 g	0.2920 g	NA
$A_r = 4$ mm	0.3894 g	0.5673 g	NA
$A_r = 6$ mm	0.5757 g	0.8131 g	NA

	$R_i = 4$ cm		
	$\tau = 0.5$ mm	$\tau = 0.75$ mm	$\tau = 1.0$ mm
$A_r = 2$ mm	0.2724 g	0.3871 g	0.5727 g
$A_r = 4$ mm	0.5300 g	0.7538 g	0.8573 g
$A_r = 6$ mm	0.7753 g	NA	1.1249 g

Table 2.1: Individual mass of 3D printed rings used in the experimental verification of the proposed theory in Section 2.2.2. The annular radius A_r is the difference between the exterior, R_i, and the interior radius of a particular ring. As all rings were 3D printed, each ring has a height or thickness compared to the print surface; τ is this thickness of the ring with respect to the z-axis.

From (2.2.29) it is known that for values of R^* that are sufficiently close to 0.55, the distance h^* between the fixed and suspended rings is maximized as the Bond number B approaches unity. Under these experimental conditions, the axisymmetric assumptions of the model presented often fail as the system tends to prefer an equilibrium configuration in which the suspended ring is tilted relative to the fixed ring. Goldstein et al. [83] investigated the inherent instability of a gravity current within a catenoid with a secondary film at its narrowest point. The observed flow into the lower half of the catenoid was not found to be symmetric; as such, in their experiments, the induced net force acting on the lower ring would be non-zero. In the suspended ring system considered here, the asymmetry of the force balance on the lower ring leads to an instability; as the flow found in the soap film reaches the suspended ring, its effective mass is no longer evenly distributed along the boundary where the soap film meets the ring. Consequently, the equilibrium orientation of the ring is not parallel to the supporting ring. A sequence of three images provided in Figure 2.13 show how this instability proceeds over time.

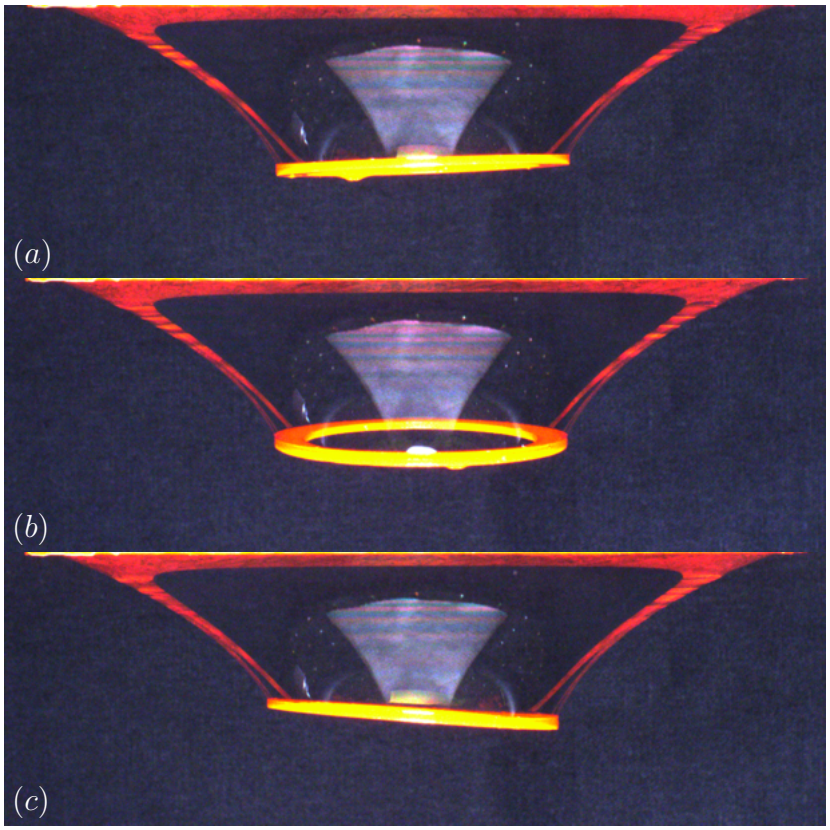


Figure 2.13: The instability of a suspended ring is shown, the radius of the ring is 2 cm, thickness of 1 mm, and mass is 0.406 g. Therefore the Bond number is $B = 0.66$ and $R^* = 0.4$. The instability leading to a rotation is hypothesized to be influenced by asymmetric gravity currents within the soap film, as shown by Goldstein et al. [83], air currents in the surrounding environment, and manufacturing defects. The time between images is approximately 2 s, but the rotation speed was noted to vary.

The suspended ring also rotates about its axis of symmetry during the instability described above. This is likely due to the asymmetry leading to the sloped orientation. A feedback loop of sorts can be hypothesized, whereby the gravity current leads to a slanted suspended ring that, in turn, changes the flow within the soap film. The rotation is not observed consistently; the rotation speed varies with environmental conditions and is even intermittent within the same experiment. The ambient airflow surrounding the soap film is likely to be a contributing factor along with potential manufacturing defects.

Figure 2.14 contains the experimental results of 31 distinct combinations of R^* and B. Extending the corresponding curves seen in Figure 2.10 to regions, the shaded areas bounded by the corresponding curves were done to account for errors stemming from the experimental setup. Error bars account for the potential change in the equilibrium value of h^* over five minutes. The flow induced in the soap film by both drainage and gravity currents affects the total mass concentrated on the suspended ring. In addition, the exact contact line of the soap film and the supporting frame cannot be directly measured; Alimov et al. [65, 69] recorded this as the major source of error in their soap film experiments. These two sources of error are accounted for in the shaded regions shown in Figure 2.14. The images in Figure 2.13 and Figure 2.14 present the soap film

as a red membrane; this is due to the color of the supporting frame and suspended ring. Diffuse white light was used to collect images from experiments; the internal reflection of light results in the distinctive color shown. Although the geometry differs from standard soap film experiments designed to explore drainage and thinning, Figure 2.13 and Figure 2.14 exhibit the characteristic bands of a thinning soap film. [51, 52, 84]

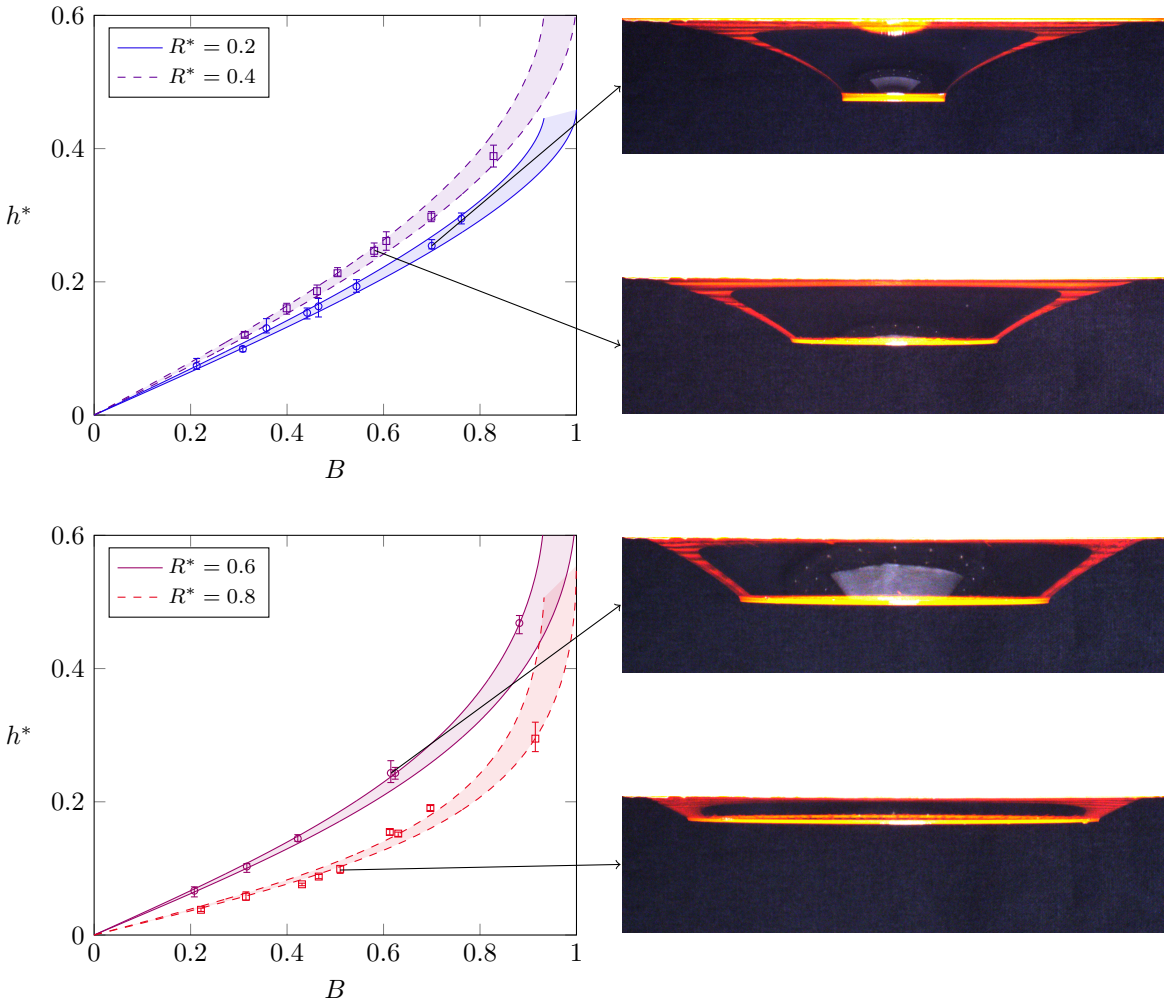


Figure 2.14: Experimental correspondence to the predictions seen in Figure 2.10. The regions seen are bounded below by the solution of (2.2.27) for each given value of R^* and above by an identical curve determined by a 7% increase in B to account for the mass of the soap film as well as other manufacturing errors. The error bars represent the maximal and minimal h^* measured over 5 minutes. The soap solution was made in an identical fashion to that used by Biria and Fried [82] with the surface tension determined to be 24 ± 0.1 mN/m. The rings on the right correspond to each of the test radii; the rings with radii of 2 and 4 cm have a thickness of 0.5 mm, the ring of radius 3 cm is 0.75 mm thick, and the ring of radius 1 cm is 1 mm thick.

2.3.3 Platonic solid assemblies

Building upon the experiments of rings suspended within a soap film, self-assembled structures formed by multiple tiles of various shapes are considered. The initial deposition of the tiles onto the soap film is carried out similarly to the procedure outlined in the previous section. To prevent the supporting soap film from rupturing on initial contact, each tile is first wetted with the same soap solution used to make the supporting soap film. Each tile should also intersect the soap film before release, and the release point should be as close to the center of the film as possible to minimize rotations and other instabilities. After the deposition of the first tile, the subsequent tiles should be released in a similar fashion close to the already freely dispersed tiles. Figure 2.15 provides a detailed visualization of the process of depositing square tiles in three colors to better illustrate the alignment and deposition process.

Following the release of the third tile, after Figure 2.15(c), the three squares snap into place and align into a cubic geometry as seen in Figure 2.16. This cubic structure is assembled without external influence.

The Bond number B defined in (2.2.26) is relevant as it allows the prediction of the maximum mass that can be supported. If the circumradius of the projected hexagon shown in the left-hand column of Figure 2.16 is approximately 1.6 cm. Setting $R_i \approx 1.6$ cm and solving for $B = 1$, given that $\sigma = 0.024$ N/m, it is found that the maximum mass that can be supported by the soap film is 0.492 g. As the total mass of the three square tiles combined is 0.3618 g, the cubic assembly is expected to be supported. The deviation of the cubic geometry from the model stems from the fact that the boundary where the tiles meet the soap film is non-planar. A circle cannot easily approximate the skew-hexagonal boundary of that self-assembled structure; the model derived for axisymmetric geometries can be used to obtain a minimal value of R_i and, consequently, a minimum value of R^*. Using the value of R^* obtained and setting $B = 1$, the value of h^* can also be found. This can be verified by inspection from Figure 2.9, from which it is evident that for $B = 1$, there exist at most two values of R^* which yield identical values of h^*. The smaller of these two choices of R^* corresponds to what is depicted in Figure 2.16.

Figure 2.17 shows five Platonic solid-like structures assembled using the gravity-mediated approach. The geometries seen comprise regular polygons; this minimizes the

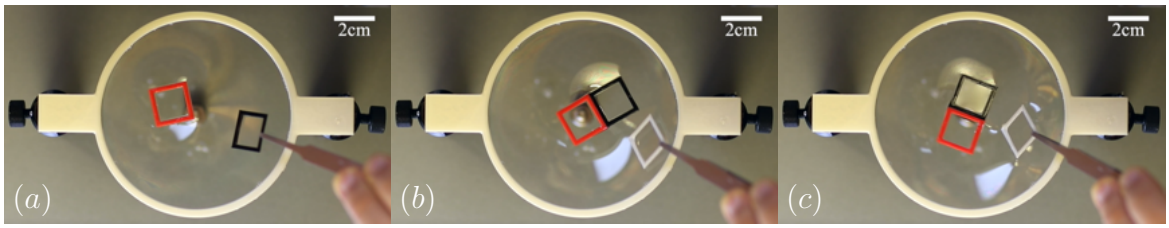


Figure 2.15: Deposition of square tiles onto a soap film. From left to right, (a) shows the instant prior to the deposition of the second tile, (b) the instant prior to the third tile coming into contact with the soap film, and (c) shows the third tile in contact with the soap film but still held in place by the tweezers. The alignment of the red and black tiles in (b) and (c) is what we refer to as edge-to-edge alignment. Please refer to Movie 1, or go to the URL: `https://www.dropbox.com/s/mvdacrnojahnwiv/Movie_1.mp4?dl=0` for a detailed view of the process.

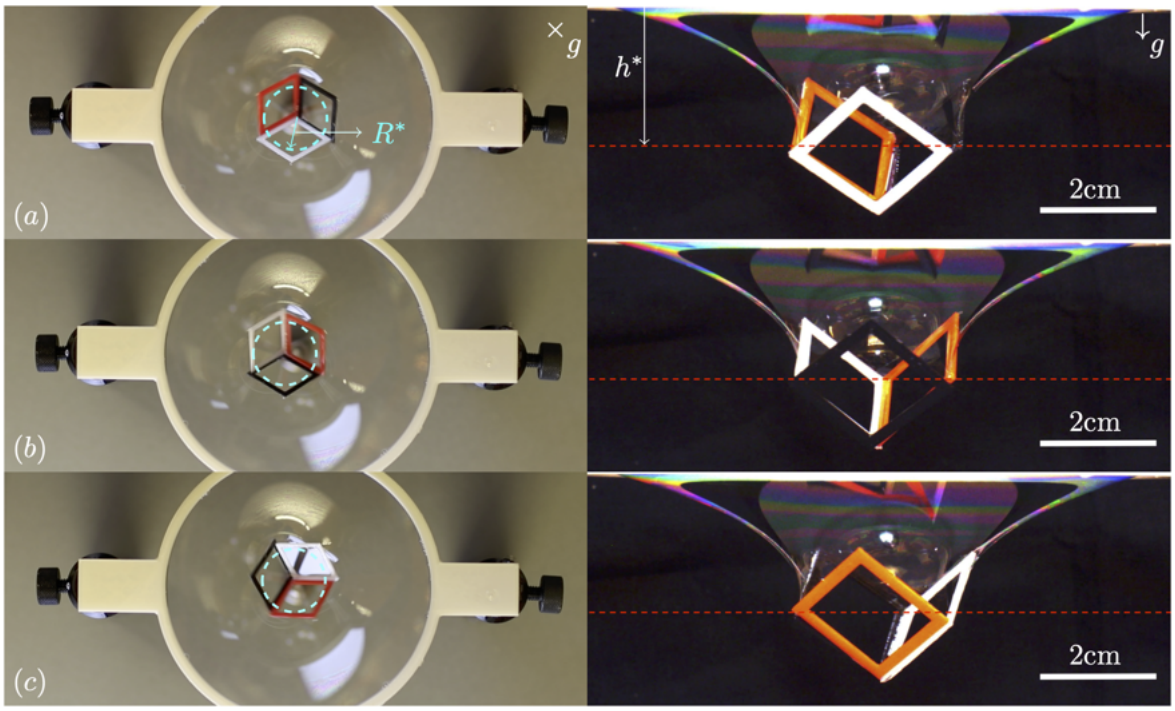


Figure 2.16: Detailed views of a suspended cubic geometry with white, black, and red squares of 2 cm side-length. While the suspended structures reach equilibrium with respect to the z-axis, the possible rotation of such structures due to environmental effects is observed here. Movie 1 shows the deposition and rotation seen here. The red dotted line corresponds to the solution of (2.2.27) given the mass of the supported structure ($m = 0.3618$ g). Generally, both B and R^* are necessary to find h^*, but assuming that $B = 1$, the value of R^* can be calculated given the other parameters. Solving $B = 1$ given the mass mentioned results in $R_i = 1.177$ cm, equivalently $R^* = 0.2354$ shown in the left column, which is smaller than the circumradius of the projected hexagon seen in the left-hand column. Setting $B = 1$ is equivalent to finding the minimal R^* that can support a given mass. And the h^* shown in the right column is the deflection corresponding to a ring of the given radius when $B = 1$.

potential misalignment of the tiles. While the assemblies are sensitive to the deposition of the tiles, the self-assembled structures are stable with respect to small perturbations. The average mass of the red triangles used in Figure 2.17 is 0.0581 g, meaning that the mass of the tetrahedral structure is 0.1743 g, that of the octahedral structure is 0.2324 g, and that of the icosahedron being 0.2905 g. The red squares used to assemble the cubic geometry have an average mass of 0.1191 g corresponding to a total mass of the assembly being 0.3573 cm. Lastly, the pentagons have an average mass of 0.1035 g, corresponding to a total mass of 0.3105 g for the dodecahedral assembly.



Figure 2.17: Simultaneous top and side views of self-assembled gravity-mediated structures. (a)-(e) each contains sections of tetrahedral, cubic, octahedral, icosahedral, and dodecahedral geometries. The triangular and square tiles have 2 cm edge lengths while the pentagonal tiles in (e) have edge length 1.5 cm. The empty interiors allow for more control of the mass suspended in the soap film as well as clearer images.

2.4 Surface Evolver simulations of non-axisymmetric geometries

It was noted that Surface Evolver could be used to compute the force that a soap film exerts on a solid boundary. In Section 2.1.2, the axisymmetry of the system allows for the construction of analytical solutions that can be used to confirm the accuracy of such computational results. For configurations such as those presented in Figure 2.16, the lower boundary of the soap film is non-planar; as such, a complete analytical representation of the system cannot be reduced to a one-dimensional problem. Therefore, numerical methods are necessary to determine the forces the soap film exerts on geometrically complex self-assembled structures. Surface Evolver is well adapted to that task.

Figure 2.18 shows the normalized force due to surface tension acting on a suspended structure with a cubic geometry for a range of values of the distance h^* between the supporting ring and the suspended structure. As with the Surface Evolver simulations for a suspended ring, Figure 2.5, the (dimensionless) radius of the supporting ring is set to unity in the simulations. The z-component of the force due to surface tension that is determined from the simulations is normalized by $4\pi\sigma$, which, due to the normalization, corresponds to the force that the soap film exerts on the supporting ring.

Figure 2.18 shows that Surface Evolver simulations can be used to predict not only the mass of a cubic assembly for a target value h^* but also the maximum mass of

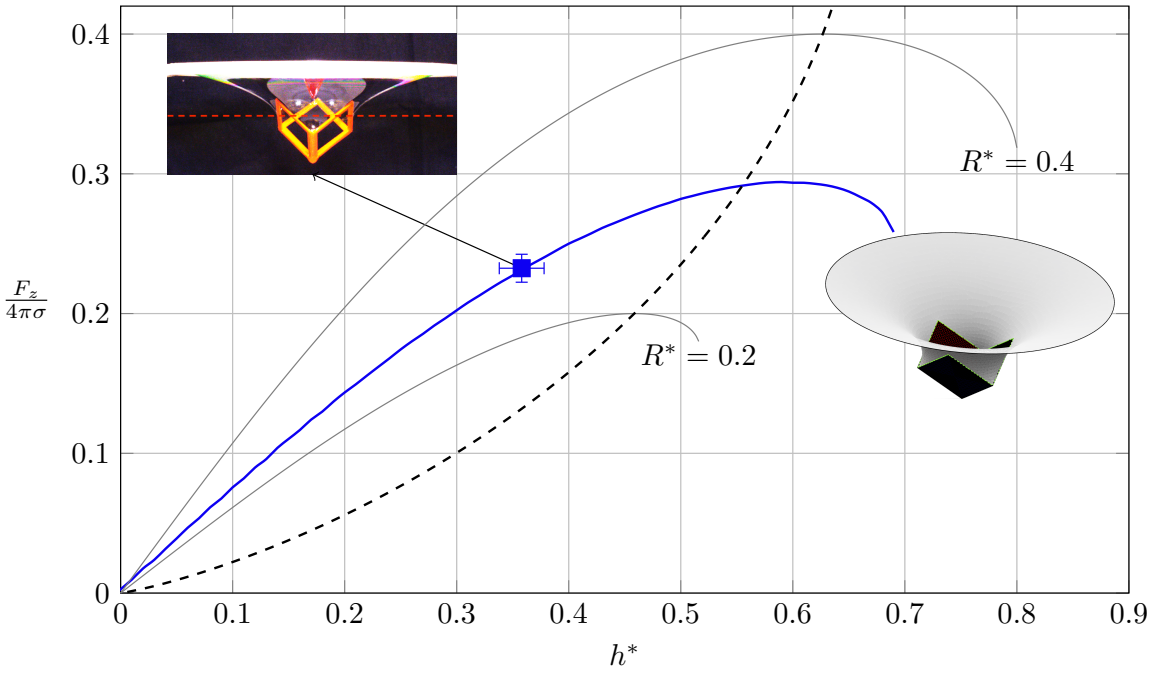


Figure 2.18: Simulation results of the normalized force due to surface tension acting on a cubic assembly. The curves corresponding to rings of radius $R^* = 0.2$, 0.4 are replicated from Figure 2.5 for reference, as is the dashed line. The inset image corresponds to the respective data point. The red dashed line in the inset image indicates the point from which h^* is measured. The square data point corresponds to the force due to gravity acting on the cubic assembly normalized in the same fashion.

a cubic assembly that can be supported by a soap film with surface tension σ. For the presented case of square tiles of side length 2 cm and a supporting ring of radius 5 cm, the maximum mass that a film with surface tension $\sigma = 0.024$ N/m can support is 0.452 g. Also noteworthy is that the curve corresponding to the simulations very closely resembles those presented in Figure 2.5. This implies that even for nonplanar soap film-structure boundaries, there exists an approximate radius for which the force due to surface tension is comparable to the simulation results, as the value of h^* varies. Additionally, the dashed line in Figure 2.18 intersects the blue curve close to its maximum. Section 2.1.2 details that the dashed curve corresponds to the maximal force due to surface tension that can be exerted on a ring of a given radius; this corresponds to solving (2.1.18) for $\phi = 0$. The dashed line is thereby the locus of local maxima of the curves seen in Figure 2.5 for all permissible values of R^*. Even for the cubic assembly simulations, this analytical prediction for the maximal force exerted by the soap film holds.

Figure 2.19 shows three additional simulations corresponding to tetrahedral, octahedral, and icosahedral gravity-mediated assemblies. Similar conclusions can be drawn regarding these assemblies, as shown for the cubic geometry. Notably, for the three structures depicted in Figure 2.19, the displacement h^* is more easily recognized in the experimental images as the boundary of the soap film, and the structure is confined to a plane. The boundaries where the soap film meets the tiles are given by an equilateral triangle, square, and pentagon for the tetrahedral, octahedral, and icosahedral structures, respectively. This observation facilitates the idea that an effective radius more easily approximates these structures as compared to the soap film boundary of the cubic assembly.

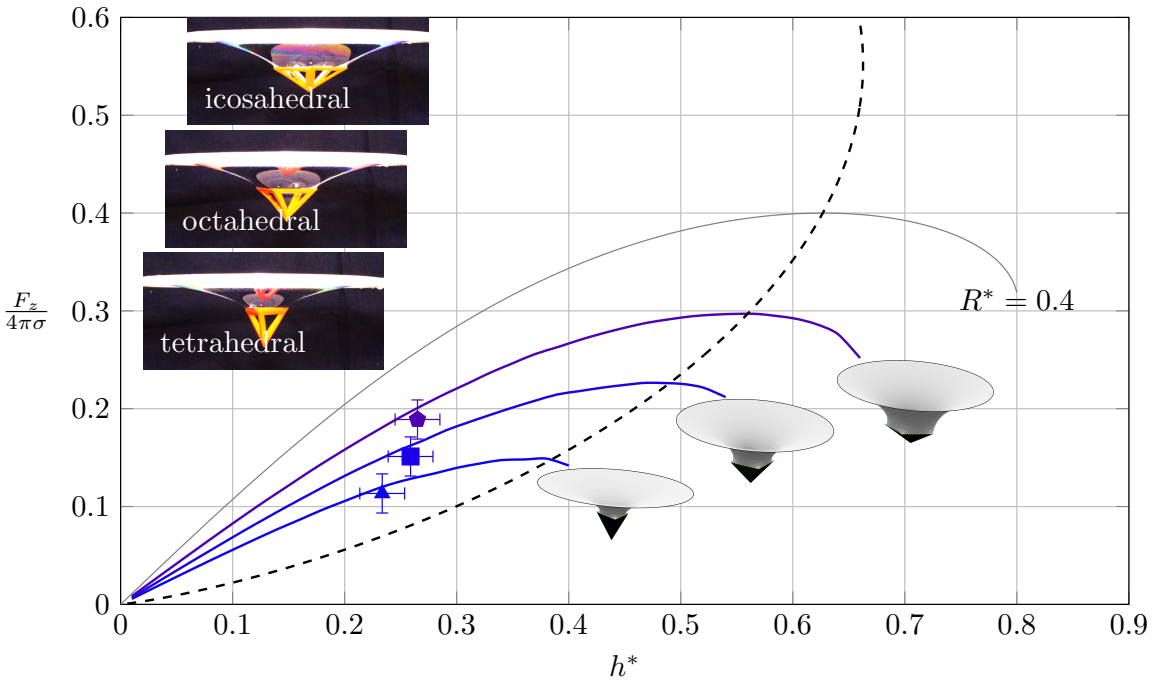


Figure 2.19: Simulation results of the normalized force due to surface tension acting on tetrahedral, octahedral, and icosahedral assemblies. The curve corresponding to a ring of radius $R^* = 0.4$ is replicated from Figure 2.5 for reference. Each inset image corresponds to the respective data point along the simulation curves. In contrast, the simulations seen at the termination points of the curves correspond to the displacement h^* for which the force due to surface tension is maximized. Note that the value of h^* for which the force due to surface tension is maximized approximately coincides with the dotted line (calculated by setting $\phi = 0$ in (2.1.18), or $B = 1$ in (2.2.27)).

Chapter 3

Displacement-driven self-assembly

The balance of surface forces and the force due to gravity can be seen as walking a tightrope. The more components are deposited onto the soap film, the total mass (B) increases, as does the effective radius (R^*); thereby, the possible assemblies are limited in size and complexity. For the construction of free-standing, detached assemblies, the system is constrained by introducing a base. Compared to the suspended ring idealization depicted in Figure 2.6, the separation distance h (and h^*) is now a parameter of the system. The basis of the assembly method presented in this chapter is predicated on the classical analysis of catenoidal soap films. Section 2.1 describes a pair of parallel axisymmetric rings where the smaller ring has a single degree of freedom in the z-axis; as the separation between the two rings increases, the shape of the soap film spanning the rings is continuously deformed up to the point at which a catenoid solution no longer exists. If the maximal separation distance between two rings for which a catenoidal solution exists is exceeded, the solutions found are known as Goldschmidt solutions [80]. Beyond the critical separation distance, the soap film spans each of the rings independently. As the separation of the two rings is increased to reach Goldschmidt solutions, a pinch-off phenomenon occurs. This topological transition has been well studied both experimentally and analytically. Applications range from vesicle permeability demonstrated by Frolov et al. [85], to foam formation as investigated by Chen et al. [59]. Combining the pinch-off phenomena with the alignment and self-assembly properties of a soap film demonstrated in Chapter 2, free-standing structures are realized through displacement-driven methods.

In Section 1 of this chapter, a brief description of the experimental setup is presented. A figure detailing the differences compared to the setup used in Chapter 2 is depicted, and an example of an assembled cubic structure is shown. The procedure of depositing the tiles is identical to that described in Section 2.3.

In Section 2, open prismatic structures are described. The realized structures are detailed as follows: 12 prism structures with triangular, square, pentagonal, and hexagonal bases were constructed with heights of 20 mm and 25 mm. A one-dimensional model based on the torque balance of an individual tile is presented and compared to experimental data. The experimental results of tile angles appear to demonstrate a transition, whereby for small base displacements d^*, the proposed theoretical model well approximates the experimental data, but as d^* increases, the angle of an individual tile can be approximated by a modified model corresponding to a masses tile. As this

transition is likely due to the interactions between tiles, numerical simulations using surface evolver are also carried out. The numerical simulations show excellent accordance with the experimental results for a range of Bond numbers. Once the tiles of a prismatic assembly align and are perpendicular to the base upon which they rest, an additional increment of the displacement, d^*, is observed prior to the initiation of soap film pinch-off. The pinch-off distances observed in the prismatic experiments compared to the theoretical predictions of catenoidal soap film existence limits from Section 2.1.1 are nearly identical when an effective radius of the prismatic structure is implemented. The proposed effective radius is further confirmed to be a robust prediction method by numerically verifying the behavior using Surface Evolver. Lastly, a discussion of assembly reversibility is presented and characterized.

In Section 3, pyramidal structures are discussed. Similar to the previous section, an effective radius is proposed and used to compare the experimentally observed pinch-off distances to the catenoidal model derived in Section 2.1.1. The discussion of assembly reversibility is expanded upon as the pyramidal structures exhibit more dynamic phenomena.

Section 4 provides a discussion of additional geometries assembled using the displacement-driven method. Closed prismatic structures with an additional tile on top are presented. Combinations of prismatic and pyramidal structures are shown, along with octahedral examples.

Lastly, Section 5 explores the possibility of self-folding as a subset of the displacement-driven assembly method presented in earlier sections. Two representative structures are shown: an open cube and an open octahedron. Square and triangular tiles with edge lengths of 2 cm were arranged into 2D nets of the corresponding structures, and adjacent edges are connected by the use of 35 μm thick tape on only one side to allow for the tape to act as a hinge. The nets are then pulled through a soap film generated on the same 5 cm radius ring. Two orientations are shown, where the structures are pulled upwards in the opposite direction compared to the force due to gravity and perpendicularly to the force due to gravity. These experiments provide multiple potential avenues for future work as the self-folded structures can be folded independently of the gravitational acceleration and the possibility for more intricate geometries is realized.

3.1 Experimental setup

To construct free-standing structures, as seen in Figure 3.1, a pre-wetted base is raised until it is coplanar to the supporting ring. The designs of the bases are depicted in Figure 3.2 by use of the computer-aided design (CAD) software Autodesk Fusion. The following step in the procedure is that the base is slightly lowered such that the cross-section of the soap film is a catenary-like curve. Then, the pre-wetted 3D printed tiles are deposited onto the membrane by hand. Lastly, the base is lowered until the soap film membrane pinches off into two disjoint parts. The supporting structures, cameras, and their arrangement are identical to those described in Section 2.3.

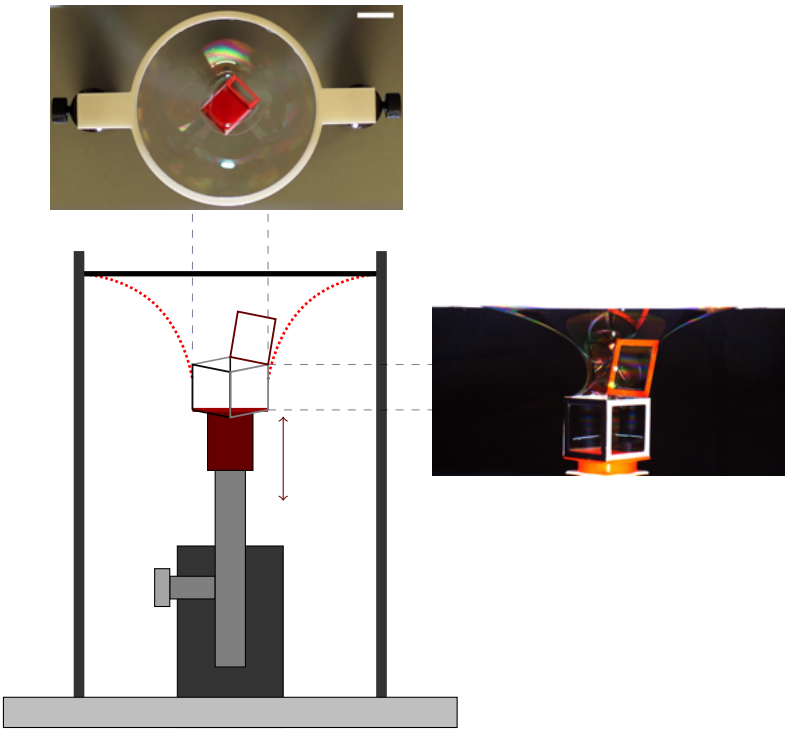


Figure 3.1: Experimental setup for displacement driven assemblies. A potential soap film configuration during an experiment is shown. The soap film is represented by the dotted red curves and the assembly by the solid black, grey, and dark red lines. The camera hardware and alignment are identical to those used in Section 3 of Chapter 2. The addition of a base is the only difference in the experimental setup. The 3D printed bases are directly coupled to a shaft with an M6 screw at the top. The shaft fits within a manual linear actuator that allows the shaft to slide up and down smoothly. There is also a screw lock within the actuator so that the shaft can be fixed in place while images are being recorded. The posts and linear actuator are attached directly to the optical breadboard below to ensure the base is centered with the ring supporting the soap film.

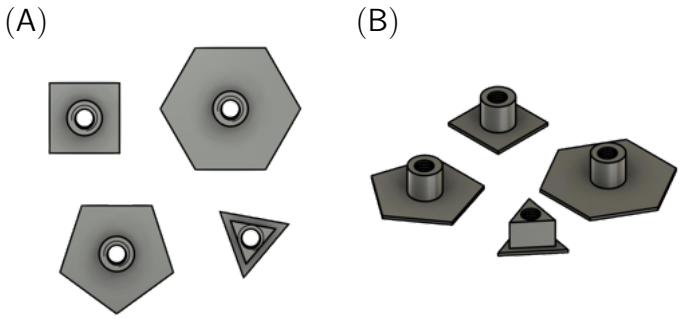


Figure 3.2: Using an Ultimaker S5 3D printer equipped with a 0.25mm nozzle attachment and Tough PLA plastic as a material, the base designs shown were made to directly connect with optical stand equipment in the lab. Edge lengths of 20 and 25 mm were made, and the inner hole is threaded to match the M6 screws typical of optical equipment. (A) and (B) show top and orthographic views, respectively.

3.2 Open prismatic structures

The first type of assembled structures detailed in this chapter are prismatic, built atop a base, enclosing the space above the corresponding polygonal base. Figure 3.3 shows four such assemblies with varying base geometry. Similarly to building a house, first, the walls must be raised. Figure 3.3 shows the initial configuration, followed by the process of bringing the tiles together. Figure 3.12 contains four examples of the final constructions from the corresponding initial states. Figure 3.12 shows a soap film spanning the tiles following the process depicted in Figure 3.3. As a catenoidal soap film pinches off, two disjoint films result. The pinch-off process of a catenoidal soap film has been investigated by Chen and Steen [86] numerically in 1997 and more recently by Goldstein et al. [71] analytically in 2021. In the context of displacement-driven assemblies, the pinch-off of the soap film results in one film returning to span the supporting ring while the other is trapped by the tiles making up the assembled structure.

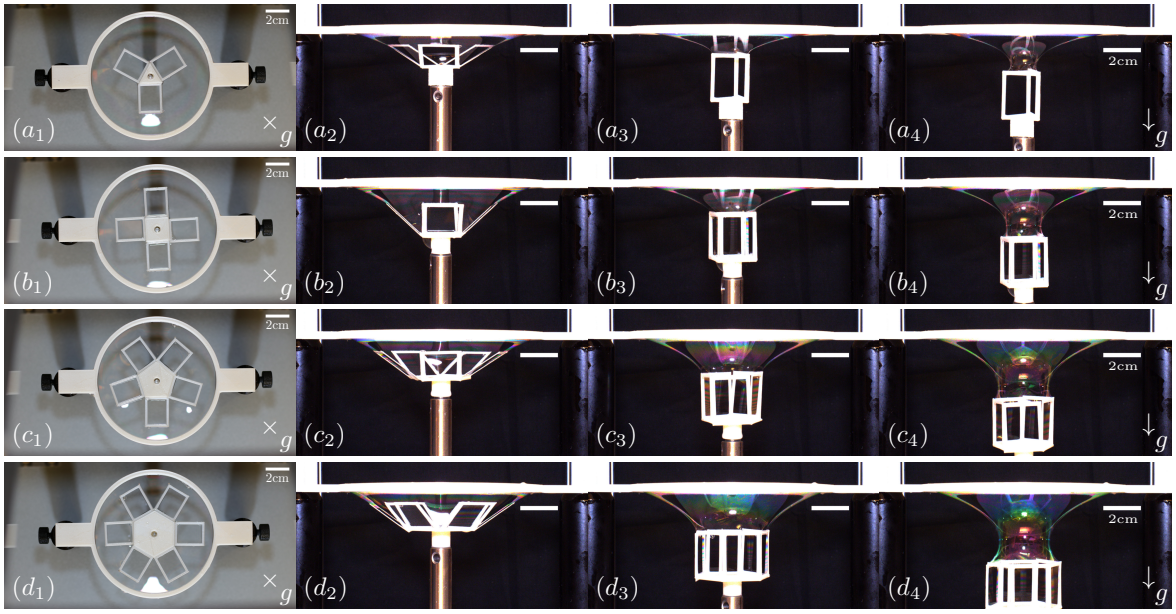


Figure 3.3: Self-assembly of prismatic structures with triangular, square, pentagonal, and hexagonal bases of 20 mm side width. The rectangular faces are of 25 mm height. Column (a_1)–(d_1) is a top view of the components' initial arrangements prior to the base displacement initiation. From columns 2 to 3, the lower bounding curve of the soap film exhibits a qualitative change as the components snap together. Column (a_4)–(d_4) shows the catenoid-like shape of the soap film immediately prior to the onset of instability. Small imperfections occur as tiles' initial deposition can lead to misalignment in the final construction. The final construction is stable for small deviations unless the misalignment is on the order of multiple millimeters. The snapping phenomena seen in column (a_3)–(d_3) may lead to collapse. Appendix B contains additional images of prismatic assemblies.

3.2.1 Transient tile angle prior to prismatic assembly

Considering the equilibrium position of the rectangular tiles seen in column 2 of Figure 3.3, there exists a range of base displacements for which the angle of an individual tile varies continuously with the imposed displacement until reaching $\pi/2$, as seen in column 3 of the same figure. In this section, a one-dimensional model of this transient behavior will be presented in conjunction with simulation results of the entire self-assembly process obtained using Surface Evolver. The parameters needed to find the equilibrium angle of a tile are: the shape of the base, the length and width of the tiles, and the size of the supporting ring. Figure 3.4 depicts a skew perspective of a potential configuration as well as a section along the x-z axes. The x and z axes are used to provide reference to the two-dimensional projection seen on the right panel of Figure 3.4. The operative assumptions are that: the tile is attached to the base via a frictionless hinge and that the soap film that connects the tile to the supporting frame can be represented by a catenary curve in the plane defined by the axes x and z. Like the angle introduced in Section 1 of Chapter 2, the angle ϕ in Figure 3.4 is determined by the angle between the soap film and the z-axis at the point where the soap film meets the tile. The angle of a tile as it deflects away from the plane containing the base is denoted by θ. Since the tile is fixed along one edge, the torques $\mathcal{T}_g$ and $\mathcal{T}_\sigma$ that gravity and surface tension exert on the tile must be balanced in equilibrium. For a tile of mass m and a soap film with surface tension σ, these torques depend on the angles ϕ and θ according to

$$\mathcal{T}_g = \frac{Lmg\cos\theta}{2}, \qquad \mathcal{T}_\sigma = 2Lw\sigma\cos(\theta+\phi). \tag{3.2.1}$$

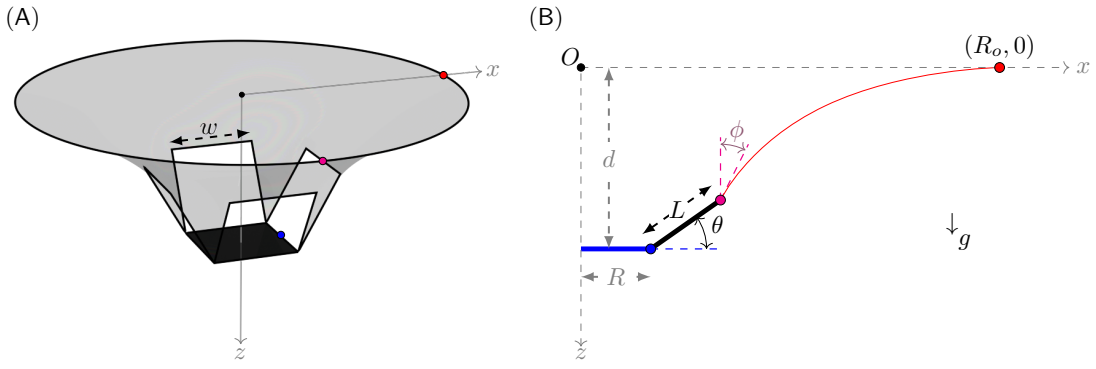


Figure 3.4: Schematic of the two-dimensional approximation of a tile resting on a square base while supported by a soap film. The soap-film membrane is shown in red, the base in blue, and the tile of length L and width w in black. The coordinate system is centered at the origin as denoted by O, with the positive z axis downward and the x axis to the right. The force due to gravity is acting along the positive z axis. All other relevant lengths and angles are labeled within the (x, z)-plane shown on the right-hand panel.

The equilibrium condition $\mathcal{T}_g = \mathcal{T}_\sigma$ can therefore be expressed as

$$\frac{mg}{4w\sigma} = \frac{\cos(\phi+\theta)}{\cos\theta}. \tag{3.2.2}$$

The left-hand side of (3.2.2) can be recognized as the Bond number B_t of the system. Experimentally θ is observed to obey

$$-\frac{\pi}{6} \lesssim \theta \lesssim \frac{\pi}{2}. \tag{3.2.3}$$

If θ is treated as a given quantity, the right-hand side of (3.2.2) is a function of only ϕ and has a unique maximum within its allowable range. The maximum can be found by setting the derivative of (3.2.2) with respect to ϕ equal to zero, giving $\sin(\phi+\theta) = 0$ or, equivalently,

$$\phi = -\theta. \tag{3.2.4}$$

Evaluating (3.2.2) for $\theta = -\pi/3$ and $\phi = \pi/3$ results in $B_t = 1.1547$. This is the maximal value of B_t for observable angles $\theta \geq -\pi/3$, interestingly taking $\theta \geq 0$ results in a maximal Bond number of one. Therefore, the subsequent analysis for the transient tile angles shares the Bond number regime for gravity-mediated assemblies described in Chapter 2. More generally, (3.2.2) affords the following relation for ϕ in terms of B_t and θ:

$$\phi = \cos^{-1}(B_t\cos\theta) - \theta. \tag{3.2.5}$$

Note that ϕ as indicated in Figure 3.4 is identically defined in Chapter 2. Let f be a function of the z coordinate representing the red curve depicted in Figure 3.4. The endpoints of the red curve depicted in Figure 3.4 are $(R+L\cos\theta, d-L\sin\theta)$ and $(R_o, 0)$. The assumption underlying the torque balance is that the intersection of the film with the quarter plane $\{(x,z) : x \geq 0, z \geq 0\}$, depicted as the red curve in Figure 3.4, is a catenary curve between the two endpoints. Under this assumption, the function f representing the red curve is given by

$$\begin{cases} f(z) = \dfrac{\cosh(\sqrt{C_1}(z+C_2))}{\sqrt{C_1}} & 0 \leq z \leq d - L\sin\theta. \qquad (3.2.6) \\ C_1 = \dfrac{1+f'(d-L\sin\theta)^2}{(R_i+L\cos\theta)^2}, & (3.2.7) \\ C_2 = \dfrac{\cosh^{-1}(R_o\sqrt{C_1})}{\sqrt{C_1}}. & (3.2.8) \end{cases}$$

The difference between (3.2.6) and (2.2.20) is in its domain of definition, which accounts for the angle θ at which the tile is inclined. C_2 can be written in terms of C_1, and C_1 can be written in terms of f', as shown in Section 2.2.2 and Appendix A.2. By the definition of ϕ and f, $f'(d-L\sin\theta) = \tan\phi$. Using this relation and (3.2.5), (3.2.7) can be written as

$$C_1 = \frac{1}{\cos[\cos^{-1}(B_t\cos\theta)-\theta]^2}\frac{1}{(R_i+L\cos\theta)^2}. \tag{3.2.9}$$

Using (3.2.8) and (3.2.9), (3.2.6) can be written in terms of R_i, R_o, L, B_t, and θ. Once again, each length is divided by the radius R_o of the supporting ring to yield a corresponding dimensionless quantity. Nondimensional parameters are denoted with a superscript asterisk, and g is defined by

$$g(B_t,\theta)=\cos[\cos^{-1}(B_t\cos\theta)-\theta],\qquad 0\le B_t\le 1.1547,\qquad -\frac{\pi}{6}\le\theta\le\frac{\pi}{2}. \tag{3.2.10}$$

Thus, the nondimensional closed-form solution of (3.2.6) is given by

$$\begin{aligned} f^*(z^*) &= \frac{\cosh(\sqrt{C_1}(z^*+C_2))}{\sqrt{C_1}} \\ &= (R^*+L^*\cos\theta)g(B_t,\theta)\cosh\left[\frac{z^*}{(R^*+L^*\cos\theta)g(B_t,\theta)}\right. \\ &\qquad \left.+\cosh^{-1}\left(\frac{1}{(R^*+L^*\cos\theta)g(B_t,\theta)}\right)\right]. \end{aligned} \tag{3.2.11}$$

where f^* is the dimensionless displacement of the base from the supporting ring, $g(B_t,\theta)$ is a function of the Bond number B_t and θ, R^* is the dimensionless radius of the supporting base, L^* is the dimensionless length of the tile, and θ is the angle between the tile and the plane containing the base. The Bond number is given by $B_t=mg/4w\sigma$, where: m is the mass of the tile, g is the acceleration due to gravity, w is the width of the tile, and σ is the surface tension of the soap film. An additional boundary condition is that f evaluated at the junction of the tile and the soap film must satisfy

$$f(d^*-L^*\sin\theta)=R^*+L^*\cos\theta. \tag{3.2.12}$$

Thus, by (3.2.11) and (3.2.12) an expression for the unknown θ is given by

$$\begin{aligned} R^*+L^*\cos\theta = (R^*+L^*\cos\theta)g(B_t,\theta)\cosh\left[\frac{d^*-L^*\sin\theta}{(R^*+L^*\cos\theta)g(B_t,\theta)}\right. \\ \left.+\cosh^{-1}\left(\frac{1}{(R^*+L^*\cos\theta)g(B_t,\theta)}\right)\right]. \end{aligned} \tag{3.2.13}$$

(3.2.13) can be rearranged and simplified such that d^* is written in terms of the other parameters as follows,

$$\begin{aligned} d^* = (R^*+L^*\cos\theta)g(B_t,\theta)\left[\cosh^{-1}\left(\frac{1}{g(B_t,\theta)}\right)-\cosh^{-1}\left(\frac{1}{(R^*+L^*\cos\theta)g(B_t,\theta)}\right)\right] \\ +L^*\sin\theta. \end{aligned} \tag{3.2.14}$$

Figure 3.5 shows two contour plots relating to the solution of (3.2.13) for two base geometries given fixed R^*. Each curve in Figure 3.5 corresponds to a fixed value of θ; (3.2.14) can be used to obtain d^* as a function of L^* for fixed R^*, B_t, and θ. To compare the theoretical predictions to the experimental results, sections of the contour plots are taken for fixed values of L^*. Figure 3.6 and Figure 3.7 show two such sections

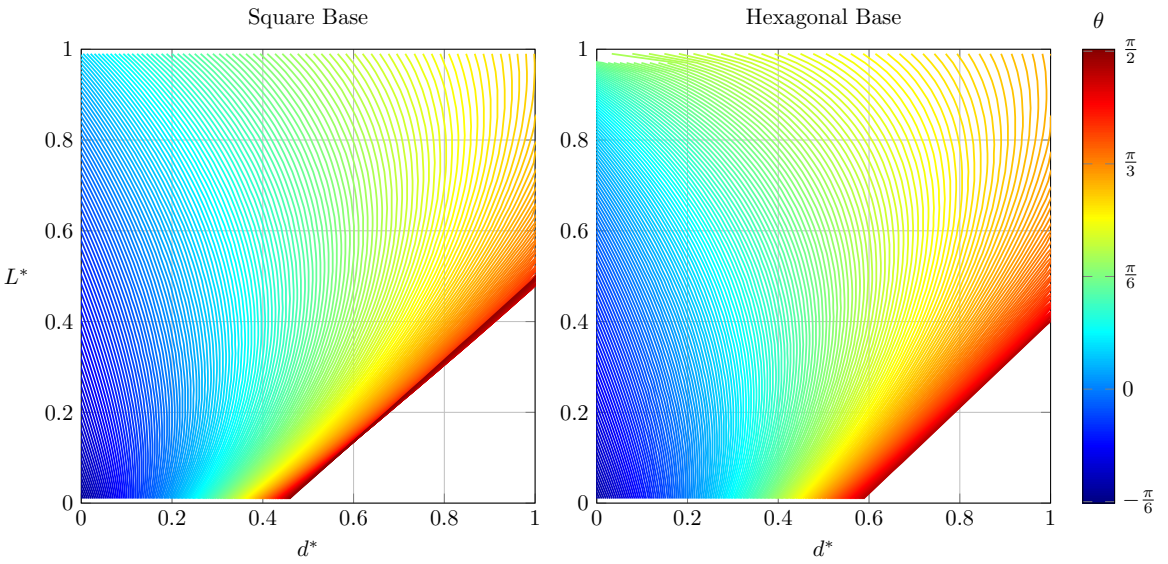


Figure 3.5: Contour Plots of (3.2.13) given physically relevant parameters. Here the mass of the tile is 0.05 g, the length and width of the tile are both 2 cm, and the surface tension of the soap film is 0.024 mN/m, which corresponds to a Bond number of $B_t = 0.51$. The radius of the base is $R^* = 0.2$ for the square base and $R^* = 0.34641$ for the hexagonal base. The calculations were carried out using Mathematica.

for the case in which the tiles are square with a side length of 2 cm Both figures afford comparisons between the experimental results and the proposed model after the appropriate image analysis. Figure 3.6 depicts the experiments using square tiles with an average mass of 0.0577 g. Equivalently, Figure 3.7 depicts experimental results for tiles with an average mass of 0.1704 g.

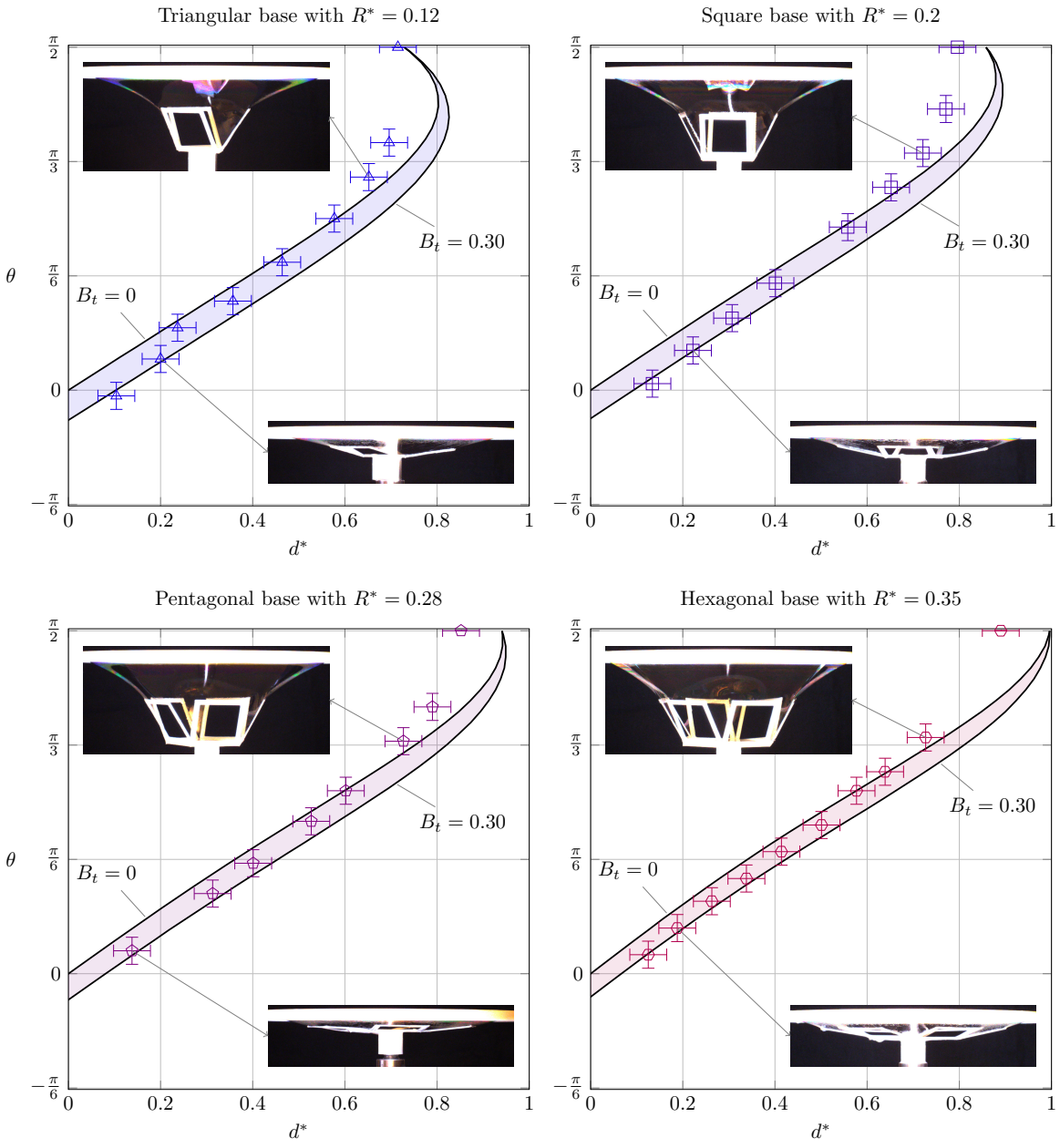


Figure 3.6: Solutions of (3.2.14) corresponding to experiments conducted with square tiles of thickness 0.5 mm and an average mass of 0.0577 g. The lower bounding curve of the shaded regions corresponds to a Bond number of $B_t = 0.3$ while the upper bounding curve corresponds to $B_t = 0$. The $B_t = 0$ curves are presented to show the expected angles of massless tiles, where surface forces dominate. For $d^* < 0.4$, the experimental results closely follow the theoretical prediction of the nonzero Bond number. While for $0.4 < d^* < 0.7$, the $B_t = 0$ solution appears to better approximate the results. And for $\theta > \pi/3$ the theoretical predictions deviate from the observed angles. Each base is a regular polygon with side length 2 cm, corresponding to a different R^*, as labeled. The tiles are all squares of side length 2 cm, meaning that $L^* = 0.4$ for all plots.

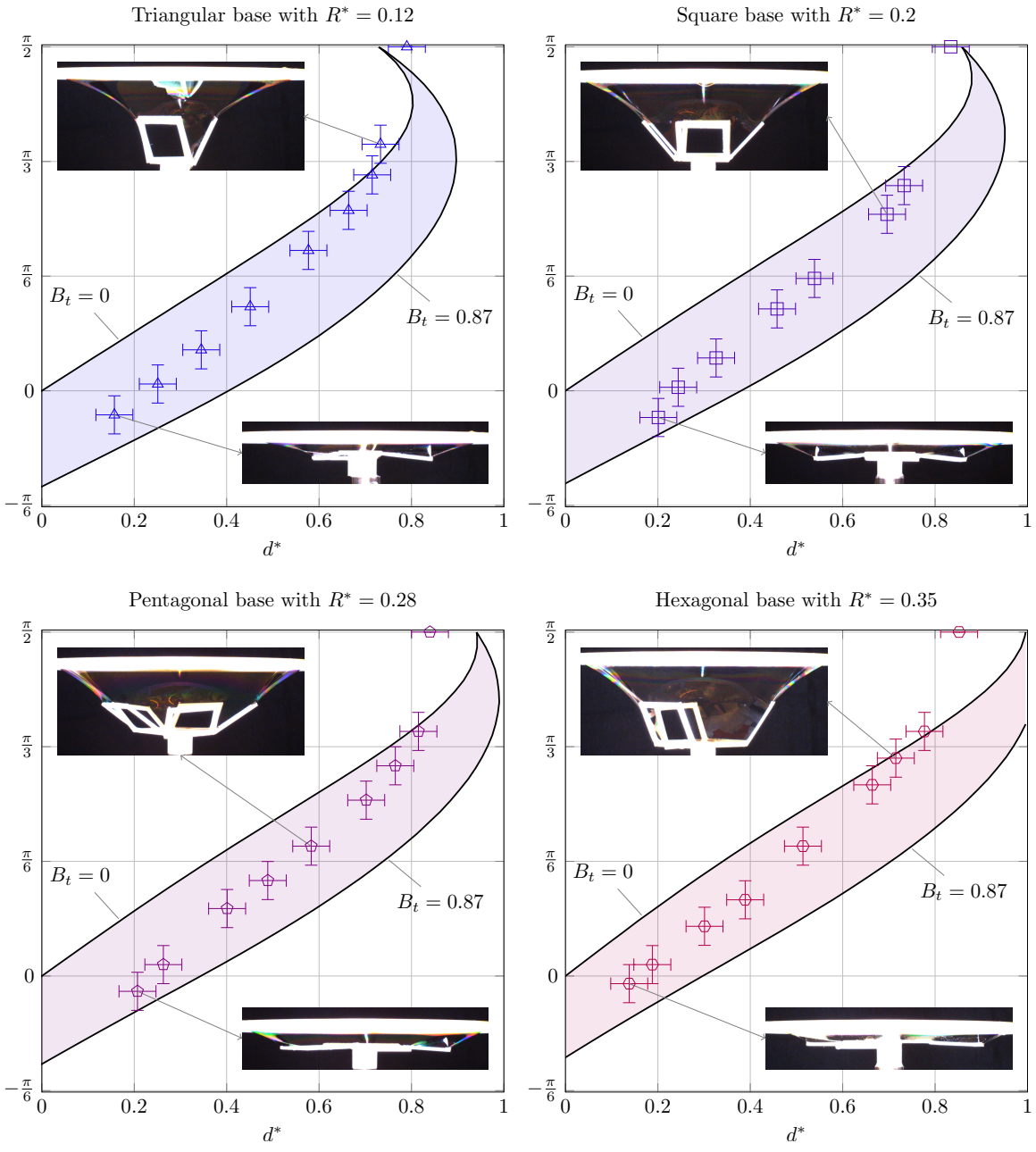


Figure 3.7: Solutions of (3.2.14) corresponding to experiments conducted with square tiles of thickness 1 mm and an average mass of 0.1704 g. Again, the theoretical prediction corresponding to $B_t = 0.87$ is compared to a masses tile prediction given by $B_t = 0$. Similarly to the accordance found in Figure 3.6, as d^* increases, the experimental results appear to be better approximated by the $B_t = 0$ curve. The implications are that as d^*, and consequently θ, increase, the interactions between tiles become dominant, and the effects of the force due to gravity diminish. Each base is a regular polygon with side length 2 cm, corresponding to a different R^*, as labeled. The tiles are all squares of side length 2 cm, meaning that $L^* = 0.4$ for all plots. The experiments corresponding to the hexagonal base only contain three tiles to ensure the clarity of the angle.

As depicted in Figure 3.6 and Figure 3.7, the proposed model does not accurately represent the experimental data for all values of d^*. To better understand the effects of the neighboring tiles on the equilibrium transient angle of an individual tile, Surface Evolver is used to implement a numerical scheme. Instead of directly coupling the force due to gravity and the force due to surface tension within Surface Evolver, each is calculated independently. Note that the force due to gravity is easily calculated from (3.2.1), given the relevant physical parameters and the angle θ. Focusing on the force due to surface tension, a similar method to that used in Chapter 2 is proposed. Consider explicitly calculating the force, equivalently the torque, acting on each vertex that is a part of the "tile" within the Surface Evolver simulations. The force due to surface tension is calculated using the `v_force()` method identically as in Section 2.4 except that two variables instead of one must be changed, within appropriate ranges, both the displacement d^* and the angle θ must be varied. Figure 3.8 shows nine combinations of d^* and θ for which the torque due to surface tension was calculated. The torque due to surface tension is considered positive if the induced rotation of the tile is counterclockwise for the tile intersecting the x–z plane given by the two grey lines in each simulation depicted in Figure 3.8. Note that the torque due to surface tension can be negative, as calculated from the simulation in Figure 3.8 corresponding to $d^* = 0.7$ and $\theta = 1.5$.

The Surface Evolver simulations were conducted by first fixing the displacement d^* and then calculating the torque due to surface tension for multiple values of θ. Figure 3.9 shows the results of these simulations. The curves corresponding to eight displacement values illustrate the numerical scheme. The curves representing the force

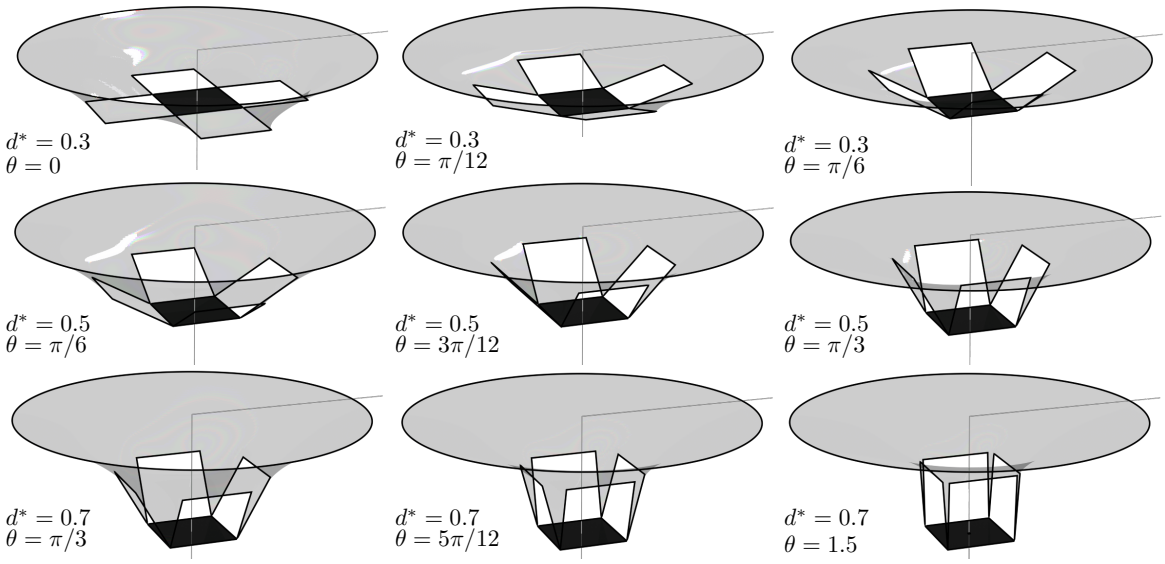


Figure 3.8: Without coupling the force due to gravity and the force due to surface tension acting on a tile within the prismatic assemblies, the entire range of potential displacements d^* and angles θ can be explored using Surface Evolver. Nine such combinations are shown to illustrate the simulations that were conducted. The force acting on the tile at each vertex can be calculated, similarly to the process described in Chapter 2; thereby, the torque acting on the tile can be found. The grey lines are the same x and z axes seen in Figure 3.4, and the black square is the base from which the displacement d^* is measured.

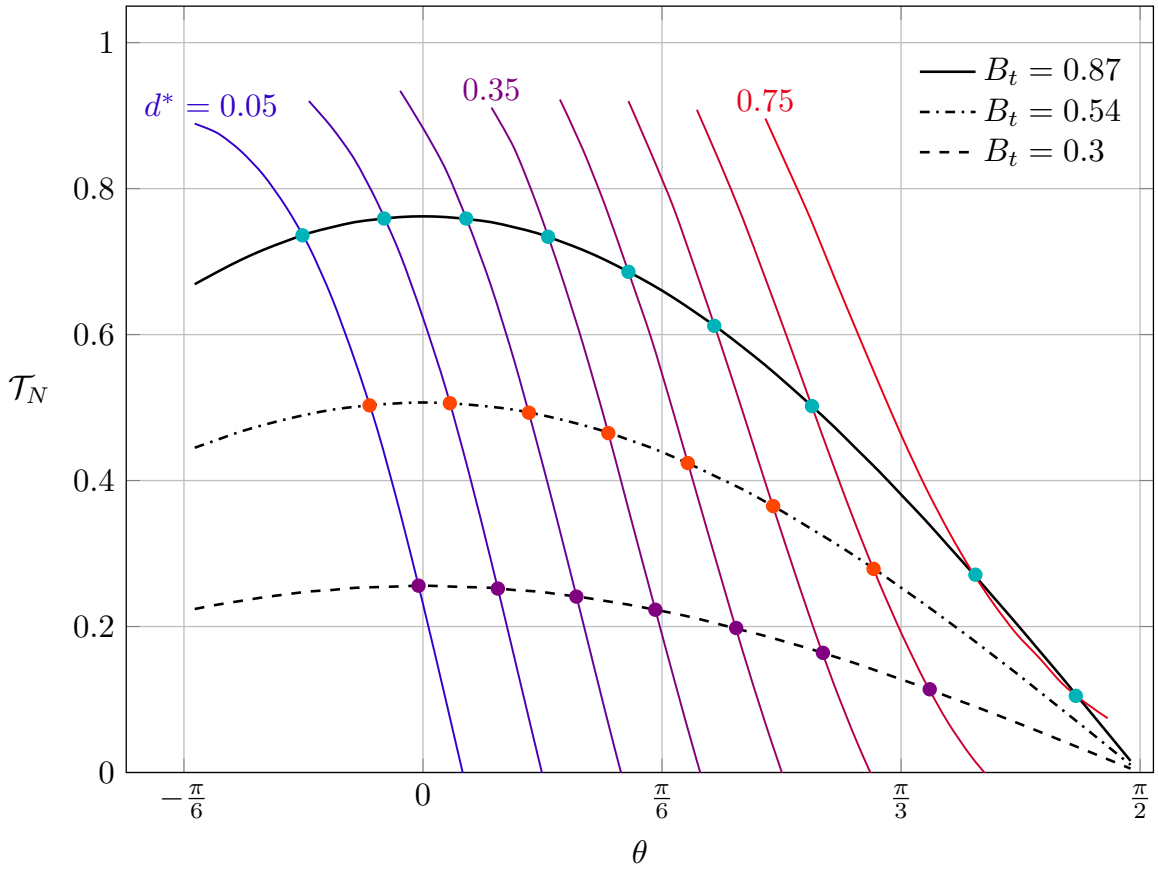


Figure 3.9: The torque due to surface tension acting on a tile is calculated as described in Figure 3.8. The torque $\mathcal{T}_N$ is normalized by $\max(B_t)4w\sigma$, or equivalently the maximal torque due to gravity given the maximal mass of a tile calculated by use of (3.2.2). Each curve denoted by $d^* = 0.05, 0.35$, and 0.75 corresponds to a particular displacement and for each d^* the torque is calculated for each θ. Intersecting these curves are the solid, dash-dotted, and dashed curves corresponding to the torque due to gravity. The torque due to gravity can be calculated by $\mathcal{T}_g = Lmg\cos\theta/2$ from (3.2.1). The intersection points of the two sets of curves depicted are the same as those seen in Figure 3.10 and Figure 3.11.

due to surface tension are juxtaposed to three curves representing the torque due to gravity, corresponding to $B_t = 0.3, 0.54, 0.87$ as labeled. By use of (3.2.1), $\mathcal{T}_g$ can easily be calculated. The intersections of these two sets of curves determine the pairs of displacement d^* and angle θ used to model the experimental data for each corresponding Bond number. Take for example the curve seen in Figure 3.9 labeled $d^* = 0.05$, it intersects the curve corresponding to $B_t = 0.3$ at approximately $\theta = 0$, meaning the curve corresponding to the numerical simulations found in Figure 3.10 should pass through these two values.

Note that as seen in the left panel of Figure 3.10 the curve corresponding to the Surface Evolver simulations has been shifted by 0.04 to account for the thickness of the base and the tiles. Within Surface Evolver, a soap film is assumed to be of zero thickness, and so the results do not accurately represent the physical reality. For the curve corresponding to $B_t = 0.54$ in Figure 3.9, additional experiments were conducted to consider the variation of the width, w, of the tiles while maintaining the inscribed

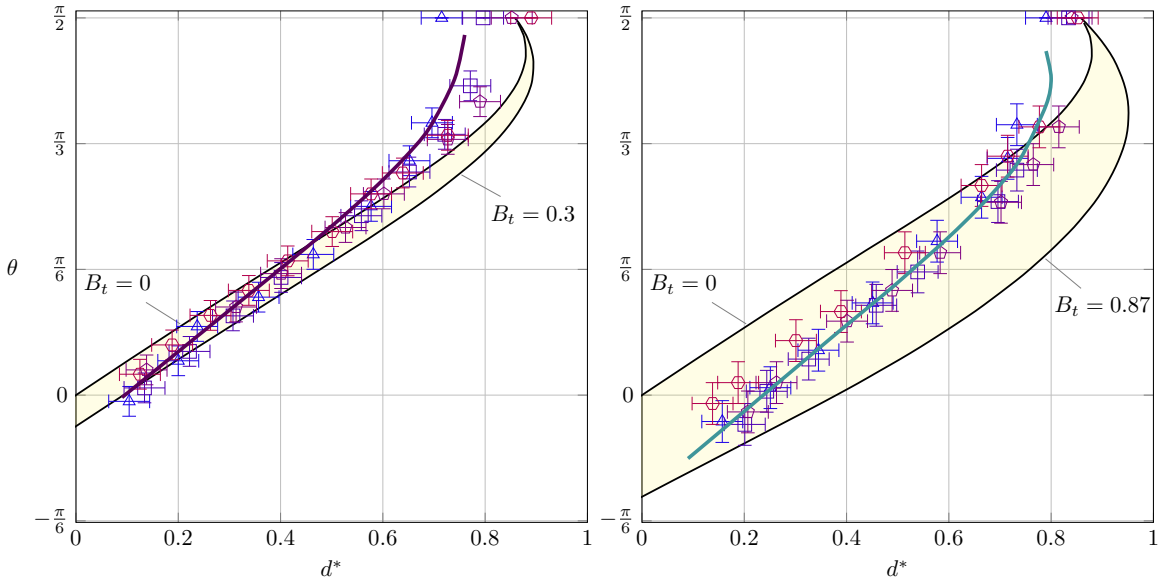


Figure 3.10: Additional experimental verification of the proposed model and comparison to simulations carried out using Surface Evolver. The empty data points shown correspond to geometries with a base shape given by the shape of the datapoint mark. Triangular $R^* = 0.12$, square $R^* = 0.2$, pentagonal $R^* = 0.28$ and hexagonal $R^* = 0.35$ bases as seen in Figure 3.3 Column 1. The left panel coalesces the experimental data points depicted in Figure 3.6 into a single plot, and the right panel similarly shows the aggregation of data points depicted in Figure 3.7. The solid circular marks are replicated from Figure 3.9 and define the line corresponding to the Surface Evolver simulations. The simulation results more closely approximate the experimental results for the entire range of d^* compared to the theoretical predictions.

radius, R^*, of the base fixed. Figure 3.11 depicts the results of these experiments. The edge lengths of the bases match the widths of the supported tiles and are given by: $R_i = 3.5$ cm for the triangular base, $R_i = 2$ cm for the square base, $R_i = 1.5$ cm for the pentagonal base, and $R_i = 1.2$ cm for the hexagonal base. The lengths of the tiles were kept fixed at 2 cm.

An interesting observation when comparing the analytical and numerical models to the experimental data is that there are no experimental values of $5\pi/12 < \theta < \pi/2$, while the models depict an inflection point of sorts. For both the analytical model (3.2.14) and the numerical scheme seen in Figure 3.10 and Figure 3.11 there exist values of d^* for which multiple values of θ and predicted. And within the same regime, no experimentally realized combinations of d^* and θ exist. This is due to the qualitative change noted between columns 2 and 3 of Figure 3.3. Beyond a critical value of d^*, at which point multiple values of θ correspond to a single value of d^*, the tiles snap to the aligned positions corresponding to $\theta = \pi/2$. It is worthwhile to note that while a single analytical model does not correspond to the experimentally observed transient tiles angles, the critical distance at which the tiles reach $\theta = \pi/2$ is well approximated by the proposed model.

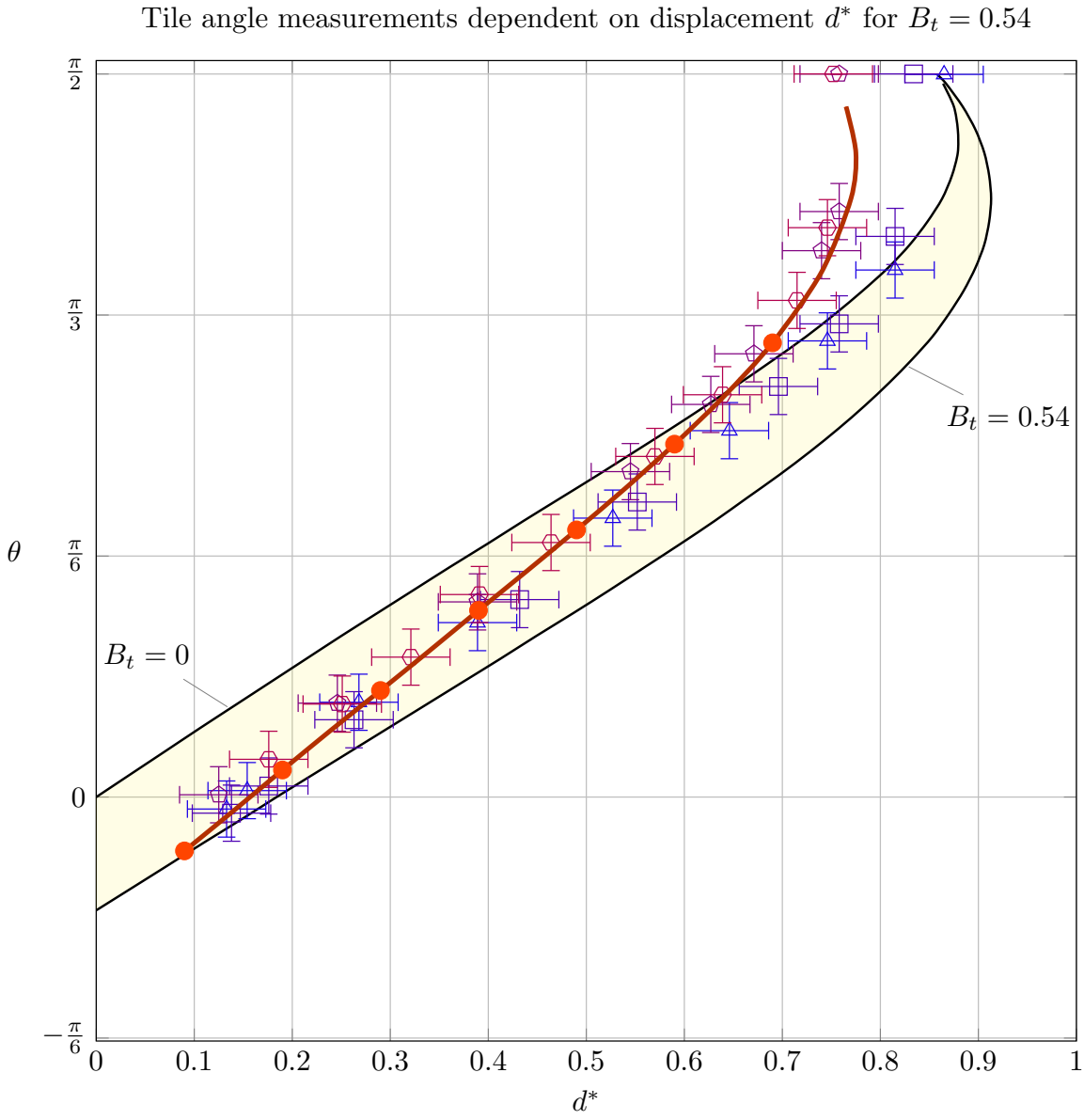


Figure 3.11: Figure 3.6 and Figure 3.7 show the correspondence of the experimental results and the proposed model. While the bond number is fixed within the two figures, the dimensionless radius varies. To further verify the observed correspondence, the Bond number of the experimental points seen here correspond to $R^* = 0.4$ and $B_t = 0.54$. Mark shape corresponds to the shape of the base. the error bars

3.2.2 Effective radius of prismatic nets

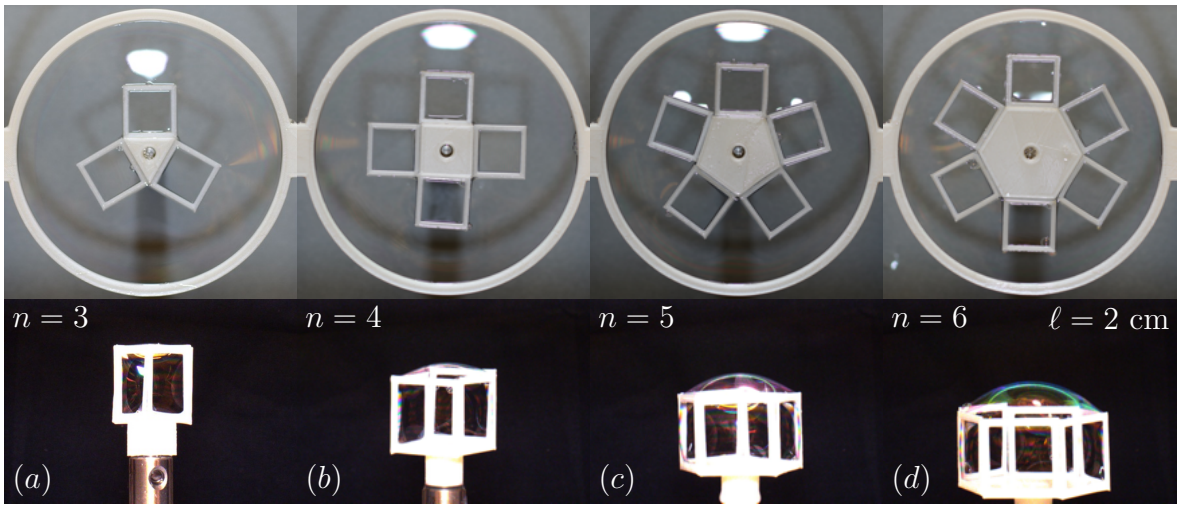


Figure 3.12: Self-Assembly of prism structures with a triangular, square, pentagonal, and hexagonal bases of 2 cm side width, the rectangular faces are of 2 cm height. The top image shows the initial net configuration, and the bottom the final displacement-driven assembly. n refers to the number of edges of the base and ℓ the edge length, ℓ being constant across all images seen. The process of assembly of these structures can be found in Appendix B. The structure in (c) is further detailed in Movie 2. Please refer to Movie 2, or go to the URL: `https://www.dropbox.com/s/ujukjasga05t7yp/Movie_2.mp4?dl=0` for a detailed view of the process.

Figure 3.13 shows the data of pinch-off distance from the supporting ring as it compares to the bounding limit of catenoidal solutions; the black line in Figure 3.13 is the same as derived in Chapter 2. The dimensionless height h^* is measured from the images in Figure 3.3. In Figure 3.13 the effective radius of prismatic assemblies is R_{e_1}/R_o where R_{e_1} is given by:

$$R_{e_1} = \sqrt{\frac{n\ell^2}{4\pi \tan\frac{\pi}{n}}}, \tag{3.2.15}$$

for n the number of sides of the polygonal base, and ℓ the length of each side as labeled in Figure 3.12. (3.2.15) is equivalent to finding the radius corresponding to the area of the base of the prism structures. As seen in Figure 3.3, the rectangular faces of the prism structures snap together; at this point, the boundary of the soap film has changed from a non-planer curve to one identical to that of its base. We expect that for prisms with square facets, the pinch-off of the assemblies will asymptotically approach the given limiting curve as the base approaches a circle. Figure 3.13 also shows the comparison of experimental and numerical results to the analytical prediction of catenoid-like soap film pinch-off. Numerical simulations were carried out with Surface Evolver identical to those described in Section 2.1.2, except that the lower bounding rings were replaced with polygonal boundaries. Simulations were conducted at each effective radius seen in Figure 3.13 for each boundary geometry: triangular, square, pentagonal, and hexagonal. The difference between the theory and numerical results appears to increase for triangular and square geometries, while pentagonal and hexago-

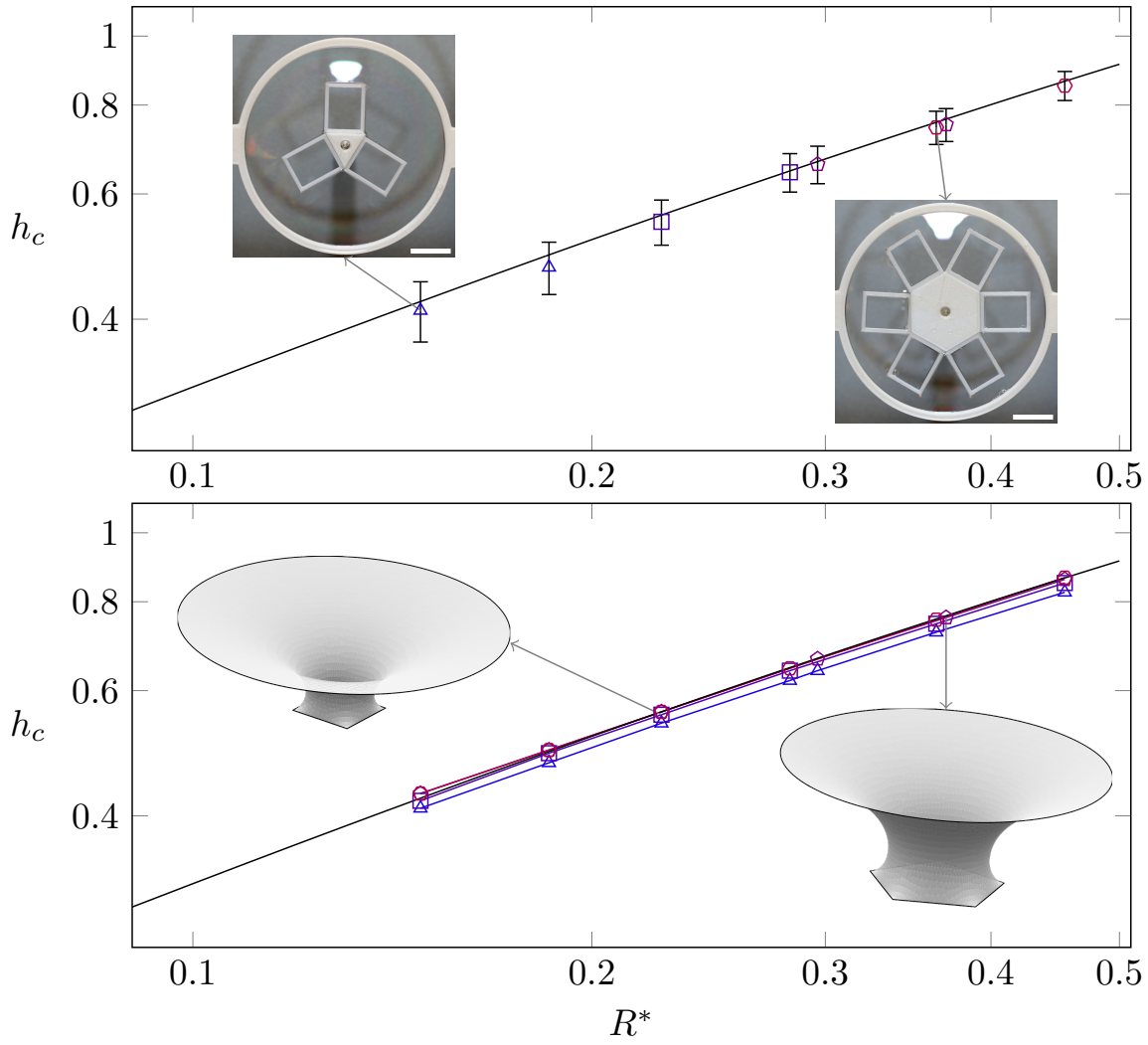


Figure 3.13: Data corresponding to the final deflections seen in Figure 3.3 of free-standing prism structures shown using a LogLog scaling. The black line is the limit of catenoidal soap film configurations as derived in Chapter 2. Mark shape corresponds to the shape of the base; triangular, square, pentagonal, and hexagonal. h^* and R^* are defined as shown in Figure 3.4. The dimensionless deflection scaled by the bounding radius $R_o = 5$ cm as is the effective radius of each data point R_{e_1}/R_o where R_{e_1} is the radius corresponding to the circle of equal area as the polygonal base, equivalently shown in (3.2.15). Points are averaged over two prism heights, and the error bars account for the error in measurement.

nal geometries fluctuate around the theorized limit. Given prism facets of non-unitary aspect ratios, the construction is dependent on the initial alignment of the components as seen in Figure 3.3 $(a_1) - (d_1)$. If one of the facets is miss-aligned during the start of the experiment, the construction will likely fail at the pinch-off stage as the asymmetry will cause the structure to fall.

3.2.3 Reversibility of assembly

The prismatic structures shown in Figure 3.12 (b), (c), and (d) all exhibit a soap film spanning the top of the tiles. This film can be used to invert the assembly process as

Figure 3.14 demonstrates. The reversibility of such structures is less consistent compared to the forward process. One should also note that extending the spanning soap film above the prismatic structure is necessary for the reverse process. The theorized mechanism of the reversibility is that the two soap film membranes coalesce, so the structures revert to a state similar to those seen in the second column of Figure 3.3. The joining of the two disjoint membranes is a much less understood process than the previously discussed pinch-off phenomena.

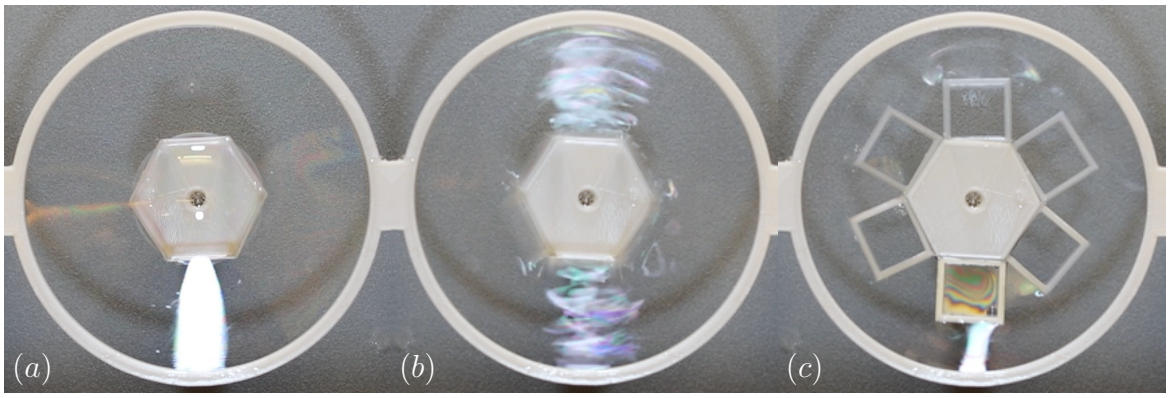


Figure 3.14: The hexagonal structure shown in Figure 3.12(*d*), with 2 cm height and identical side length, is raised until the soap film spanning the top of the structure comes into contact with the existing film spanning the support frame. (*b*) is the first contact between the two films. The elapsed time from image (*a*) to (*b*) and (*b*) to (*c*) is 200 ms. Following (*c*), the tiles suspended in the soap film reach an equilibrium angle, as described in Section 3.2.1, after approximately two seconds. Please refer to Movie 3, or go to the URL: `https://www.dropbox.com/s/hvp4fn64ccuut43/Movie_3.mp4?dl=0` for a detailed view of the process.

3.3 Pyramidal structures

Continuing with the analogy of building a house, once the walls have been raised, the roof needs to snap together. This section shows the construction of pyramidal structures atop a polygonal base. Figure 3.15 contains one of four pyramidal structures constructed on each base. The same bases as in Section 2 were used with similarly 3D printed components. The process seen in Figure 3.15 is stationary in time for all configurations of the tiles until the facets are perpendicular to the base. Following this configuration, seen in Figure 3.15 (c_3) and (d_3), the pinch-off of the catenoidal soap film is initiated. The symmetry breaking found in certain prismatic structures, as described in the previous section, also occurs in pyramidal structures. Row (d) in Figure 3.15 shows how the deposition of a component directly impacts the final structure. Prior to (d_1), the triangular tile on the lower left side was deposited with excess kinetic energy and thus did not align properly with the base edge. It could have been aligned manually prior to the initiation of the displacement, but the imperfection was small enough that the final structure was still stable. As all the tiles seen in Figure 3.15 are isosceles triangles, the deposition must be carried out in a particular fashion. Such tiles are held by tweezers at the vertex opposite the tile edge of 2 cm length. This is to ensure that the edge of the triangular tile aligns with the base as closely as possible after deposition.

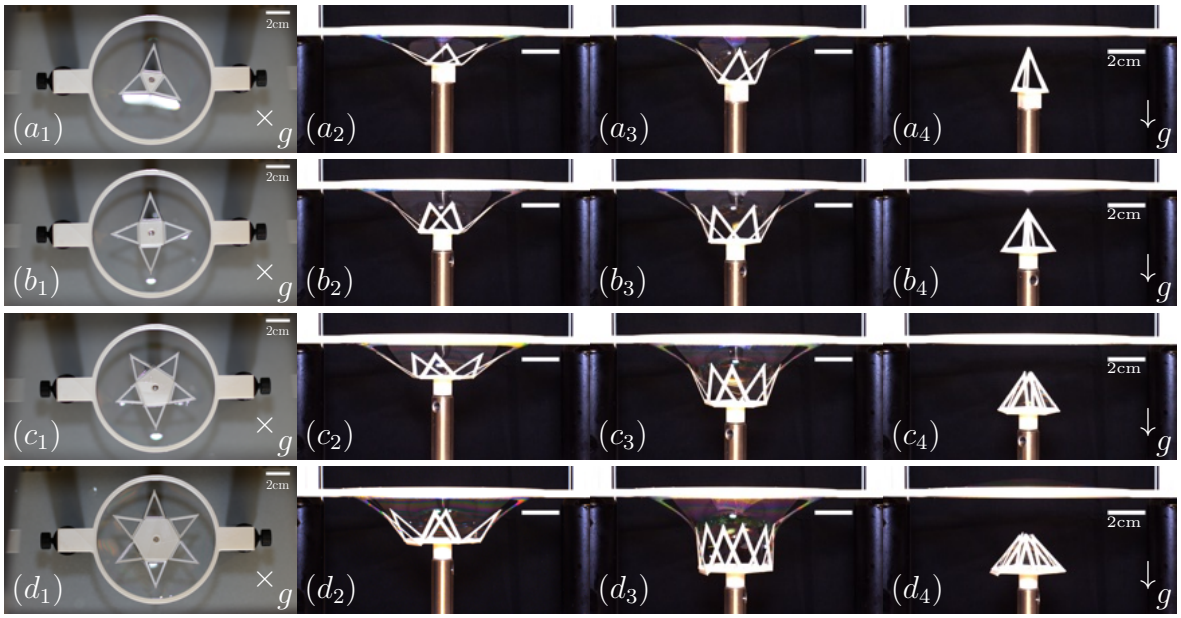


Figure 3.15: Self-Assembly of pyramid structures with triangular, square, pentagonal, and hexagonal bases of 20 mm side width. The long edges of the triangular facets measure 26 mm, corresponding to the largest heights, t_h, tested. Note that for rows (c) and (d), the triangular facets do not meet at the apex of the pyramid structure; this is due to the pinch-off behavior of the soap film. Appendix C contains additional images of pyramidal constructions. Movie 4 shows the deposition and construction of a pentagonal pyramid similar to that seen in row (c), but with equilateral triangular facets. The video can also be found at the following URL: `https://www.dropbox.com/s/gto8y1ifg6rk84a/Movie_4.mp4?dl=0`.

3.3.1 Effective radius of pyramidal nets

Regarding the constructions seen in Figure 3.15, we propose an alternative effective radius that determines the pinch-off distance of pyramid structures. One notable difference between the construction of prisms and pyramids is that the boundary between the soap film and the suspended facets does not revert to a planer boundary, which means that the snap-together phenomena seen in the prismatic structures, after which the soap film is still maintained, occurs simultaneously with the pinch-off of the catenoidal soap film. This coincidence of occurrence, pinch-off, and the pyramid snap together should be reflected in the effective radius of the process. As such, we consider the total area of the star shapes seen in Figure 3.15 $(a_1) - (d_1)$, the area of the triangular facets as well as the base. Finding the radius of a circle corresponding to the given area similarly to (3.2.15). Additionally, a parameter is needed to account for the different shapes of the triangular faces. The following expression is used to calculate the

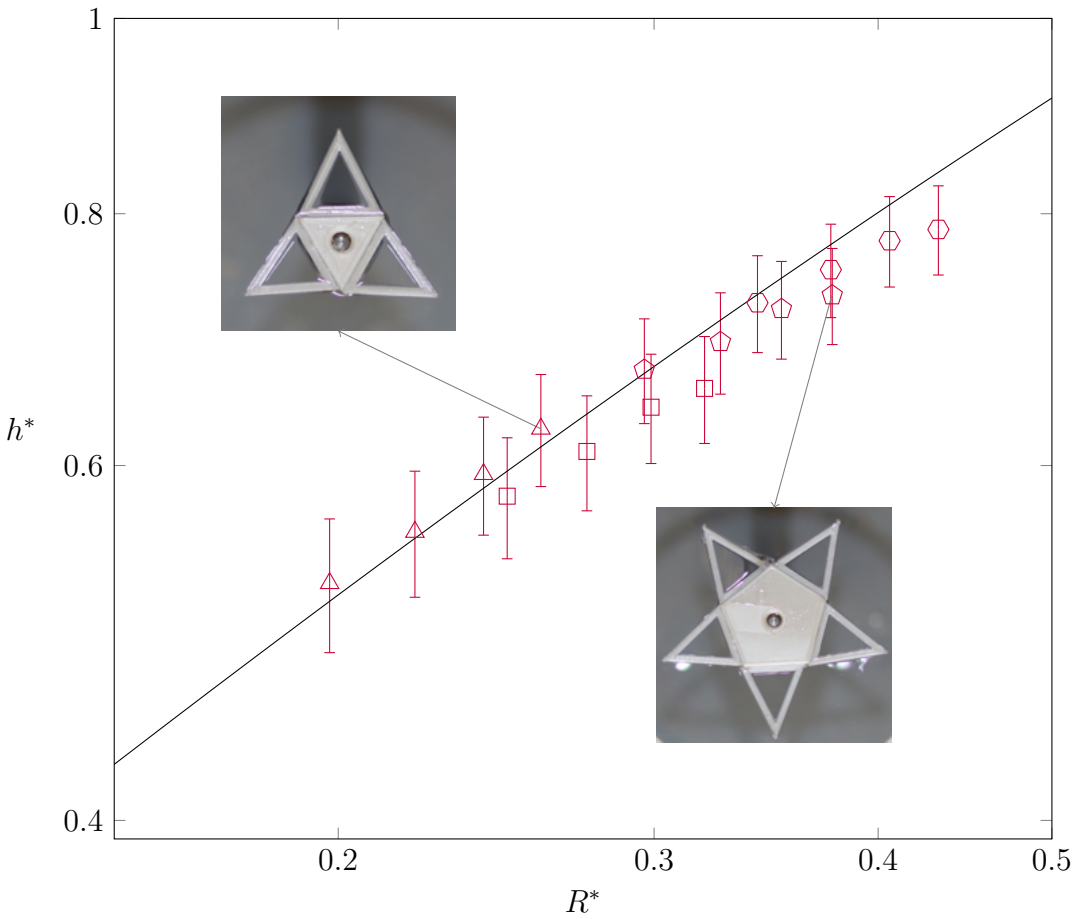


Figure 3.16: Data corresponding to the final deflections of pyramid structures seen in Figure 3.15 using a LogLog scaling. The black curve is the condition on the existence of catenoidal soap films, as seen in Figure 3.3 and derived in Chapter 2. Mark shape corresponds to the shape of the base; triangular, square, pentagonal, and hexagonal with side length 2 cm. For each base geometry, four different triangular facet heights were considered. The effective radius of each structure is R_{e_2}/R_o where the effective radius R_{e_2} is given in by (3.3.1) and takes into account the ratio between facet height and side length as well as the total area of the facets and base.

effective radii of the corresponding structures as found in Figure 3.16,

$$R_{e_2} = \frac{t_h - 2l_c}{\sqrt{t_h^2 + (\ell/2)^2}} \sqrt{\frac{n\ell t_h + \frac{n\ell^2}{2\tan\frac{\pi}{n}}}{2\pi}}. \tag{3.3.1}$$

Once more, for n the number of sides of the polygonal base, ℓ the length of each side, t_h being the height of the triangular facets, and l_c the capillary length, assumed to be $l_c = 2$ mm. The addition of the capillary length, in particular, accounts for the sharp edges of the facets.

3.3.2 Reversibility of assembly

The reversibility of pyramidal structures follows the same principle of prismatic geometries. A distinction is that we only expect pentagonal and hexagonal pyramidal structures to exhibit reversibility. Only these two base geometries have been shown to construct pyramidal geometries with a soap film spanning the apex of the pyramid. For triangular and square pyramidal structures, the tiles all appear to meet at the apex, as seen in Figure 3.15 and Appendix C. The sharp vertices of closed pyramidal structures will often puncture the soap film spanning the supporting ring. Figure 3.17 shows an identical view as seen in the previous section for the reversibility of a hexagonal pyramid. The structure shown in Figure 3.17 (a) is constructed from equilateral triangular tiles. The initial assembly process can be found in Figure C.4. As the tiles are equilateral and the base hexagonal, one should notice that the vertices of the tiles cannot touch. For this reason, this is one of the potential candidates to test the reversibility of pyramidal structures.

Note that, compared to the hexagonal prism in the previous section, Figure 3.17 (c) shows much more movement and displacement of the tiles. Figure 3.18 shows a

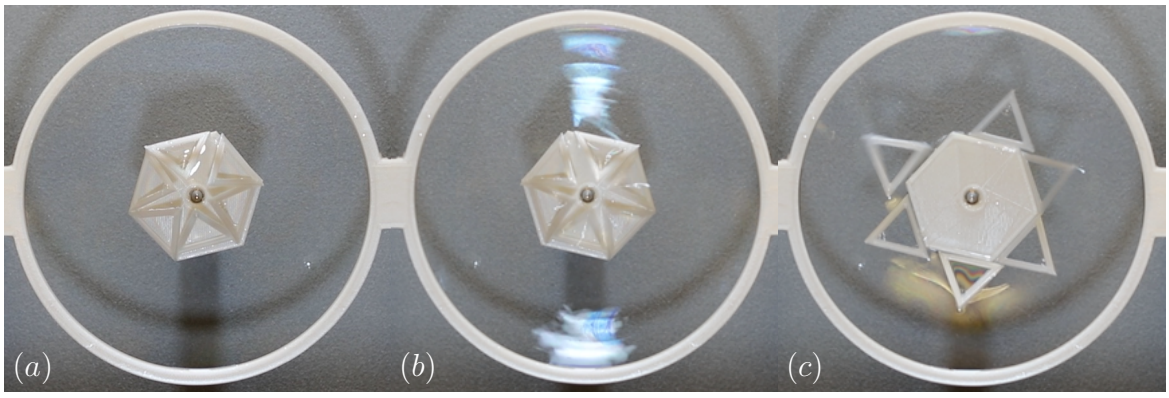


Figure 3.17: The hexagonal structure similar to that shown in Figure 3.15, except with equilateral triangular tiles, is raised until the soap film spanning the top of the structure comes into contact with the existing film spanning the support frame. (b) is the first contact between the two films. The elapsed time from image (a) to (b) and (b) to (c) is 200 ms. Following (c), the tiles suspended in the soap film reach an equilibrium after approximately two seconds. Please refer to Movie 5, or go to the url: `https://www.dropbox.com/s/o50bxuzdijbv2j8/Movie_5.mp4?dl=0` for a detailed view of the process.

similar process to that seen in Figure 3.17 but from the side. The side view shows that the process of inverting a pyramidal structure to its net orientation is much more explosive than observed in the prismatic case. This is likely due to the increased momentum of the tiles following the joining of the two soap film membranes. The tiles in the pyramidal geometry are moved from an angled position compared to the vertical position that the tiles of the prismatic structures start in prior to the opening of the structures.

3.4 Additional geometries

The displacement-driven assembly method presented in this chapter builds upon the gravity-mediated structures presented in Chapter 2. The addition of the supporting base significantly increases the number (and thereby total mass) of components that can reach equilibrium within the membrane. While only three suspended squares, as seen in Figure 2.16, approach the upper Bond number limit, the displacement-driven case allows for four and even five such tiles. Figure 3.19 shows a closed cubic structure made using the displacement-driven method. The construction of prisms and pyramids contains many subtle differences; Figure 3.19 and Figure 3.20 combine these two fundamental forms. While the previous sections show how to bring the walls of a house together and separately the construction of polygonal pyramids, the method presented in this chapter can also make closed structures. Figure 3.19$(a) - (e)$ follows the behavior of prism assemblies while from $(f) - (h)$ the pinch-off of the soap film resembles that seen in pyramid construction.

The phenomena seen in Figure 3.19 is a particular case as it contains a lid for the cube. The fifth square tile added to the assembly must be placed in a specific location. The size of the supporting frame is also relevant as its radius bounds the size of the potential assemblies. Figure 3.20 completes the house-building analogy mentioned at the start of this chapter. The careful deposition of four triangular tiles aligned with four square tiles atop a square base results in a simple house structure assembled by the displacement-driven method.

In addition to combining prismatic and pyramidal geometries, the presented method enables the assembly of octahedral geometries. Figure 3.21 portrays such a structure. The initial deposition of three additional triangular tiles while maintaining the symme-

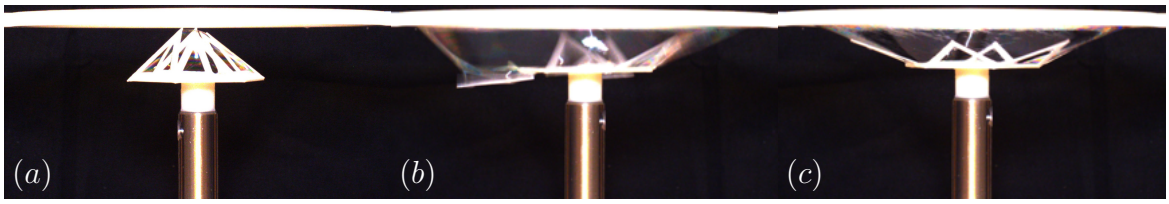


Figure 3.18: The hexagonal structure similar to that shown in Figure 3.17, except with triangular tiles of 21.81 mm height, is raised until the soap film spanning the top of the structure comes into contact with the existing film spanning the support frame. Time elapsed between frames (a) and (b) is 150 ms, and between (b) and (c) is approximately one second. Please refer to Movie 6, or go to the url: https://www.dropbox.com/s/w8nm81ixsf5lzvl/Movie_6.mp4?dl=0 for a detailed view of the process.

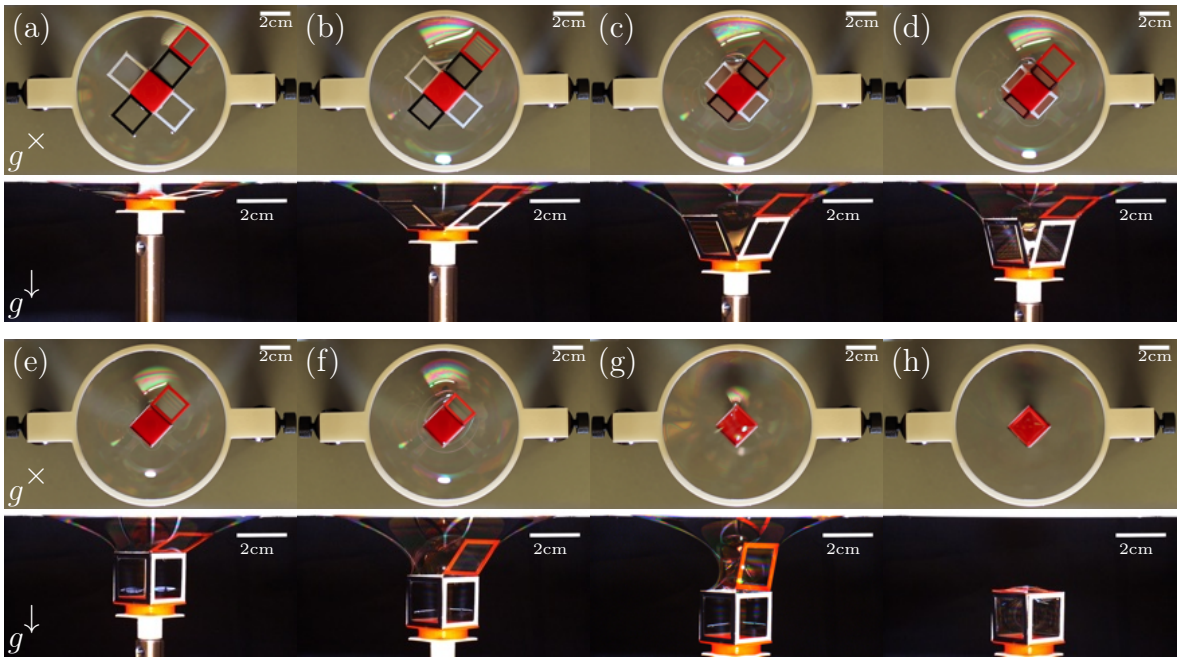


Figure 3.19: Simultaneous top and side views of a displacement-driven self-assembled cube with side lengths of 2 cm. The process is stable at each instance (a)-(f) and (h), while (g) is a frame captured during the snapping process. The phenomena observed between instances (f) and (g) resemble the pinch-off of a catenoid-shaped soap film during the transition to a Goldschmidt solution. Please refer to Movie 7, or go to the url: `https://www.dropbox.com/s/iwncru315dqp5gd/Movie_7.mp4?dl=0` for further details.

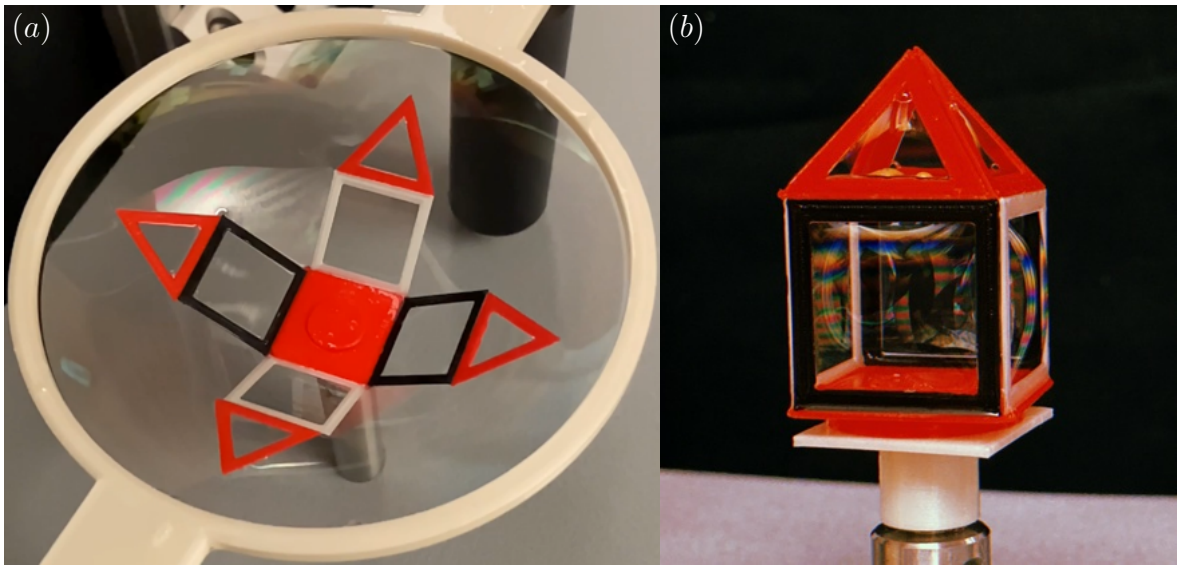


Figure 3.20: Self-Assembly of a square pyramidal structure atop a cube. We expect the pinch-off behavior to be similar to that of the pyramidal structures with square bases presented in Figure 3.15 and Figure C.2. The addition of the triangular tiles necessitates careful deposition to one of the four suitable placements for the construction to be stable. Please refer to Movie 8 , or go to the url: `https://www.dropbox.com/s/zkcu2ojl1zh9uzq/Movie_8.mp4?dl=0` for further details.

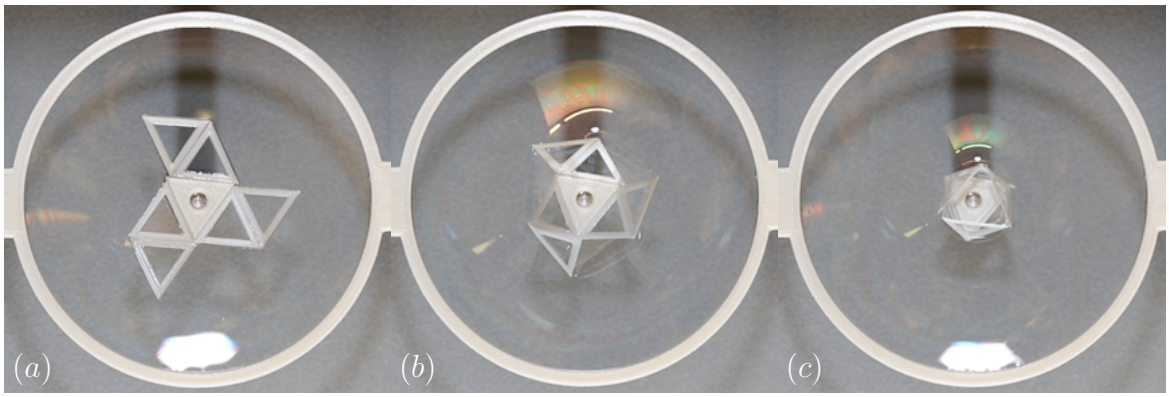


Figure 3.21: Self-Assembly of an octahedral structure with a triangular base of 2 cm side width. The pinch-off behavior is expected to be the same as for prismatic structures. The six triangular components exhibit a snapping and pinch-off process as observed in the prism structures detailed in Figure 3.3 and Appendix B.

try of the net allows for constructing an octahedral geometry without a lid. Figure 3.22 shows the corresponding closed structure with the addition of a seventh triangular tile. The addition of closed and octahedral geometries considerably broadens potential research avenues into such constructions and their applications.

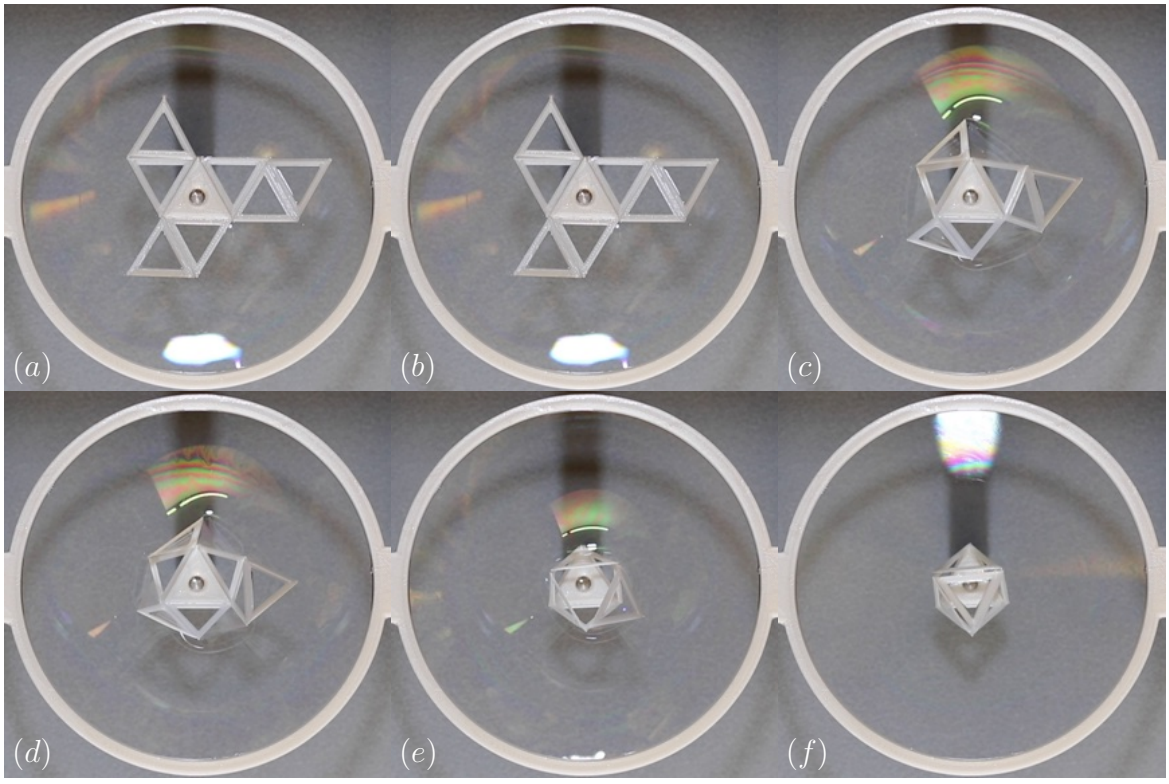


Figure 3.22: Self-Assembly of an octahedral structure with a triangular base of 2 cm side width and a lid. We expect the pinch-off behavior to be similar to that of the cube presented in Figure 3.19. Note that adding the seventh component (the lid) necessitates careful deposition to one of the three suitable placements for the construction to be stable. Please refer to Movie 9 , or go to the url: `https://www.dropbox.com/s/7x65isgjt5fhbf4/Movie_9.mp4?dl=0` for further details.

3.5 Self-folding

Additional experiments were conducted to show that self-folding of pre-patterned polyhedral nets can be accomplished using the presented method regardless of the orientation. Figure 3.23 shows the alignments of a cubic and an octahedral geometry in (a) and (b), respectively. 35 μm thick tape, seen in yellow, is used to join the edges and function as a hinge. The use of such a thin tape limits the resistance to bending and allows the structures to come together, as seen in Figure 3.24. The low resistance to bending allows the soap film's catenoid-like shape to arrange the tiles into the expected 3D structures. Following the soap film pinch-off, as seen in Figure 3.24 (b_3), the structure is held together by capillary adhesion. Once the soap film has pinched off, it spans the bounding ring of radius 5 cm and the top of the self-folded structure, thereby keeping the structure together. Figure 3.24 depicts a self-folding process with the base moving in the opposite direction as the direction of gravitational acceleration. (a_3) and (b_3) show the instances prior to and following the soap film pinch-off, respectively. In the absence of the soap film, the nets would find an equilibrium in an open position, as the resistance to bending of the tape is non-zero, and the force due to gravity is acting on the structure.

Figure 3.25 depicts the same structures, but the base is moving in a direction perpendicular to the direction of gravitational acceleration. Once more, the shape of the soap film immediately prior to pinch-off is well approximated by a catenoid, so the self-folding process is expected to exhibit the same phenomena described earlier in this chapter. These experiments show that the displacement-driven assembly methods investigated in this chapter are not restricted to small Bond numbers nor the geometries

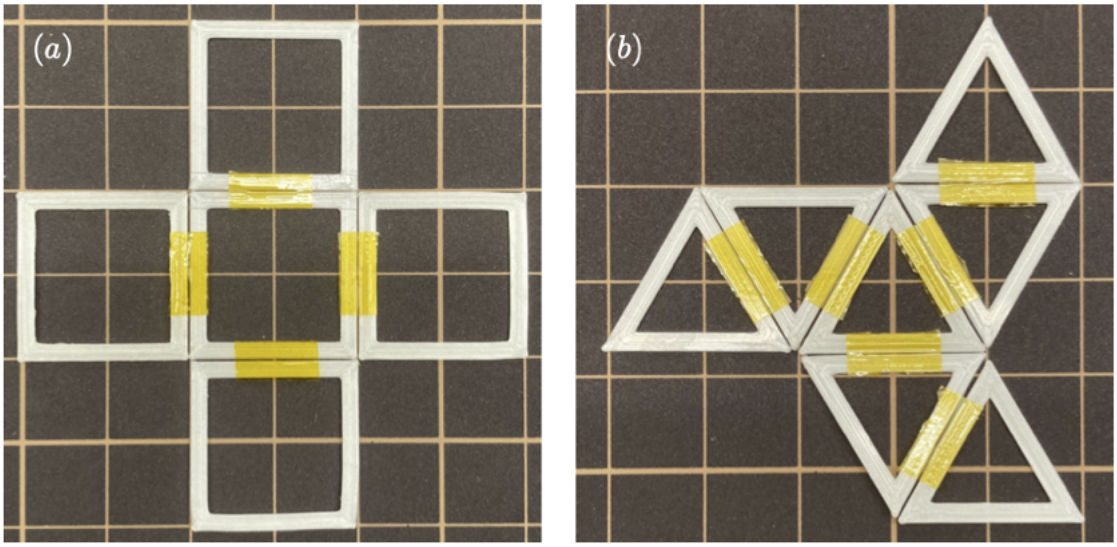


Figure 3.23: 2D nets of self-folding assemblies. (a) shows five squares of side length 2 cm held together at four edges by use of 35 μm thick tape. The tiles are 0.5 mm thick and have an average mass of 0.0577 g; the same tiles were used in Section 3.2 to investigate prismatic assembles. (b) shows seven equilateral triangles of side length 2 cm and thickness of 0.5 mm held together at six edges by use of the same 35 μm thick tape. The average mass of these triangles is 0.0391 g. The tape is applied to one side of the tiles, and the excess is trimmed to ensure that the tape functions as a hinge with as little resistance as possible.

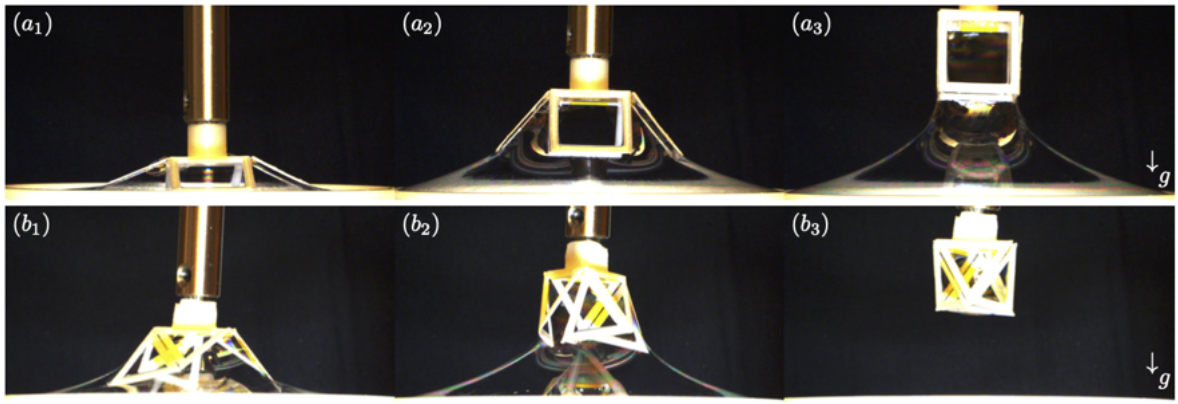


Figure 3.24: Row (a) depicts the progression of self-folding of a cube from the pattern shown in Figure 3.23(a). While row (b) depicts the same for an octahedral geometry. The critical separation distance between the base and the ring supporting the soap film is expected to be the same as described in Section 3.2.

presented in this thesis. The potential for future work regarding soap film mediated self-assembly and self-folding can even be considered in gravity-independent environments.

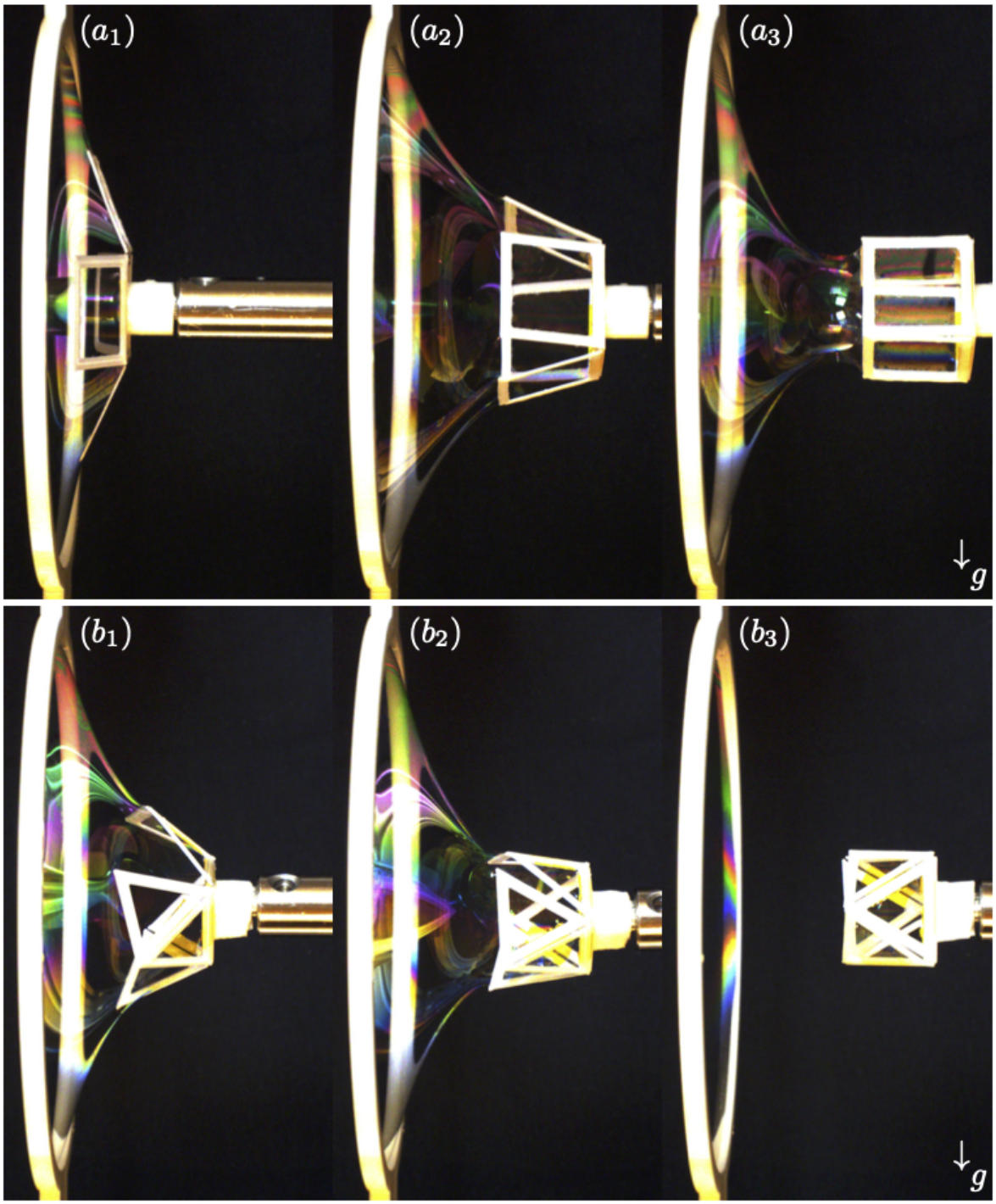


Figure 3.25: Self-folding perpendicular to the direction of gravitational acceleration is shown for cubic and octahedral structures. The camera is aligned such that the entirety of the ring, of radius 5 cm, can be observed. The soap film and tiles used are identical to those used previously.

Conclusions

This thesis has investigated the potential of self-assembly at centimeter length scales, demonstrating suspended platonic geometries, free-standing prismatic, pyramidal, and octahedral geometries. Extending the current capabilities of capillary-driven assemblies into larger length scales and away from self-folding systems. Iyer and Kolin [5] point to the current disadvantages of mesoscale self-assembly, being that processes are slow and that self-repair could be costly. But as described, the method presented in this thesis is highly reproducible and even reversible. Using soap film membranes, gravity-mediated assemblies were shown along with an axisymmetric model to bound the total mass and effective radii of such structures. In the context of displacement-driven assemblies, a catenoid-like soap film was used to assemble self-supported structures atop a base via the pinch-off instability of a catenoidal soap film. The pinch-off instability of a soap film has been well studied experimentally (by Robinson and Steen [70]), numerically (by Jana and Kar [87]), and theoretically (by Goldstein et al. [71]) as recently as 2021. Building upon the vast existing literature, this thesis has demonstrated a new method of self-assembly as well as another avenue of study considering the interactions of tiles and soap films.

Figure 4.1 combines these concepts into a phase space of existence for catenoidal soap films and the corresponding 3D assemblies. The dashed curve corresponds to the condition on the existence of a catenoid derived in Chapter 2. The red region above the dashed line corresponds to combinations of R^* and h^* such that a catenoid cannot span the two rings of defined radius given the separation between them. The transition to this region enables the assemblies found in Chapter 3, and it contains the fully assembled structures. The assembly of displacement-driven structures is found in the red area below the dashed line. The effective radii corresponding to prismatic and pyramidal displacement-driven assemblies, detailed in Chapter 3, provide a geometric interpretation of the tiles' effect on the pinch-off of a catenoid-like soap film. The blue region contains possible gravity-mediated assemblies. The bounding blue curve is the limiting solution of the system derived in Chapter 2, detailing a ring of given mass supported by a soap film that spans a bounding frame.

The blue curve seen in Figure 4.1 is an ideal bound on the existence of gravity-mediated assemblies. As described in Chapter 2 Section 3, even a suspended ring exhibits symmetry breaking for large Bond numbers. As the mass of a suspended structure increases, the induced flow and manufacturing imperfections lead to asymmetric equilibrium arrangements. While rings have been shown to be supported in such asymmetric configurations, this is not the case for gravity-mediated platonic assemblies. As such, an approximate bound on the total mass of a suspended assembly

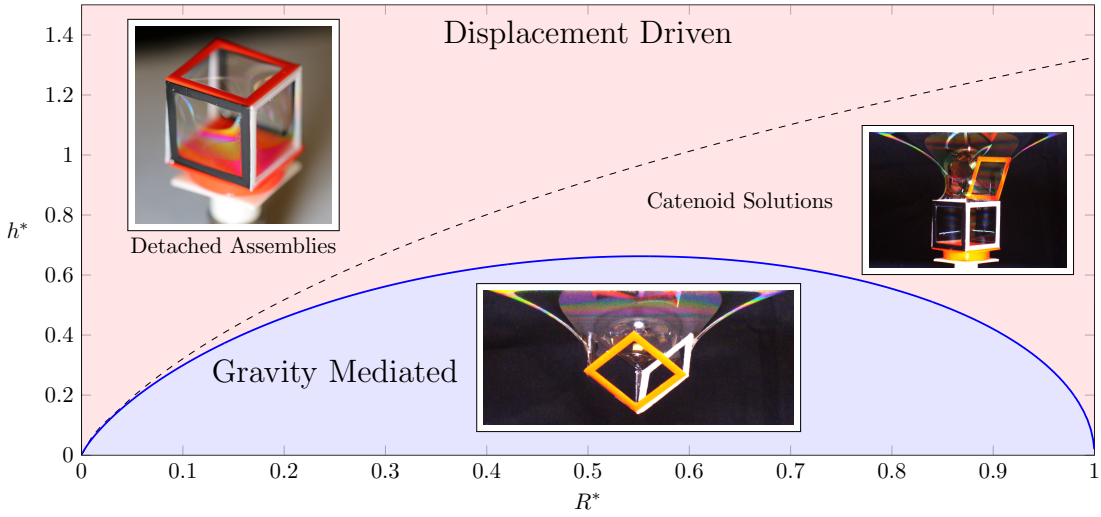


Figure 4.1: As previously noted, R^* is the ratio of the effective radius of an assembly and the radius of the bounding frame., h^* is the ratio of the separation displacement and the radius of the supporting ring. The dashed curve delimits the existence conditions of catenoidal soap film geometries. The detached assemblies correspond to discontinuous Goldschmidt solutions, while the catenoid solutions contain assemblies still attached to the catenoid-like soap film. The blue curve is the limit of gravity-mediated assemblies within a catenoidal soap film membrane, namely the solution of 2.2.27 for $B = 1$, shown in Chapter 2.

is considered. Given $B = 0.8$, the equilibrium displacements h^* are less than half the values corresponding to $B = 1$ for all R^*. I propose that the approximate bound of $B \leq 0.8$ is appropriate when considering physically realizable gravity-mediated assemblies. Another factor to consider is the boundary of the soap film as it interacts with a suspended structure. The boundary between the soap film and the tiles is a regular polygon for tetrahedral, octahedral, and icosahedral geometries. Chapter 3 Section 2 details how such polygonal boundaries admit an effective radius; this approximation applies to the gravity-mediated assemblies with corresponding shapes. For cubic and dodecahedral suspended geometries, the boundary between the soap film and the tiles is not planer. The existence of such gravity-mediated structures can be predicted partially by the Bond number approximation proposed in Chapter 2. Using Surface Evolver simulations, all assemblies were predicted to correspond to an effective radius.

Regarding displacement-driven assemblies, one should notice the imperfections in the constructions described in Chapter 3. The deposition of the tiles directly influences the final assembly. Imperfections in the alignment can lead to the collapse of an assembly, but the structures are found to be still formed for small-scale deviations. Additional experiments and analysis could aid in the development of a more consistent experimental procedure. The pinch-off phenomenon of catenoidal soap films is well studied, but with the addition of the tiles detailed in this thesis, the rate at which pinch-off occurs is an important distinction. More detailed experiments are needed to understand the effect of the tiles on the pinch-off process.

Future work could consider combining the self-assembly capabilities of the system demonstrated in this thesis with the photo-polymerization of a liquid film. The result of Ragelle et al. [11] could be integrated with the assembly processes of Chapter 3

to construct rigid structures. The structures shown in this thesis are only the fundamental building blocks of all possible assemblies, combining and rearranging these building blocks could lead to a multitude of additional assemblies. The potential of two-dimensional assemblies within a gravity-mediated system could be further investigated. The methods shown in this thesis could be used on larger length scales. Consider a liquid film of similar physical properties to a soap film. Still, with surface tension orders of magnitude higher, such a film would be able to construct structures with length scales on the order of meters. Increasing the length-scale of the assemblies presented in this thesis would enable further applications in packaging, robotics, and three-dimensional electronics.

Bibliography

[1] G. M. Whitesides and M. Boncheva. Beyond molecules: Self-assembly of mesoscopic and macroscopic components. *Proceedings of the National Academy of Sciences of the United States of America*, 99:4769–4774, 2002.

[2] Massimo Mastrangeli and Michele Perego. Bottom-up assembly of micro/nanostructures. *Advanced Materials Interfaces*, 7(5):2000182, 2020.

[3] Kai Cui and Zhilong Zhao. Bibliometric analysis on self-assembly research in nanoscale. *Journal of Nanoparticle Research*, 22(7):1–10, 2020.

[4] Katsuhiko Ariga, Jonathan P Hill, Michael V Lee, Ajayan Vinu, Richard Charvet, and Somobrata Acharya. Challenges and breakthroughs in recent research on self-assembly. *Science and technology of advanced materials*, 2008.

[5] Anusha Subramony Iyer and Kolin Paul. Self-assembly: a review of scope and applications. *IET nanobiotechnology*, 9(3):122–135, 2015.

[6] Jean Berthier. Micro-drops and digital microfluidics (second edition). pages 75–160. William Andrew Publishing, second edition edition, 2013.

[7] Caroline Cohen, Baptiste Darbois Texier, Etienne Reyssat, Jacco H Snoeijer, David Quéré, and Christophe Clanet. On the shape of giant soap bubbles. *Proceedings of the National Academy of Sciences*, 114(10):2515–2519, 2017.

[8] T. G. Leong, P. A. Lester, T. L. Koh, E. K. Call, and D. H. Gracias. Surface tension-driven self-folding polyhedra. *Langmuir*, 23:8747–8751, 2007.

[9] Ryan Kaplan, Joseph Klobušickỳ, Shivendra Pandey, David H Gracias, and Govind Menon. Building polyhedra by self-assembly: theory and experiment. *Artificial life*, 20(4):409–439, 2014.

[10] Michael T Tolley, Samuel M Felton, Shuhei Miyashita, Daniel Aukes, Daniela Rus, and Robert J Wood. Self-folding origami: shape memory composites activated by uniform heating. *Smart Materials and Structures*, 23(9):094006, 2014.

[11] Héloïse Ragelle, Mark W Tibbitt, Shang-Yun Wu, Michael A Castillo, George Z Cheng, Sidharta P Gangadharan, Daniel G Anderson, Michael J Cima, and Robert Langer. Surface tension-assisted additive manufacturing. *Nature communications*, 9(1):1–10, 2018.

[12] Seo Woo Song, Sumin Lee, Jun Kyu Choe, Na-Hyang Kim, Junwon Kang, Amos Chungwon Lee, Yeongjae Choi, Ahyoun Choi, Yunjin Jeong, Wooseok Lee, Ju-Young Kim, Sunghoon Kwon, and Jiyun Kim. Direct 2d-to-3d transformation of pen drawings. *Science Advances*, 7(13), 2021.

[13] Stoffel D. Janssens, Satoshi Koizumi, and Eliot Fried. Behavior of self-propelled acetone droplets in a Leidenfrost state on liquid substrates. *Physics of Fluids*, 29(3):032103, 2017.

[14] Carlo Marangoni. On the expansion of a drop of liquid floating on the surface of another liquid. *Tipographia dei fratelli Fusi, Pavia*, 1865.

[15] Thomas Henry Havelock. Wave resistance: some cases of three-dimensional fluid motion. *Proc. R. Soc. Lond. A*, 95(670):354–365, 1919.

[16] AD Chepelianskii, M Schindler, F Chevy, and E Raphaël. Self-consistent theory of capillary-gravity-wave generation by small moving objects. *Physical Review E*, 81(1):016306, 2010.

[17] Edward Bormashenko, Yelena Bormashenko, Roman Grynyov, Hadas Aharoni, Gene Whyman, and Bernard P. Binks. Self-propulsion of liquid marbles: Leidenfrost-like levitation driven by marangoni flow. *The Journal of Physical Chemistry C*, 119(18):9910–9915, 2015.

[18] Elie Raphaël and P-G De Gennes. Capillary gravity waves caused by a moving disturbance: wave resistance. *Physical Review E*, 53(4):3448, 1996.

[19] Birgitt Boschitsch Stogin, Luke Gockowski, Hannah Feldstein, Houston Claure, Jing Wang, and Tak-Sing Wong. Free-standing liquid membranes as unusual particle separators. *Science Advances*, 4(8), 2018.

[20] John A Pelesko. *Self assembly: the science of things that put themselves together*. CRC Press, 2007.

[21] G. M. Whitesides and B. Grzybowski. Self-assembly at all scales. *Science*, 295:2418–2421, 2002.

[22] R. Groß and M. Dorigo. Self-assembly at the macroscopic scale. In *Proceedings of the IEEE*, pages 1490–1508. **96**, 2008.

[23] Zhiyong Gu, Yiming Chen, and David H. Gracias. Surface tension driven self-assembly of bundles and networks of 200 nm diameter rods using a polymerizable adhesive. *Langmuir*, 20(26):11308–11311, 2004.

[24] L. Botto, L. Yao, R. L. Leheny, and K. J. Stebe. Capillary bond between rod-like particles and the micromechanics of particle-laden interfaces. *Soft Matter*, 8:4971–4979, 2012.

[25] Eric P. Lewandowski, Marcello Cavallaro, Lorenzo Botto, Jorge C. Bernate, Valeria Garbin, and Kathleen J. Stebe. Orientation and self-assembly of cylindrical particles by anisotropic capillary interactions. *Langmuir*, 26(19):15142–15154, 2010. PMID: 20806978.

[26] A. Terfort, N. Bowden, and G. M. Whitesides. Three-dimensional self-assembly of millimetre scale components. *Nature*, 386:162–164, 1997.

[27] Joe Tien, Andreas Terfort, and George M. Whitesides. Microfabrication through electrostatic self-assembly. *Langmuir*, 13(20):5349–5355, 1997.

[28] Sungho Park, Jung-Hyurk Lim, Sung-Wook Chung, and Chad A. Mirkin. Self-Assembly of Mesoscopic Metal-Polymer Amphiphiles. *Science*, 303(5656):348–351, 2004.

[29] M Poty, G Lumay, and N Vandewalle. Customizing mesoscale self-assembly with three-dimensional printing. *New Journal of Physics*, 16(2):023013, feb 2014.

[30] Ned Bowden, Insung S. Choi, Bartosz A. Grzybowski, and George M. Whitesides. Mesoscale self-assembly of hexagonal plates using lateral capillary forces: Synthesis using the 'capillary bond'. *Journal of the American Chemical Society*, 121(23):5373–5391, 1999.

[31] Bartosz A Grzybowski, Howard A Stone, and George M Whitesides. Dynamic self-assembly of magnetized, millimetre-sized objects rotating at a liquid–air interface. *Nature*, 405(6790):1033–1036, 2000.

[32] Nicolas Vandewalle, Martin Poty, Nathan Vanesse, Jérémie Caprasse, Thomas Defize, and Christine Jérôme. Switchable self-assembled capillary structures. *Soft Matter*, 16(45):10320–10325, 2020.

[33] Kazuo Hosokawa, Isao Shimoyama, and Hirofumi Miura. Two-dimensional micro-self-assembly using the surface tension of water. *Sensors and Actuators A: Physical*, 57(2):117–125, 1996. Ninth International Workshop on Micro Electro Mechanical System.

[34] D.Y.C Chan, J.D Henry, and L.R White. The interaction of colloidal particles collected at fluid interfaces. *Journal of Colloid and Interface Science*, 79(2):410–418, 1981.

[35] L. Botto, E. P. Lewandowski, Cavallaro, and K. J. Stebe. Capillary interactions between anisotropic particles. *Soft Matter*, 8:9957–9971, 2012.

[36] S. Ni, J. Leemann, H. Wolf, and L. Isa. Insights into mechanisms of capillary assembly. *Faraday Discussions*, 181:225–242, 2015.

[37] J. Liu and S. Li. Capillarity-driven migration of small objects: A critical review. *European Physical Journal E*, 42:1, 2019.

[38] I. B. Liu, N. Sharifi-Mood, and K. J. Stebe. Curvature-driven assembly in soft matter. *Philosophical Transactions of the Royal Society of London A*, 374:20150133, 2015.

[39] M. Poty and N. Vandewalle. Equilibrium distances for the capillary interaction between floating objects. *Soft Matter*, 17:6718–6727, 2021.

[40] Charlotte Py, Paul Reverdy, Lionel Doppler, José Bico, Benoît Roman, and Charles N. Baroud. Capillary origami: Spontaneous wrapping of a droplet with an elastic sheet. *Phys. Rev. Lett.*, 98:156103, Apr 2007.

[41] NR Geraldi, F Fouzia Ouali, RH Morris, Glen McHale, and MI Newton. Capillary origami and superhydrophobic membrane surfaces. *Applied Physics Letters*, 102(21):214104, 2013.

[42] A. Legrain, T. G. Janson, J. W. Berenschot, L. Abelmann, and N. R. Tas. Controllable elastocapillary folding of three-dimensional micro-objects by through-wafer filling. *Journal of Applied Physics*, 115(21):214905, 2014.

[43] S. J. P. Callens, N. Tümer, and A. A. Zadpoor. Hyperbolic origami-inspired folding of triply periodic minimal surface structures. *Applied Materials Today*, 15:453–461, 2019.

[44] M. Boncheva, S. A. Andreev, L. Mahadevan, A. Winkleman, D. R. Reichman, M. G. Prentiss, S. Whitesides, and G. M. Whitesides. Magnetic self assembly of 3d surfaces from planar sheets. *Proceedings of the National Academy of Sciences of the United States of America*, 102, 2005.

[45] Charles Vernon Boys et al. *Soap-bubbles, and the forces which mould them*. Cornell University Library, 1890.

[46] Richard Courant. Soap film experiments with minimal surfaces. *The American Mathematical Monthly*, 47(3):167–174, 1940.

[47] C Gaulon, C Derec, T Combriat, Philippe Marmottant, and F Elias. Sound and vision: visualization of music with a soap film. *European Journal of Physics*, 38(4):045804, 2017.

[48] P. Vorobieff, M. Rivera, and R. E. Ecke. Soap film flows: Statistics of two-dimensional turbulence. *Physics of Fluids*, 11(8):2167–2177, 1999.

[49] J. M. Chomaz and B. Cathalau. Soap films as two-dimensional classical fluids. *Phys. Rev. A*, 41:2243–2245, Feb 1990.

[50] Isaac Newton. *Opticks, or, a treatise of the reflections, refractions, inflections & colours of light*. Prabhat Prakashan, 1730.

[51] Lorasne Champougny, Jonas Miguet, Robin Henaff, Frederic Restagno, Franasois Boulogne, and Emmanuelle Rio. Influence of evaporation on soap film rupture. *Langmuir*, 34(10):3221–3227, 2018.

[52] Steffen Berg, Eric A. Adelizzi, and Sandra M. Troian. Experimental study of entrainment and drainage flows in microscale soap films. *Langmuir*, 21(9):3867–3876, 2005.

[53] Winnie R McEntee and Karol J Mysels. Bursting of soap films. an experimental study. *The Journal of Physical Chemistry*, 73(9):3018–3028, 1969.

[54] Nicholas D Brubaker. Shapes of large, static soap bubbles. *Proceedings of the Royal Society A*, 477(2246):20200851, 2021.

[55] Pauline Petit, Jacopo Seiwert, Isabelle Cantat, and A-L Biance. On the generation of a foam film during a topological rearrangement. *Journal of Fluid Mechanics*, 763:286–301, 2015.

[56] Dominique Langevin. Aqueous foams and foam films stabilized by surfactants. gravity-free studies. *Comptes Rendus Macanique*, 345(1):47–55, 2017. Basic and applied researches in microgravity a tribute to Bernard Zappolias contribution.

[57] Laurie Saulnier, Lorene Champougny, Gael Bastien, Frederic Restagno, Dominique Langevin, and Emmanuelle Rio. A study of generation and rupture of soap films. *Soft Matter*, 10:2899–2906, 2014.

[58] Ioan Tudur Davies and Christophe Raufaste. Effect of gravity on the orientation and detachment of cubic particles adsorbed at soap film or liquid interfaces. *Soft Matter*, 2021.

[59] C.-H. Chen, A. Perera, P. Jackson, B. Hallmark, and J.F. Davidson. The distortion of a horizontal soap film due to the impact of a falling sphere. *Chemical Engineering Science*, 206:305–314, 2019.

[60] SJ Cox and IT Davies. Bubble entrainment by a sphere falling through a horizontal soap foam. *EPL (Europhysics Letters)*, 130(1):14002, 2020.

[61] Ioan Tudur Davies. Simulating the interaction between a descending super-quadric solid object and a soap film. *Proceedings of the Royal Society A: Mathematical, Physical and Engineering Sciences*, 2018.

[62] S. Mollaei, M. Nasiri, N. Soltanmohammadi, R. Shirsavar, A. Ramos, and A. Amjadi. Soap-film flow induced by electric fields in asymmetric frames. *Phys. Rev. E*, 97:043110, Apr 2018.

[63] Oriane Bonhomme, Olivier Liot, Anne-Laure Biance, and Lydéric Bocquet. Soft nanofluidic transport in a soap film. *Phys. Rev. Lett.*, 110:054502, Feb 2013.

[64] Derek E Moulton and John A Pelesko. Theory and experiment for soap-film bridge in an electric field. *Journal of colloid and interface science*, 322(1):252–262, 2008.

[65] Mars M. Alimov, Alexander V. Bazilevsky, and Konstantin G. Kornev. Minimal surfaces on mirror-symmetric frames: a fluid dynamics analogy. *Journal of Fluid Mechanics*, 897:A36, 2020.

[66] Leonhard Euler. *Methodus inveniendi lineas curvas maximi minimive proprietate gaudentes*. apud Marcum-Michaelem Bousquet, 1744.

[67] V. A. Frolov and V. A. Lizunov. A. *Ya. Dunina-Barkovskaya, A.V. Samsonov & J. Zimmerberg. Shape bistability of a membrane neck: A toggle switch to control vesicle content release*, 100:9220–9224, 2003.

[68] M. Chabanon and P. Rangamani. Gaussian curvature directs the distribution of spontaneous curvature on bilayer membrane necks. *Soft Matter*, 14:2281–2294, 2018.

[69] Mars M. Alimov, Alexander V. Bazilevsky, and Konstantin G. Kornev. Soap film on two noncircular frames. *Physics of Fluids*, 33(5):052104, 2021.

[70] Nathaniel D. Robinson and Paul H. Steen. Observations of singularity formation during the capillary collapse and bubble pinch-off of a soap film bridge. *Journal of Colloid and Interface Science*, 241(2):448–458, 2001.

[71] Raymond E. Goldstein, Adriana I. Pesci, Christophe Raufaste, and James D. Shemilt. Geometry of catenoidal soap film collapse induced by boundary deformation. *Phys. Rev. E*, 104:035105, Sep 2021.

[72] Raymond E. Goldstein, H. Keith Moffatt, Adriana I. Pesci, and Renzo L. Ricca. Soap-film möbius strip changes topology with a twist singularity. *Proceedings of the National Academy of Sciences*, 107(51):21979–21984, 2010.

[73] H. K. Moffatt, Raymond E. Goldstein, and Adriana I. Pesci. Soap-film dynamics and topological transitions under continuous deformation. *Phys. Rev. Fluids*, 1:060503, Oct 2016.

[74] S. Hutzler, M. Saadatfar, A. van der Net, D. Weaire, and S.J. Cox. The dynamics of a topological change in a system of soap films. *Colloids and Surfaces A: Physicochemical and Engineering Aspects*, 323(1):123–131, 2008. Bubble and Drop Interfaces.

[75] Joseph Antoine Ferdinand Plateau. *Statique expérimentale et théorique des liquides soumis aux seules forces moléculaires*, volume 2. Gauthier-Villars, 1873.

[76] Jesse Douglas. Solution of the problem of plateau. *Transactions of the American Mathematical Society*, 33(1):263–321, 1931.

[77] Kenneth A Brakke. The surface evolver. *Experimental mathematics*, 1(2):141–165, 1992.

[78] Joseph-Louis Lagrange. *Essai d'une nouvelle methode pour determiner les maxima et les minima des formules integrals indefinies*. Miscellanea Taurinensia 2, 1762.

[79] Louis Salkin, Alexandre Schmit, Pascal Panizza, and Laurent Courbin. Influence of boundary conditions on the existence and stability of minimal surfaces of revolution made of soap films. *American Journal of Physics*, 82(9):839–847, 2014.

[80] C. W. B. Goldschmidt. *Determinatio superficiei minimae rotatione curvae data duo puncta jungentis circa datum axem ortae.* Dieterichianis, Gottingae, 1831.

[81] Steven A Cryer and Paul H Steen. Collapse of the soap-film bridge: quasistatic description. *Journal of colloid and interface science*, 154(1):276–288, 1992.

[82] Aisa Biria and Eliot Fried. Theoretical and experimental study of the stability of a soap film spanning a flexible loop. *International Journal of Engineering Science*, 94:86–102, 2015.

[83] Raymond E. Goldstein, Herbert E. Huppert, H. Keith Moffatt, and Adriana I. Pesci. Instability of a gravity current within a soap film. *Journal of Fluid Mechanics*, 753:R1, 2014.

[84] M. Winkler, G. Kofod, R. Krastev, S. Stöckle, and M. Abel. Exponentially fast thinning of nanoscale films by turbulent mixing. *Phys. Rev. Lett.*, 110:094501, Feb 2013.

[85] Vadim A Frolov, Vladimir A Lizunov, Antonina Ya Dunina-Barkovskaya, Andrey V Samsonov, and Joshua Zimmerberg. Shape bistability of a membrane neck: a toggle switch to control vesicle content release. *Proceedings of the National Academy of Sciences*, 100(15):8698–8703, 2003.

[86] Y.J. Chen and P. H. Steen. Dynamics of inviscid capillary breakup: collapse and pinchoff of a film bridge. *Journal of Fluid Mechanics*, 341, 1997.

[87] Soumya Jana and Sayan Kar. Perturbative stability of catenoidal soap films. *The European Physical Journal Plus*, 128(9):1–12, 2013.

Appendix A

Supplementary calculations

A.1 Gravitational Effects

Consider a soap film supported by a circular loop of radius R_o with orientation perpendicular to the direction of gravitational acceleration.

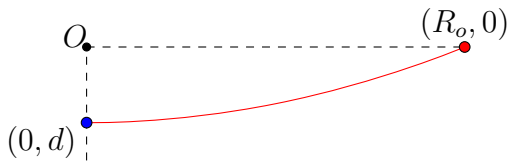


Figure A.1: Schematic of a potential equilibrium configuration of a soap film deflection under the effect of its own mass ($r = 0$ is the axis of rotation). The soap-film membrane is shown in red, with a Dirichlet condition at $(R_o, 0)$ and a Neumann condition at $(0, d)$ for a deflection of magnitude d

The shape of the soap film in Figure A.1 can be represented as $z(r)$ such that $z(R_o) = 0$ and $z'(0) = 0$ are relevant boundary conditions. The total energy of the system can be written as a sum of the surface energy of the soap film and its corresponding gravitational potential energy, as follows

$$\bar{\mathcal{E}}(z) = \int_0^{R_o} 2\pi r \left(2\sigma + \rho\tau g z\right) \sqrt{1 + (z'(r))^2}\, dr, \tag{A.1.1}$$

where σ is the surface tension of the soap film, ρ is the density(assumed to be constant), τ is the thickness (also assumed to be constant), and g is the gravitational acceleration. As (A.1.1) has fixed endpoints and depends on r, $z(r)$, and $z'(r)$ the Euler–Lagrange

Equation corresponding the the functional $\bar{\mathcal{E}}(r, z, z')$ can be directly computed as

$$0 = \frac{\partial \bar{\mathcal{E}}}{\partial z} - \frac{\mathrm{d}}{\mathrm{d}r}\left(\frac{\partial \bar{\mathcal{E}}}{\partial z'}\right), \tag{A.1.2}$$

$$= 2\pi r \rho\tau g\sqrt{1+(z')^2} - \frac{\mathrm{d}}{\mathrm{d}r}\left[\frac{2\pi r(2\sigma+\rho\tau g z)z'}{\sqrt{1+(z')^2}}\right], \tag{A.1.3}$$

$$= (r - z'(z+\frac{2\sigma}{\rho\tau g}))((z')^2+1) - rz''(z+\frac{2\sigma}{\rho\tau g}). \tag{A.1.4}$$

Non-dimensionalizing (A.1.4) by $r^* = \frac{r}{R_o}$, $\bar{z} = \frac{z}{R_o}$ and setting $B_g = \frac{2\sigma}{\rho\tau g R_o}$ yields

$$\begin{cases} \bar{z}'' = \left(1+(\bar{z}')^2\right)\left(\dfrac{1}{\bar{z}+B_g} - \dfrac{\bar{z}'}{r^*}\right), & \text{(A.1.5)} \\ z(1) = 0, & \text{(A.1.6)} \\ z'(0) = 0. & \text{(A.1.7)} \end{cases}$$

Solving this system numerically for $B_g \in [20, 2000]$ and evaluating $z(0)$, a plot of the maximal deflection (d) of a soap film deformation under the effect of its mass is seen in Figure A.2. The physical parameters $\sigma = 0.024\mathrm{N/m}$, $\rho = 1100\mathrm{kg/m^3}$, $g = 9.81\mathrm{m/s^2}$, $R_o = 5cm$, and τ ranging from 50 to 5000nm correspond to B_g ranging from 17.8 to 1779. As B_g resembles the recripocal of a standard Bond number, as B_g approaches infinity the Bond number of the system approaches zero.

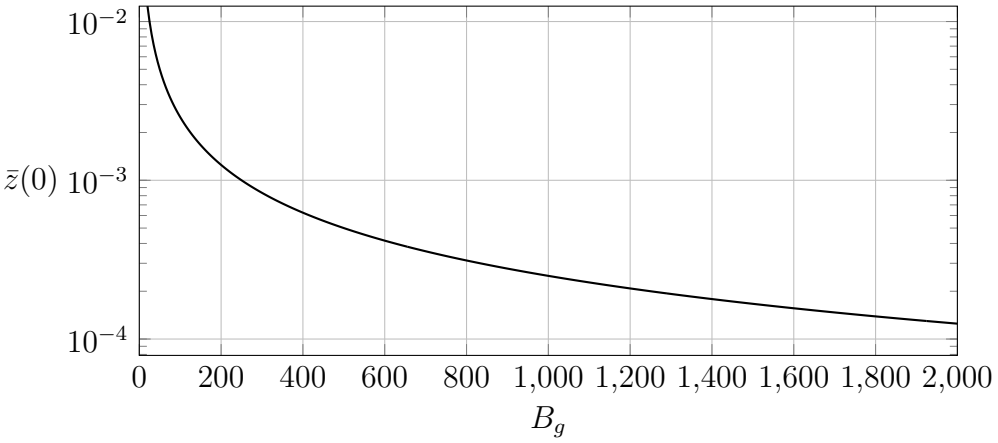


Figure A.2: The curve seen shows the total dimensionless deflection $d = \bar{z}(0) = z(0)/R_o$ (in log scale) of a soap film oriented as shown in (A.1). The dimensionless parameter $B_g = 2\sigma/\rho\tau g R_o$ can be charecterized as the inverse of the Bond number of the system. Note that for large values of R_o the assumption that the density is constant no longer holds. As the soap film grows in size and the deflection increases a fluid flow is induced, resulting in greater τ and ρ near $r = 0$.

A.2 Catenary solution of the axisymmetric minimal surface equation

From (2.2.14) the axisymmetric minimal surface equation is reproduced as follows

$$0 = \sqrt{1+(r')^2} - \frac{d}{dz}\left(\frac{rr'}{\sqrt{1+(r')^2}}\right) \tag{A.2.1}$$

Evaluating the derivative and rearranging the terms:

$$0 = \sqrt{1+(r')^2} - \frac{(r')^4 + (r')^2 + rr''}{(1+(r')^2)^{3/2}} \tag{A.2.2}$$

$$= (1+(r')^2)^2 - (r')^4 - (r')^2 - rr'' \tag{A.2.3}$$

$$= 1 + (r')^2 - rr'' \tag{A.2.4}$$

Note that (A.2.4) is the axisymmetric minimal surface equation presented in Section 2.1. Letting $u = r' = \mathrm{d}r/\mathrm{d}z$ we can simplify (A.2.4) to a first order differential equation.

$$ru\frac{\mathrm{d}u}{\mathrm{d}r} - u^2 - 1 = 0 \tag{A.2.5}$$

$$r\frac{\mathrm{d}u}{\mathrm{d}r} = \frac{1+u^2}{u} \tag{A.2.6}$$

By separation of variables, we can now integrate, yielding:

$$\ln(r) = \frac{\ln(1+u^2)}{2} + C_1 \tag{A.2.7}$$

$$C_1 r^2 = 1 + u^2 \tag{A.2.8}$$

$$u^2 = C_1 r^2 - 1 \tag{A.2.9}$$

$$u = \sqrt{C_1 r^2 - 1} \tag{A.2.10}$$

(A.2.10) is a first-order ordinary differential equation in terms of r and a constant of integration C_1. This allows for another integration and a solution written in terms of the constants of integration C_1 and C_2

$$\frac{\mathrm{d}r}{\mathrm{d}z} = \sqrt{C_1 r^2 - 1} \tag{A.2.11}$$

$$r(z) = \frac{\cosh(\sqrt{C_1}(z+C_2))}{\sqrt{C_1}} \tag{A.2.12}$$

By evaluating (A.2.12) at two points a system of 2 equations and two unknowns (C_1 and C_2) can be found. But while it is possible to isolate for C_2, an expression for C_1 cannot be written in closed form. As such consider (A.2.11) evaluated at (r_1, z_1), and (A.2.12) evaluated at (r_2, z_2). This allows for both C_1 and C_2 to be written in closed

form in terms of the endpoints and $r'(z_1)$

$$C_1 = \frac{1 + r'(z_1)^2}{r_1^2} \tag{A.2.13}$$

$$C_2 = \frac{\cosh^{-1}(r_2\sqrt{C_1})}{\sqrt{C_1}} - z_2 \tag{A.2.14}$$

(A.2.12) can thus be written as

$$r(z) = \frac{r_1}{\sqrt{1 + r'(z_1)^2}} \cosh\left(\frac{z\sqrt{1 + r'(z_1)^2}}{r_1} + \cosh^{-1}\left(\frac{r_2\sqrt{1 + r'(z_1)^2}}{r_1}\right) - z_2\frac{\sqrt{1 + r'(z_1)^2}}{r_1}\right) \tag{A.2.15}$$

Non-Dimensionalizing the system by setting $\bar{r} = r/r_2$, $\bar{z} = z/r_2$, $r^* = r_1/r_2$, $z^* = z_2/r_2$, and $R' = \sqrt{1 + r'(z_1)^2}$

$$\bar{r} = \frac{r^*}{R'} \cosh\left(\frac{(\bar{z} - z^*)R'}{r^*} + \cosh^{-1}\left(\frac{R'}{r^*}\right)\right) \tag{A.2.16}$$

(A.2.16) can be rearranged such that $\bar{z}$ is a function of $\bar{r}$ as follows

$$\bar{z} = \frac{r*}{R'}\left[\cosh^{-1}\left(\frac{\bar{r}R'}{r^*}\right) - \cosh^{-1}\left(\frac{R'}{r^*}\right)\right] + z^* \tag{A.2.17}$$

A.3 Force balance formulation of gravity-mediated assemblies

In the same geometry as seen in Figure 2.6 note that the total force acting on the suspended ring of radius R_i is concentrated on the edge. Due to the symmetry of the system, the force balance perpendicular to the direction of gravity is directly satisfied. In the direction of gravitational acceleration, a balance between the force due to the surface tension of the soap film and the force due to gravity must be satisfied. As such, at the point (R_i, h), the following holds

$$0 = F_g + F_\sigma \tag{A.3.1}$$
$$= mg + (2\pi R_i)(2\sigma\cos(\phi)) \tag{A.3.2}$$

where ϕ is the angle between the soap film and the direction of gravitational acceleration at the point (R_i, h). Notice that $\frac{\mathrm{d}r}{\mathrm{d}z}|_{z=h} = \tan(\phi)$, namely the slope of the soap film at (R_i, h) or $r'(h)$ can be written in terms of ϕ

$$\left.\frac{\mathrm{d}r}{\mathrm{d}z}\right|_{z=h} = r'(h) = \tan(\phi) = \tan\left(\cos^{-1}\left(\frac{-mg}{4\pi\sigma R_i}\right)\right) \tag{A.3.3}$$

Knowing that a soap film spanning two concentric rings separated by some distance h can be represented by a catenary, the following system determines the shape of the soap film

$$\begin{cases} r(z) = \dfrac{\cosh(\sqrt{C_1}(z + C_2))}{\sqrt{C_1}} & \text{(A.3.4)} \\ C_1 = \dfrac{(r'(h))^2 + 1}{R_i^2} & \text{(A.3.5)} \\ C_2 = \dfrac{\cosh(R_o\sqrt{C_1})}{\sqrt{C_1}} & \text{(A.3.6)} \end{cases}$$

Using (A.3.3), the constant of integration C_1 and C_2 can be expressed as follows

$$\begin{cases} C_1 = \left(\dfrac{4\pi\sigma}{mg}\right)^2 & \text{(A.3.7)} \\ C_2 = \dfrac{mg}{4\pi\sigma}\cosh\left(\dfrac{4\pi\sigma R_o}{mg}\right) & \text{(A.3.8)} \end{cases}$$

Evaluating (A.3.4) at the point (R_i, h) and isolating for h the same expression as shown in (2.2.25) is recovered. This is obvious as the constants of integration are identical to those recovered in Chapter 2.

Appendix B

Open prismatic structures

This appendix is provided as a library of images. While a multitude of experiments concerning the displacement-driven assembly of prismatic structures was conducted, experimental trials used as data points or referenced throughout the thesis are found in Figure B.1. The bases are all regular polygons with a side length of 2 cm. For each distinct base, two different rectangular tiles are presented with heights of 2 cm and 2.5 cm. The experiments corresponding to tiles of height 2 cm show detached assemblies in column 4 while the other prismatic height depicts the instant prior to pinch-off in the fourth column. The average mass of the square tiles is 0.0577 g while the rectangular tiles of height 2.5 cm have an average mass of 0.0636 g.

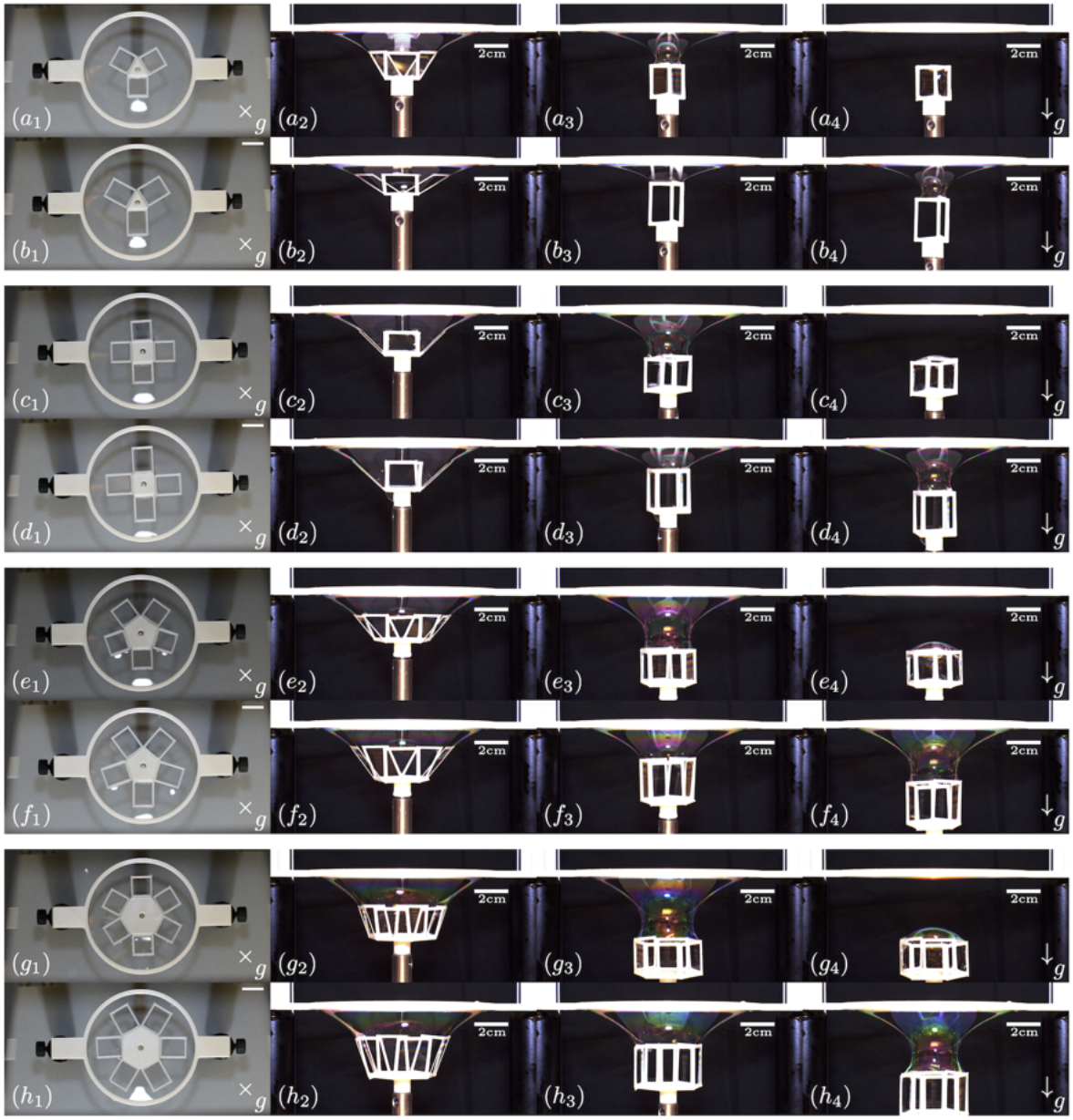


Figure B.1: Self-assembly of prismatic structures with bases of 20 mm side width, the rectangular faces are of 20 and 25 mm height. Column (a_1)-(h_1) is a top view of the initial arrangements of the components prior to the initiation of the base displacement. From column 2 to 3 the lower bounding curve of the soap film exhibits a qualitative change as the components snap together the boundary is planar, matching the shape of the base.

Appendix C

Pyramidal structures

Similar to the appendix regarding prismatic structures this appendix functions as a library of images showing all relevant experimental trials. Each of the following figures is labeled according to the shape of the base. All bases are regular polygons with side lengths of 2 cm. The triangular tiles making up the faces of the pyramidal structures are all iscolescs and separated into four kinds. All triangles have one edge of length 2 cm and the other two edges have lengths as follows: 2 cm, 2.2 cm, 2.4 cm, and 2.6 cm. Correspondingly, the average masses of these types of triangular tiles are: 0.0391 g, 0.0402 g, 0.0469 g, and 0.048 g respectively.

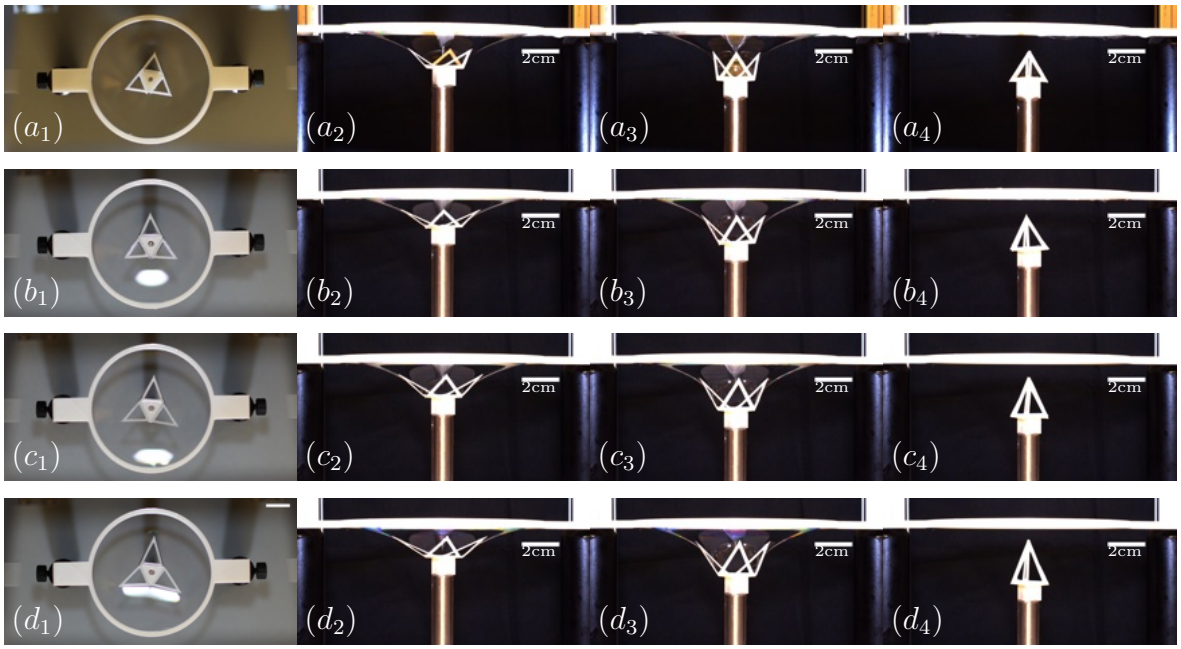


Figure C.1: Displacement-driven triangular pyramidal structures.

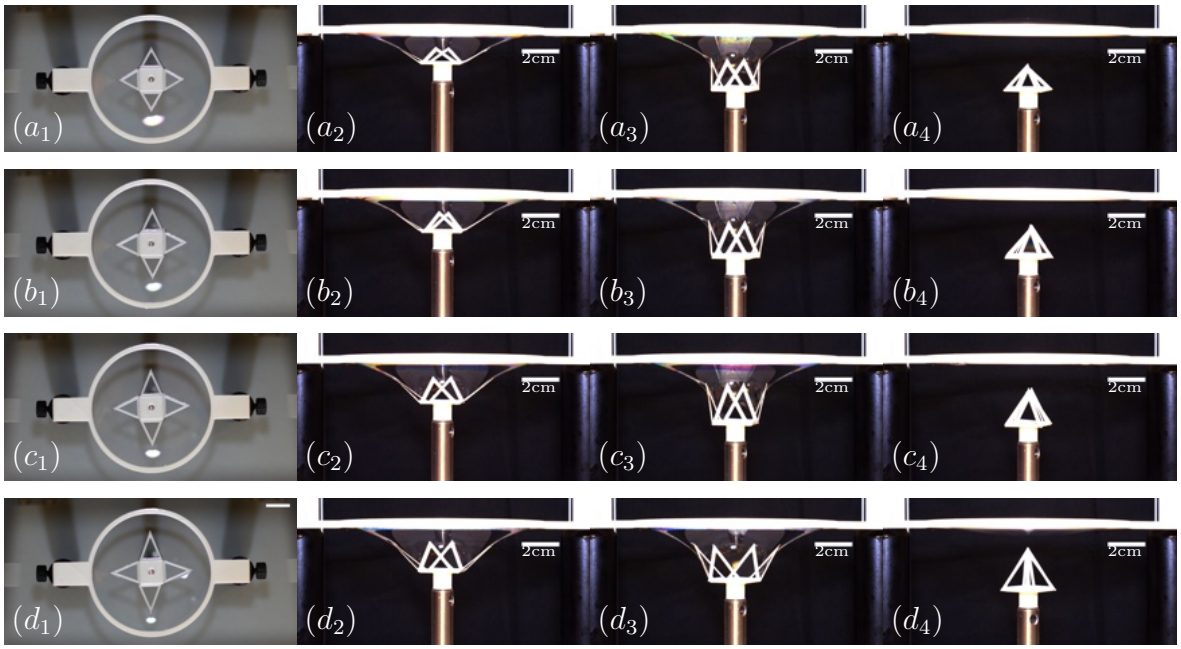


Figure C.2: Displacement-driven square pyramidal structures.

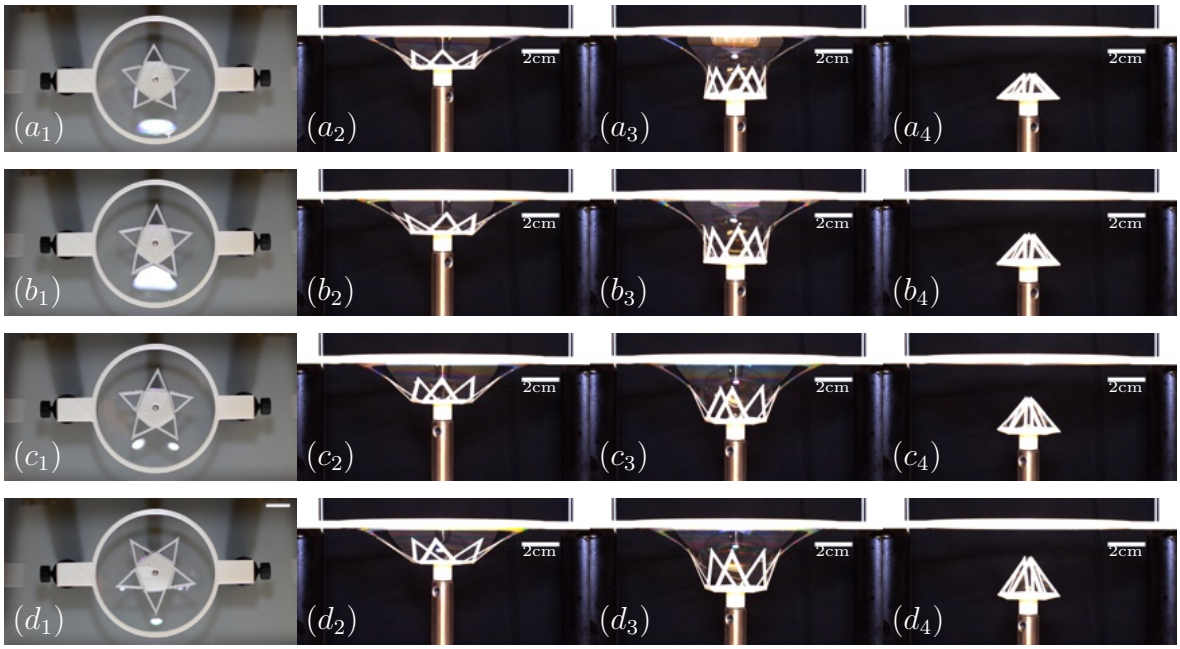


Figure C.3: Displacement-driven pentagonal pyramidal structures.

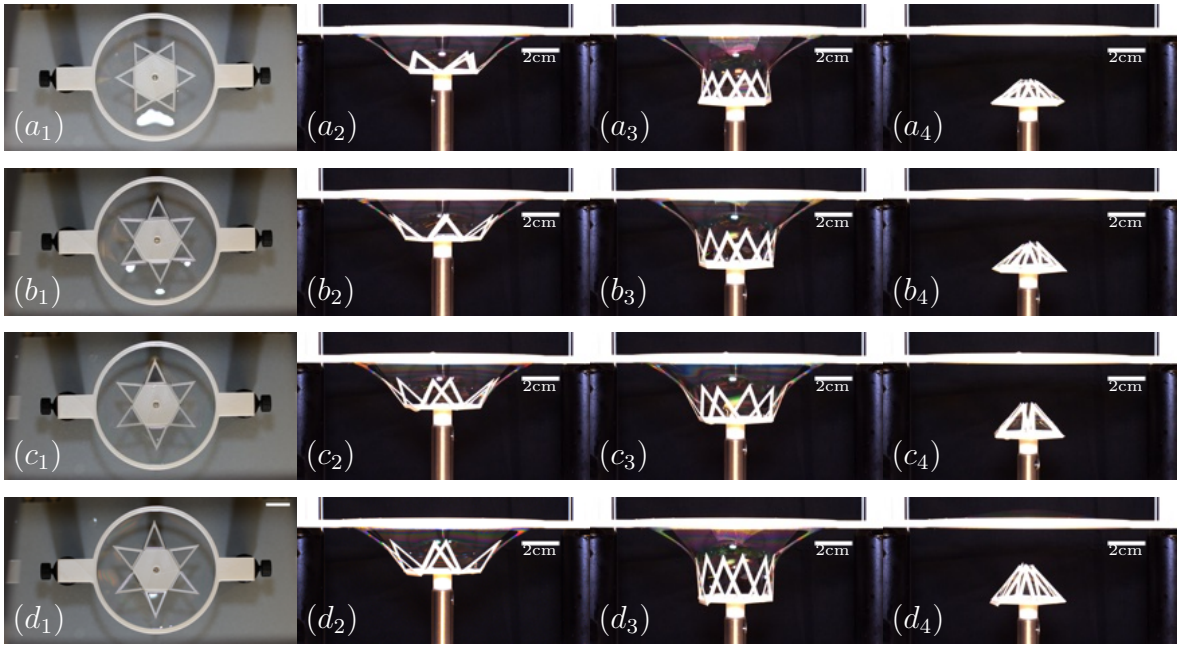


Figure C.4: Displacement-driven hexagonal pyramidal structures.